RAJKUMAR SAVAI

ESTABLISHMENT OF MOUSE LUNG TUMOR MODELS AND DEVELOPMENT OF NEW THERAPEUTIC APPROACHES

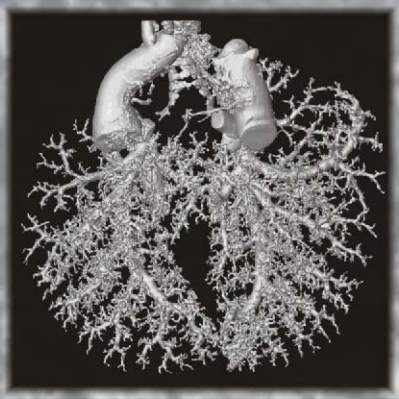

INAUGURALDISSERTATION
zur Erlangung des Grades eines
Doktors der Humanbiologie
des Fachbereichs Medizin der
Justus-Liebig-Universität Gießen

édition scientifique
VVB LAUFERSWEILER VERLAG

Das Werk ist in allen seinen Teilen urheberrechtlich geschützt.

Jede Verwertung ist ohne schriftliche Zustimmung des Autors oder des Verlages unzulässig. Das gilt insbesondere für Vervielfältigungen, Übersetzungen, Mikroverfilmungen und die Einspeicherung in und Verarbeitung durch elektronische Systeme.

1. Auflage 2006

All rights reserved. No part of this publication may be reproduced, stored in a retrieval system, or transmitted, in any form or by any means, electronic, mechanical, photocopying, recording, or otherwise, without the prior written permission of the Author or the Publishers.

1st Edition 2006

© 2006 by VVB LAUFERSWEILER VERLAG, Giessen
Printed in Germany

VVB LAUFERSWEILER VERLAG
édition scientifique

STAUFENBERGRING 15, D-35396 GIESSEN
Tel: 0641-5599888 Fax: 0641-5599890
email: redaktion@doktorverlag.de

www.doktorverlag.de

ESTABLISHMENT OF MOUSE LUNG TUMOR MODELS AND DEVELOPMENT OF NEW THERAPEUTIC APPROACHES

INAUGURALDISSERTATION
zur Erlangung des Grades eines
Doktors der Humanbiologie
des Fachbereichs Medizin der
Justus-Liebig-Universität Giessen

vorgelegt von

RAJKUMAR SAVAI
(M.Sc in Biochemistry)

aus Warangal, Indien

Giessen 2005

Aus der Medizinischen Klinik II
Direktor: Prof. Dr. med. Werner Seeger
des Universitätsklinikums Gießen und Marburg
Standort Gießen

Gutachter: Priv.-Doz. Dr. rer. nat. Jörg Hänze

Gutachter: Prof. Dr. med. Rainer M. Bohle

Tag der Disputation: 12-05-2006

My Parents

Komuramma, Ilaiah

My brothers

Late Sambaiah

Ravi, Srinivas

&

Shobha, Rama, Soni, Divya,
Deepak, Vamshi, Varun.

Table of Contents

Chapter	Description	Page(s)
1.	**Introduction**	**1-12**
1.1	**Lung cancer pathology**	**1**
1.1.1	Risk factors	1
1.1.2	Pathological processes	2
1.2	**Classification**	**3**
1.3	**Treatment and prognosis**	**4**
1.3.1	Staging	4
1.3.2	Management	6
1.3.2.1	Surgery	6
1.3.2.2	Chemotherapy	6
1.3.2.3	Radiation therapy	6
1.3.2.4	Combined modality therapy	7
1.3.2.5	Targeted therapy	7
1.3.2.6	Immunotherapy	8
1.4	**Animal models of lung cancer**	**9**
1.4.1	Spontaneous tumor models	9
1.4.2	Transplantable animal tumor models	10
1.4.2.1	Xenograft model	10
1.4.2.2	Orthotopic xenograft model	10
1.4.3	Genetically engineered animals	10
1.5	**Imaging techniques**	**11**
2	**Aims**	**13**

Chapter	Description	Page(s)
3	**Materials and Methods**	**14-28**
3.1	**Cell biological methods**	**14**
3.1.1	Culture of human A549, mouse LLC1 and mouse B16/F10 cells	14
3.1.2	Cell culture and generation of HIF-1α overexpressing cells	14
3.1.3	Hypoxia treatment	15
3.1.4	Immunocytochemistry of HIF-1α	15
3.1.5	Hypoxia-responsive element reporter gene assay	15
3.1.6	Determination of vascular endothelial growth factor (VEGF) concentration	16
3.1.7	MTT assay	16
3.1.8	Thymidine incorporation	16
3.1.9	Soft- agar colony-formation assay	17
3.1.10	Generation of bone marrow derived dendritic cells	17
3.1.11	DC/ Tumor fusion cell preparation	17
3.1.12	Fusion efficiency and fluorescence-activated cell sorting	18
3.1.13	Proliferation assay for spleen and lymph node cells	18
3.1.14	Cytotoxic assays for spleen and lymph node cells	19
3.2	**Animal studies**	**20**
3.2.1	Animals	20
3.2.2	Tumorigenicity in nude mice	20
3.2.3	Immunization	20
3.2.4	Pre tumor challenge	21
3.2.5	Vaccine therapy	21
3.2.6	Adoptive immunotherapy	21
3.2.7	Intratracheal instillation	22

Chapter	Description	Page(s)
3.2.8	Infusion of fluorescent microspheres	22
3.2.9	Tumor and lung tissue digestion and processing	23
3.3	**Imaging techniques**	**23**
3.3.1	Flat-panel volumetric computed tomography	23
3.3.2	Multislice computed tomography	24
3.3.3	Micro computed tomography	24
3.4	**Histological methods**	**25**
3.4.1	Hematoxylin and Eosin (H&E) staining	25
3.4.2	Assessment of microvessel density	25
3.4.3	Apoptosis by cyto- and histochemistry	25
3.4.4	Histology of fluorescent microsphere-infused lungs	26
3.5	**Molecular biological methods**	**26**
3.5.1	Construction of expression plasmid for HIF-1α	26
3.5.2	Real-time reverse transcription-polymerase chain reaction (RT-PCR)	27
3.5.3	Gene expression array analysis	27
3.5.4	Semiquantitative RT-PCR	28
3.6	**Data analysis**	**28**
4	**Results**	**29-59**
4.1	**Mouse models of lung cancer**	**29**

Chapter	Description	Page(s)
4.2	**Role of HIF-1α on tumor growth of lung adenocarcinomas**	**30**
4.2.1	Characterization of cells transfected by HIF-1α	30
4.2.2	Effect of HIF-1α on proliferation and apoptosis in cultured cells	32
4.2.3	Effect of HIF-1α on tumor growth in vivo	34
4.2.4	Effect of HIF-1α on tumor vascularity and apoptosis	35
4.3	**Anti-tumor effects of LLC1/DC fusion hybrids**	**36**
4.3.1	Characterization of LLC1/DC cell hybrids	36
4.3.2	Proliferation and cytotoxic response of hybrid immunized mice T-lymphocytes	38
4.3.3	Cytokine profile of hybrid immunized mice	39
4.3.4	Immunization with hybrids induce growth retardation of LLC1 tumor challenge	41
4.3.5	Anti-tumor effect of hybrid vaccination	42
4.3.6	Adoptive therapy of established syngeneic tumors with hybrids primed T-cells	44
4.4	**Detection of pulmonary nodules in a lewis lung carcinoma model by fpvCT and MSCT**	**46**
4.5	**Quantitative analysis of lung tumor vessel content by micro computed tomography**	**50**
4.6	**Distribution of pulmonary and bronchial blood supply to lewis lung carcinomas**	**52**
4.6.1	Tumor model	52
4.6.2	Fluorescent microspheres in LLC1 tumor lungs	53
4.6.3	Analysis of micro computed tomography images	55

Chapter	Description	Page(s)
4.6.4	Repetitive analysis of fpvCT images in living mice	58
5.	**Discussion**	**60-68**
5.1	**Therapeutic strategies**	**60**
5.1.1	HIF-1α overexpression in lung adenocarcinoma mouse model	60
5.1.2	Therapy with hybrid primed lymphocytes and hybrid vaccination	61
5.2	**Tumor imaging modalities**	**63**
5.2.1	Micro computed tomography (μCT)	63
5.2.2	Flat panel volumetric computed tomography (fpvCT)	65
5.3	**Applications**	**66**
5.3.1	Delineation of vascular supply of lung tumors	66
6	**Summary**	**69**
7	**Zusammenfassung**	**71**
8	**References**	**73**
9	**Abbreviations**	**87**
10	**Erklärung**	**89**
10	**Acknowledgements**	**90**
11	**Curriculum vitae**	**91**
12	**Publications**	**93**

List of Figures

Figures	Description	Page(s)
1	Sequential pathogenic changes involved in lung cancer	3
2	Cell morphology and mouse strains	29
3	Subcutaneous tumor, lung tumor detection and measurement	30
4	Characterization of HIF-1α expression in stable transfected A549 cells	31
5	Analysis of cell proliferation in stable-transfected A549 cells	32
6	Soft agar cloning of stable-transfected A549 cells	33
7	Measurement of apoptosis in vitro	33
8	Tumor growth from cells stable-transfected with empty plasmid or plasmid carrying HIF-1α	34
9	Quantification of vascular density and apoptosis	35
10	Fusion rate	36
11	Fluorescence micrographs of LLC1, dendritic cells, and fusion hybrids	37
12	Proliferative activity and cytotoxicity of T lymphocytes from immunized mice	39
13	Representation of mouse common cytokine gene arrays from immunized mouse blood	40
14	Anti-tumor effects of hybrid immunization	42
15	Lower tumor development by hybrid vaccination	43
16	Suppression of LLC1 tumor growth in mice given adoptive immunotherapy	45
17	3D segmentation of the lung	46
18	Display of coronal and axial reformatted images of datasets acquired with fpvCT and MSCT	47

Figures	Description	Page(s)
19	Comparison between fpvCT image and histology is displayed	50
20	Comparison of μCT and microscopic images	51
21	Quantitative volumetric measurements of extracted tumors and vascular fractions	51
22	Analysis of lung tumor growth by histology and fpvCT	52
23	Blood vessel supply of healthy and tumor-bearing lung tissue analyzed by fluorescent microspheres	54
24	Volume rendering technique (VRT) images of the μCT	56
25	Maximum intensity projection (MIP) and multiplanar reconstructions (MPR) images of the μCT	57
26	In vivo volumetric computed tomography (fpvCT) scanning of LLC1 lung tumors	58

List of Tables

Tables	Description	Page(s)
1	International staging system for lung cancer	5
2	Lung tumor analysis	49
3	Measurement of tumor growth by histology and fpvCT	53
4	Analysis of pulmonary and systemic blood flow markers	55

1 Introduction

Lung cancer, a disease characterized by uncontrolled cell growth in the lungs, is the leading cause of cancer deaths for both men and women. Lung cancer was first diagnosed in the mid-nineteenth century, when it was considered a relatively rare occurrence. By the turn of the century, it was considered the most common malignancy and the leading cause of cancer-related death in more than 25 developed countries. Lung cancer accounts for almost 28% of all cancer deaths worldwide, with a global incidence of this disease rising at approximately 0.5% per year. Lung cancer is often fatal, with a 5 year survival rate of ~14%, primarily due to inability to detect the disease early. In the European Union, lung cancer accounts for 20% of all cancer-related deaths. This figure is likely to increase as the population ages and more countries join the European Union from Eastern Europe, where smoking rates are higher (Bray *et al.,* 2003; Coleman *et al.,* 2003; Quinn *et al.,* 2003; Levi *et al.,* 2004).

1.1 Lung cancer pathology

1.1.1 Risk factors

Lung cancer is a complex disease caused by a variety of factors. It involves genetics, the immune system, dose and duration of exposure to carcinogens, cellular irritation, DNA alteration, and many more factors (Abdel-Rahman *et al.,* 1998; Amos *et al.,* 1999; Lam *et al*., 1999). Smoking, particularly cigarette smoking, is the major cause of lung cancer, contributing to 70% of lung cancers. Exposure to carcinogens, which are present in tobacco smoke, immediately causes small changes to the tissue lining the bronchi of the lungs (the bronchial mucous membrane). This effect is cumulative; thus, with continued exposure, more tissue gets damaged, until a tumor develops (Lam *et al.,* 1999; Rojas *et al.,* 2004). Furthermore, passive smoking, or inhalation of another's exhaled smoke, has recently been identified as a more common cause of lung cancer in non-smokers than previously believed (Schwartz *et al.,* 1999). However, the incidence of lung cancer deaths not associated with smoking or other environmental factors (e.g., asbestos, radon, nickel, and coal tar products) is increasing at a higher rate than that of any other group. This effect appears to be linked with diet, infection, and inflammatory diseases (Steenland *et al.,* 1997; Jung *et al.,* 2000). Numerous studies suggest a correlation between lung cancer and a high

intake of cholesterol or incidence of viral or bacterial infections such as Chlamydia pneumoniae (Ignacio *et al.,* 1998; Nyberg *et al.,* 1998; Littman *et al.,* 2004).

1.1.2 Pathological processes

Lung cancer, the final step in a series of morphological and structural changes occurring over several years, is caused by carcinogens. These carcinogens affect DNA via several molecular mechanisms, producing mutations at multiple sites of the epithelial lining of the lung (Roland *et al.,* 1998). These mutations provide the cell with a proliferative advantage over nonmutant epithelial cells and promote clonal expansion to form a preneoplastic lesion. Lesions, when subjected to further mutations, transform into more malignant invasive cancer phenotypes (Lee *et al.,* 1998; Rubens *et al.,* 2002).

Mutations causing tumors occur mainly in genes that contain instructions for regulating cell growth and differentiation. Both the activation of proto-oncogenes and regression of tumor suppressor genes are likely to be the earliest steps in the development of lung cancer (Liotta *et al.,* 1991). Proto-oncogenes are important for the regulatory mechanisms of growth, cell-cycle control, programmed cell death, and terminal differentiation. Abnormal expression of these genes by point mutations, translocation, or DNA amplification may confer tumorigenicity. In addition, oncogene products, through the gain of function mutations, are positive effectors of transformation (Bouck *et al.,* 1990). Overexpression of oncogenes such as K-*ras* and c-Myc was particularly observed in the development of lung cancer (Rodenhuis *et al.,* 1990; Prins *et al.,* 1993; Lorenz *et al.,* 1994).

Unlike classical oncogenes, tumor suppressor genes are oncogenic through loss, rather than activation of function. The most commonly altered tumor suppressor gene, p53, is almost always defective or downregulated in most cases of lung cancer (Halevy *et al.,* 1990; Hollstein *et al.,* 1991).

However, alterations in both oncogenes and tumor suppressor genes instruct the cells and their offspring to reproduce at a dramatic rate, without regard for the normal shape and function of the lung. This unregulated reproduction causes the formation of tumors that may block air passages in the lung. In most cases, tumors arise in the bronchial mucosa and invade the bronchial wall. Additionally, tumors may grow around the bronchus, subsequently obstructing the bronchial lumen. Obstruction of

the lumen leads to collapse and often infection of the lung distal to the tumor (Rubens *et al.,* 2002).

Furthermore, lung cancers can metastasize to remote sites by blood or lymphatics. Metastatic spread is a multistep process that distinguishes benign tumors from invasive tumors (Chambers *et al.,* 2002). The first site of tumor metastasis is usually the lymph nodes within the lungs and the mediastinum; in later stages, tumors can spread to virtually any other organ.

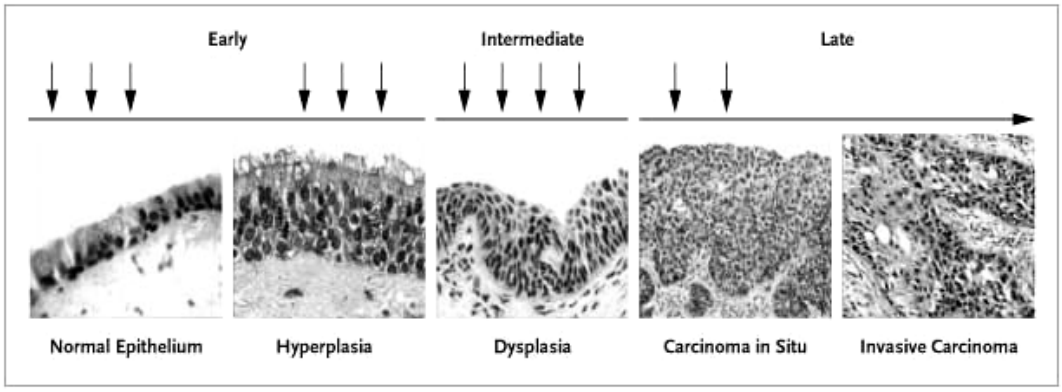

Figure 1: Sequential pathogenic changes involved in lung cancer: Although multiple genetic markers (indicated by the arrows) are abnormal in lung cancers, the timing of their appearance during the lengthy preneoplastic process varies. Several alterations have been described in histologically normal specimens of bronchial epithelium from smokers. Other changes (such as hyperplasia and metaplasia) have been detected in slightly abnormal epithelium and are regarded as early changes. Molecular changes, detected frequently in dysplasia, are considered intermediate in timing, whereas those usually detected in carcinoma in situ or invasive stages are regarded as late changes (Hirsch *et al.,* 2001).

1.2 Classification

Primary tumors are classified based on their histological appearance and presumed tissue of origin: epithelium, lymphatics, mesothelium, soft tissue, or miscellaneous. However, mixed tumors exist and are often classified according to the most predominant cell type found.

Tumors derived from epithelium are by far the most common and diverse. Based on their morphological appearance, epithelial tumors are further classified into two major groups: small and non-small cell lung cancer (Kreyberg *et al.,* 1982; Beadsmoore *et*

al., 2003). Small cell lung carcinoma (SCLC) is the less common form of lung cancer, making up 20% of cases. SCLC often starts in the larger breathing tubes and grows rapidly.

Non-small cell lung cancer (NSCLC) accounts for 75-80% of all lung cancer cases and is classified into three types:

- **Adenocarcinoma** represents the largest number of lung cancers (35%-40%) and usually arises in the outlying areas of the lung.
- **Squamous cell cancer** represents 25%-30% of lung cancers. It also starts in the larger airways but grows slower, meaning that the size of these tumors varies when diagnosed.
- **Large cell carcinoma** is found in approximately 10%-15% of lung cancer cases. It is a fast-growing form that grows near the surface of the lung.

Other rare types of cancer may be found, although they represent a very small percentage (less than 5%) of the total number of lung cancer cases, which includes adenosquamous carcinoma, sarcomatoid carcinoma, carcinoid tumor, and salivary-gland tumors (Travis *et al*., 2004; Beasley *et al.,* 2005).

This classification, although based on simple pathomorphological criteria, has very important implications for both clinical management and prognosis of the disease.

1.3 Treatment and prognosis

The prognosis for lung cancer is poor, showing little improvement over the past twenty years. Furthermore, small cell lung cancer and non-small cell lung cancer are treated in different manners. In essence, the stage of the disease plays a major role in deciding these treatment options.

1.3.1 Staging

As described, treatment for non-small cell lung cancer depends primarily on the stage of the cancer. Staging classification is mainly based on the results of pulmonary X-rays, CT-scans of the thorax and upper abdomen, bronchoscopy, and, in elective cases, mediastinoscopy. The classification follows the recommendations from Union Internationale Contre le Cancer (UICC) and is first categorized by the size and spread

or extension of the tumor, such as relation to main bronchus or thoracic wall, node involvement, and metastases (Beahrs *et al.,* 1992; Sobin *et al.,* 1997). This identification method is called the TNM system. The TNM system is used to determine the stage (numbered 0 to IV) of the tumor. The four stages, based on the TNM classification described below, provide a consistent and reproducible classification for describing the extent of disease (Mountain *et al.,* 1997; Beadsmoore *et al.,* 2003).

However, the TNM system is not used in the practical management of small cell lung cancer, mainly because of the overt metastatic disease often observed at diagnosis in the majority of patients. Hence, these cancers are broadly classified into two categories: extensive and limited stage disease. Limited stage disease is defined as cancer confined to the hemithorax of origin, the mediastinum, and the supraclavicular nodes. With extensive stage disease, the tumor is widespread; patients with distant metastases are always included in this group (Beadsmoore *et al.,* 2003).

Staging of Lung Cancer.*

Stage	Tumor	Node	Metastasis	General Description	Survival Rate 1 Yr	5 Yr
Non–small-cell lung cancer						
Local						
IA	T1	N0	M0	T1 tumor: ≤3 cm, surrounded by lung or pleura; no tumor more proximal than lobe bronchus	94	67
IB	T2	N0	M0	T2 tumor: >3 cm, involving main bronchus ≥2 cm distal to carina, invading pleura; atelectasis or pneumonitis extending to hilum but not entire lung	87	57
IIA	T1	N1	M0	N1: involvement of ipsilateral peribronchial or hilar nodes and intrapulmonary nodes by direct extension	89	55
Locally advanced						
IIB	T2	N1	M0		73	39
	T3	N0	M0	T3 tumor: invasion of chest wall, diaphragm, mediastinal pleura, pericardium, main bronchus <2 cm distal to carina; atelectasis or pneumonitis of entire lung		
IIIA	T1	N2	M0		64	23
	T2	N2	M0			
	T3	N1	M0			
	T3	N2	M0	N2: involvement of ipsilateral mediastinal or subcarinal nodes		
IIIB	Any T	N3	M0	N3: involvement of contralateral (lung) nodes or any supraclavicular node	32	3
Advanced						
IIIB	T4	Any N	M0	T4 tumor: invasion of mediastinum, heart, great vessels, trachea, esophagus, vertebral body, carina; separate tumor nodules; malignant pleural effusion	37	7
IV	Any T	Any N	M1	Distant metastasis	20	1
Small-cell lung cancer						
Limited disease				Evidence of tumor confined to ipsilateral hemithorax; can be encompassed by a single radiation port		
Extensive disease				All other diseases, including metastatic disease		

* Data are adapted from Mountain and Dresler.[7] The staging system was developed by the American Joint Commission on Cancer. T denotes tumor, N node, and M metastasis.

Table 1: International staging system for lung cancer: The tumor, node, metastasis (TNM) international staging system for lung cancer, developed by the American Joint Committee on Lung Cancer (Mountain *et al*., 1997).

1.3.2 Management

Depending on the type and stage of the disease, lung cancer can be treated with surgery, chemotherapy, radiation therapy, or a combination of these treatments. In the absence of treatment, tumor progression in SCLC is rapid, with a median survival of 2 to 4 months. On the other hand, patients with untreated NSCLC, even some with widespread metastatic disease, may, in rare instances, live for 5 years. Thus, the therapeutic approaches to these groups of patients should differ.

1.3.2.1 Surgery

There are three surgical procedures commonly used to treat lung cancer: wedge resection, or segmentectomy (in which a small section of the lung is removed); lobectomy (in which an entire section is removed); pneumonectomy (which involves the removal of an entire lung). Surgery remains one of the main cures for about one third of patients with NSCLC (stages I, II, and a limited group of patients with stage IIIA) who have surgically resectable disease (Shah *et al.,* 1995; Wada *et al.,* 1996). In SCLC, however, surgery is not feasible, since most patients have either locally advanced disease or distant metastases.

1.3.2.2 Chemotherapy

Chemotherapy modestly improves the survival rate of patients whose tumors are somewhat more advanced and can also provide symptomatic relief. A program of chemotherapy before surgery produces objective tumor responses in about 80% of patients with SCLC, while response rates in NSCLC are lower and often incomplete, as approximately 70% of NSCLC tumors are unresectable at the time of diagnosis (Feigal *et al*., 1993). New drugs like taxanes (paclitaxel and docetaxel), camptothecins (topotecan and irinotecan), new anti-metabolites (such as gemcitabine and difluorodeoxycytidine), and anti-tubulin agents (vinorelbine) show promise in the management of NSCLC (Halme *et al*., 1997; Mattson *et al*., 1997; Giaccone *et al*., 1998).

1.3.2.3 Radiation therapy

When surgery is not the best option, 3D conformal radiation therapy system delivers the highest possible radiation dose targeted directly at the tumor. This method spares

normal tissues and reduces damage to other organs in the chest. Therefore, patients with tumors too extensive for surgery and without distant metastases are likely to benefit from radiotherapy. Radiotherapy elicits responses in about 90% of patients with SCLC and in about 50% of those with NSCLC (Noordijk *et al.,* 1988; Stewart *et al.,* 1998).

1.3.2.4 Combined modality therapy

Clinical trials and meta-analyses demonstrated that combination therapy with both chemotherapy and radiotherapy improves the therapeutic outcome in patients with locally advanced, unresectable stage III NSCLC over a single modality therapy (Taillade *et al.,* 2004; Pritchard *et al.,* 1996). Combined modality therapy given to these patients increased the median survival to 14 months and the 5 year survival rate to 20%, nearly three times that reported with radiation therapy alone (Roth *et al.,* 1998). Combination chemotherapy with etoposide/cisplatin prolongs survival and is well-tolerated among SCLC patients, particularly patients with limited disease (Pignon *et al.,* 1992; Arriagada *et al.,* 1994).

1.3.2.5 Targeted therapy

The limited success of classic chemotherapeutic agents has led researchers to focus on developing rationally targeted therapies aimed at the molecular mechanisms underlying lung tumorigenesis. Agents inhibiting various aspects of tumor protein trafficking and protein degradation, cell cycle regulation, angiogenesis, and antigenicity are currently under clinical investigation. For example, Tarceva™ (erlotinib)-an epidermal growth factor receptor (EGFR) blocker, in combination with a Celebrex® (celecoxib)-an anti-inflammatory medication, is currently under phase II trial for the treatment of stage IV disease lung cancer patients (Perez-Soler *et al.,* 2004).

In addition, the existence of hypoxia and necrosis also allows use of tumor-selective therapy in regions resistant to both chemotherapy and radiotherapy. Hypoxia (very low oxygen concentrations) in tumors is a consequence of insufficient vascularization, impaired microcirculation, and thus increased diffusion distances, subsequently leading to necrosis and tumor cell death (Dang *et al.,* 1999; Hockel *et al.,* 2001). To counteract the possible deleterious effects of hypoxia, an immediate molecular

response is initiated, causing adaptation responses aimed at cell survival (Bunn *et al.,* 1996). This response is mediated by the hypoxia-inducible factor-1 (HIF-1), a heterodimer consisting of an α- and a β-subunit. HIF-1α protein, which is stabilized under hypoxic conditions, dimerizes with HIF-1β and transactivates target genes, including genes related to cell proliferation, cell survival, apoptosis, angiogenesis, vascular tone regulation, energy metabolism, oxygen transport, cell adhesion, and cell motility (Semenza *et al.,* 1992, 1996; Wang *et al.,* 1995). Several HIF-responsive genes are upregulated in human malignancies (Zhong *et al.,* 1999; Talks *et al.,* 2000). The role of HIF-dependent gene expression in tumor growth was well-demonstrated, but the correlation between HIF-1α overexpression and adverse clinical outcome of specific tumor disease is not identical. Overexpression is associated with both increased and decreased mortality (Semenza *et al.,* 2003). Controversial reports abound concerning the role of HIF-1 pathway in lung cancers. We address this issue in a mouse model of adenocarcinoma, a common form of lung cancer.

1.3.2.6 Immunotherapy

Host defense mechanisms may play an important role in diminishing tumors. Defects in immune response in patients with a variety of tumors and in tumor-bearing animals have been well-documented. In addition, several features of tumor cells may also limit the effectiveness of immune stimulation (Boon *et al.,* 1997; Gilboa *et al.,* 1998; Timmerman *et al.,* 1999; Rosenberg *et al.,* 2001) that includes active ‘tolerance’ of T-cells, resulting from an inadequate presentation of tumor associated antigens (TAAs) on the tumors.

Two different cell-based immunomodulatory strategies to improve the presentation and effectiveness of TAAs against tumors have been investigated. The first strategy involves antigen presenting cells, modified to either present specific tumor antigens to immune effector cells or to be more efficient in eliciting an anti-tumor immune response. A second strategy involves genetic modification of T-cells to alter their antigen specificity and increase their responsiveness to tumor antigens.

Dendritic cells (DCs) are the most efficient antigen presenting cells. They induce activation and proliferation of both naive CD8+ cytotoxic T lymphocytes (CTLs) and CD4+ T-helper (Th) cells, generating an anti-tumor response. (Porgador *et al.,* 1995; Brossart *et al.,* 1997; Ohshima *et al.,* 1997; Shen *et al.,* 1997; Nair *et al.,* 1998). Lack

of tumor antigen presentation by DCs in vivo might prevent the host immune system from eradicating most immunogenic tumors (Schuler *et al.,* 1997). Increasing evidence indicates that dendritic cells, pulsed with specific tumor antigen peptides or tumor extracts in an attempt to load tumor peptides into the major histo- compatibility complex (MHC) for presentation to T-cells, encourage a more potent anti-tumor response. However, these methods suffer from drawbacks such as transient presentation to single, known TAAs.

Considering the heterogeneous expression and undefined nature of TAAs, other Ag presentation systems have been developed to stimulate polyclonal immune responses against multiple tumor associated proteins by co-culturing DCs with attenuated tumor cells, tumor lysates, or transfecting with tumor derived RNA (Boczkowski *et al.,* 1996; Nair *et al.,* 1997, 1998; Celluzzi *et al.,* 1998; Nestle *et al.,* 1998) or fusion with tumor cells. However, fusion of tumor cells and DCs are most efficient in inducing a host T cell-mediated anti-tumor response. This is most likely due to the expression of MHC class I and class II antigens, as well as co-stimulatory molecules, on the DC-tumor cell chimera. However, the efficiency of fusion hybrids in eliciting tumor specific immune responses against lung carcinomas has not yet been demonstrated.

1.4 Animal models of lung cancer

Late diagnosis and inadequate knowledge about tumor progression and its associated molecular alterations pose significant problems in the treatment of lung cancer patients. To this end, appropriate and evolving animal models that mimic human disease paradigm in terms of genetic alterations and histological characteristics should be developed. Such experiments have been performed largely on mice, which could safely replace the more costly and time-consuming large animal studies in dog and monkey models. Because they readily mimic human lung cancers, mouse models facilitate the development of novel therapeutic approaches and methods for early diagnosis. To date, several approaches have been taken in the development of murine lung cancer models.

1.4.1 Spontaneous tumor models

Spontaneous and carcinogen induced tumors are either idiopathic or arise following carcinogenic or viral exposure in sensitive mouse strains such as A/J and SWR to

mimic the clinical situation most closely (Tuveson *et al.,* 1999). However, due to significant obstacles to the use of such model systems, new models must be developed for widespread use in experimental therapeutics.

1.4.2 Transplantable animal tumor models

1.4.2.1 Xenograft model

Early passages of transplanted tumors most closely resemble spontaneous cancer. These tumors can be transplanted into mice via various routes: subcutaneous, intraperitoneal, intratracheal, or intravenous, each with specific advantages and limitations (McLemore *et al.,* 1988; Gazdar *et al.,* 1997). These early passages show significant heterogeneity in cell kinetics and histology. Despite these changes, the majority of xenografted human tumors maintain the morphologic and biochemical characteristics of their original tumors. In fact, strong correlations can be made between average growth delay for human tumors in immunodeficient mice treated with the best available drug combinations and complete clinical response rates (Giovanella *et al.,* 1983). In increasing order of responsiveness, these correlations have been shown for human xenografts of non-small cell lung cancer, colon cancer, breast cancer, and malignant melanoma.

1.4.2.2 Orthotopic xenograft model

The orthotopic xenograft model is another transplanted system in which tumor cells are implanted at the site of the organ of origin. This organ-specific site presumably provides the tumor cells with an optimal environment for growth and progression and may reflect the clinical situation most closely. However, this model yields a high mortality rate (Jerald *et al.,* 1999; Tuveson *et al.,* 1999).

1.4.3 Genetically engineered animals

Many different genetically engineered mouse models for lung cancer have been developed to identify the role of specific genes during transformation and disease progression. Constitutive or conditional transgenes can be targeted to the lung to regulate the expression and ablation of genes. This allows the generation of animal models that represent a better paradigm for cancer development than the widely used xenograft model. This technology, however, is limited by the number of tools

available to direct these genetic events to many of the cell types clinically important for lung cancer (Kwak *et al.*, 2004).

On the other hand, the development of mouse models is complicated by the cellular diversity of lung cancer. Therefore, the success of establishing mouse models for lung cancer will depend upon the ability to target the specific oncogenic genetic modification in a cell-specific fashion. We attempted to establish orthotopic xenograft mouse models for adenocarcinoma and lewis lung carcinomas in order to study the underlying molecular mechanisms, to develop novel therapeutics, and to develop methods for early detection.

1.5 Imaging techniques

Another significant problem in the treatment of lung cancer patients is late diagnosis. Unfortunately, the 5-year survival rate for lung cancer ranges between 5%-10%, primarily because most patients are diagnosed with advanced-stage disease. However, when lung cancer is diagnosed and resected at an early stage, the survival rate may be as high as 80%.

Nevertheless, a group of new techniques known collectively as “molecular imaging” now offers scientists an unprecedented opportunity to significantly improve the detection of localized lung cancer, better understand tumor biology, improve diagnosis, enhance treatment, and consequently reduce mortality. These imaging modalities explore the utility of spiral computed tomography (CT), high magnetic field magnetic resonance imaging scanners (MRI), PET imaging, fluorescence bronchoscopy, and the proteomic and genomic analysis of tumors and other specimens. These approaches (in particular, the application of CT) have the potential to identify small and early lesions that have not been readily detectable in clinical practice through more conventional methods.

Helical or spiral CT is a radiographic method that can provide within short scanning times high quality, three-dimensional images of the lungs and lung nodules during a single breath-hold. Helical CT is more sensitive than chest x-ray and can often detect lung nodules as small as 5mm in diameter in humans. However, the resolution of conventional CT-systems is not sufficient for scanning and quantitative monitoring of lung disease in small animal models. Furthermore, the CT technique suffers from poor soft tissue resolution, though visualization of the lung tissue means imaging in high

contrast. The recent development of high resolution CT imaging such as of micro computed tomography (μCT) has not solved the problem of poor contrast; however, the higher resolution makes the technique suitable for small animal imaging. Micro-CT systems provide resolution down to 10 μm, but there is a trade-off between resolution, field of view, and radiation dose.

The successful development of tumor models with human cell lines and the availability of novel therapeutic approaches like anti-angiogenic or genetic therapies increase the need for advancement in high resolution in vivo imaging in small animal models for tumor screening and volumetry. Beyond morphology at a definite time-point, follow-up studies play a critical role in cancer research. Therefore, imaging systems offering a high resolution in time and space have to be provided. The applicability of high resolution Magnetic Resonance Imaging (MRI) systems for this purpose has been already demonstrated. Long acquisition times and limitation to a small field-of-view dependent on the required resolution disqualify the system for quantitative and longitudinal monitoring of small lung nodules.

In this context, we introduced the novel high resolution micro-computed-tomography (μCT) and flat-panel volumetric Computed Tomograph (fpvCT) for in vivo small animal imaging to gain novel insights into lung tumor evolution and processes and to monitor therapeutic effects.

2. Aims

This thesis was guided in its formation by the following goals.

- Establishment of lung mouse tumor models.
- Analysis of the role of HIF-1α in the adenocarcinoma mouse model.
- Study of tumor regression capabilities by dendritic/tumor cell hybrid-primed T-lymphocytes and hybrid vaccination in a lewis lung carcinoma model.
- Application of new imaging strategies in order to monitor tumorogenesis and tumor metastasis in vivo over time (multislice computed tomography, micro-computed tomography, and flat-panel volumetric computed tomography).
- Use of the imaging techniques to delineate vessel architecture (vascularization) and blood supply of lung tumors.

3 Materials and Methods

3.1 Cell biological methods

3.1.1 Culture of human A549, mouse LLC1 and mouse B16/F10 cells

LLC1-mouse lewis lung carcinoma, B16/F10-mouse melanoma, and A549-human lung adenocarcinoma cell lines were obtained from American Type Culture Collection (ATCC, Manassas, VA, USA).

LLC1 cells were maintained in RPMI-1640 medium supplemented with 2% FBS, penicillin (100 U/ml), and streptomycin (0.1 mg/ml) at 37°C in humidified atmosphere containing 5% CO_2.

B16/F10 cells were maintained in DMEM/F12 medium supplemented with 10% FBS, penicillin (100 U/ml), and streptomycin (0.1 mg/ml) at 37°C in humidified atmosphere containing 5% CO_2.

A549 cells were maintained in DMEM/F12 medium supplemented with 10% FBS, penicillin (100 U/ml), streptomycin (0.1 mg/ml), 1% MEM vitamin solution, 2 mM glutamate and 1% non-essential amino acids at 37°C in humidified atmosphere containing 5% CO_2.

RPMI-1640 and DMEM/F12 media were purchased from PAN Biotech GmbH (Aidenbach, Germany). FBS was obtained from Greiner BioOne (Frickenhausen, Germany). Penicillin, streptomycin, MEM vitamin solution, glutamate, and non-essential amino acids all were purchased from Gibco (Eggenstein, Germany).

3.1.2 Cell culture and generation of HIF-1α overexpressing cells

A549 cells were transfected with pMG-HIF-1α or empty pMG plasmid (as control) with Lipofectamine 2000 (Invitrogen, Carlsbad, CA, USA) for 6 h according to the manufacturer's recommendations. Cells were treated with medium containing 750 µg/ml hygromycin B (Roche, Indianapolis, IN, USA) 24 h post-transfection. The medium containing hygromycin B was replaced every 48 h for two weeks. After two weeks, the concentration of hygromycin B was reduced to 500 µg/ml, and incubation was continued for two more weeks. Ultimately, cells were maintained continuously in 350 µg/ml hygromycin B (Goyal *et al.,* 2004).

3.1.3 Hypoxia treatment

A549 cells were exposed to hypoxic conditions in a chamber equilibrated with a water-saturated gas mixture of 1% (v/v) oxygen, 5% (v/v) carbon dioxide, and 94% (v/v) nitrogen at 37°C. Control cells were maintained under normoxic conditions in water-saturated room air, supplemented with 5% (v/v) carbon dioxide at 37°C.

3.1.4 Immunocytochemistry of HIF-1α

The A549 cells selected for hygromycin resistance were grown on chamber slides and treated as indicated. Cells were removed and fixed immediately in acetone:methanol (1:1). The fixed cells were incubated overnight at 4°C in 100 µl phosphate-buffered saline (PBS; Gibco, Eggenstein, Germany) containing an anti-human HIF-1α mouse monoclonal antibody clone 54 (1:100, BD Biosciences, Heidelberg, Germany). Indirect immunofluorescence was conducted by incubation with fluorescein isothiocyanate (FITC)-conjugated rabbit anti-mouse IgG antibodies (1:100, DAKO, Glostrup, Denmark) in 100 µl PBS. Coverslips were mounted on glass slides and subjected to microscopic analysis (Hanze *et al.,* 2003).

3.1.5 Hypoxia-responsive element reporter gene assay

A dual reporter gene assay for studying HIF-1α dependent gene regulation was performed. One vector, carrying a firefly luciferase gene and controlled by a three-tandem repeat of the HRE coupled to a thymidine-kinase minimal promoter (TK-MP) from Herpes simplex, was co-transfected with a second reporter vector carrying a renilla luciferase gene controlled by the TK-MP promoter without HRE. The values represent the ratio of chemiluminescence measured for firefly and renilla, respectively, thus giving the HRE specific luciferase activation. Hypoxic-responsive promoter constructs were prepared as previously described (Goyal *et al.,* 2004). The HRE-TK-MP and pRL-TK-MP plasmids were transfected in a molar ratio of 3:1 into A549 cells by Lipofectamin 2000 according to the manufacturer's protocol (Invitrogen, Carlsbad, CA, USA) in a 48-well plate. Transfected cells were incubated for 6 h in FCS-containing medium and then replaced by serum-free medium for 24 h in normoxic and hypoxic conditions. The cells were lysed in 4°C luciferase lysis buffer (Promega, Mannheim, Germany), and firefly and renilla luciferase activities

were measured by a bioluminometer (TEKAN, Crailsheim, Germany) (Hanze *et al.*, 2003; Goyal *et al.*, 2004).

3.1.6 Determination of vascular endothelial growth factor (VEGF) concentration

Subconfluent A549 cells, selected for hygromycin resistance, were grown in 100-mm petri dishes with 10 ml of fresh medium for 24 h, either under normoxic or hypoxic conditions, as in 3.1.3 methods section. Cell supernatants were collected, clarified by centrifugation at 2000 rpm for 5 min, and stored at -20°C. Concentrations of VEGF in supernatants were determined with an ELISA kit (R & D Systems, Minneapolis, MN, USA) following the manufacturer's guidelines. Samples were analyzed in duplicate, human recombinant VEGF165 diluted in series and used as a standard. VEGF concentrations were measured according to the standard curve. Concentrations were calculated using a standard curve generated with specific standards provided by the manufacturer. The VEGF concentration was expressed as pg of VEGF/ml of medium, and per mg of total protein.

3.1.7 MTT assay

The MTT (3-(4, 5-dimethylthiazol-2-yl)-2, 5-diphenyltetrazolium bromide) assay was performed to evaluate the effects, if any, of hypoxia and normoxia on A549 cell viability and density, as in Section 3.1.3. Cells (2×10^3) were seeded in 96-well plates, and the medium was replaced by a fresh serum-free medium. Cells were then exposed to hypoxic or normoxic conditions for 1, 2, 4, 6, and 8 days. At the end of this period, 0.2 mg/ml MTT (Roche, Mannheim, Germany) was added to each well, and incubation continued for 1-2 h at 37°C. The extent of MTT reduction to formazan within cells was quantified spectrophotometrically (TEKAN, Crailsheim, Germany) at 490 nm and taken as an indicator of cell viability.

3.1.8 Thymidine incorporation

Cells were incubated in a serum-free medium in the presence of ^{3}H-thymidine (Amersham Pharmacia Biotech UK Ltd., Buckinghamshire, England) (1.5 µCi/100 µl) for 18 h. After aspiration of unincorporated extracellular tracer, cells were washed extensively and incubated in ice-cold 5% (v/v) trichloroacetic acid (TCA; Sigma,

Deisenhofen, Germany) for 30 min. After the removal of TCA, cells were lysed with 0.5 M NaOH. Finally, cells were removed from the wells and resuspended in 5 ml of scintillation mixture (Roth, Karlsruhe, Germany) for radioactive counting. Vials were vortexed thoroughly before radioactive counts were measured by scintillation counter (Canberra Packard, Dreieich, Germany). Counts were measured in dpm (disintegrations per minute).

3.1.9 Soft- agar colony-formation assay

Anchorage-independent proliferation was examined using soft agar (Barr *et al.,* 2000). Cells (1×10^4/well) were suspended in 200 µl of 0.35% (v/v) agar in DMEM/F12 medium supplements with 10% (v/v) FCS, penicillin-streptomycin, L-glutamine, and hygromycin B, layered above 200 µl of 0.7% (v/v) agar, and overlaid with 200 µl in 24-well plates. Six plates were incubated at 37°C for 2 to 3 weeks and imaged by light microscopy (20X magnification) in three different non-overlapping views to detect colonies. A colony was defined as a group of more than 15 cells.

3.1.10 Generation of bone marrow derived dendritic cells

Erythrocyte-depleted C57/BL6 mouse bone marrow cells flushed from marrow cavities of femurs and tibias were cultured in RPMI-1640 medium supplemented with 1000 U/ml of both GMCSF (Pepro Tech EC Ltd., London, England) and IL-4 (Strathmann Biotec AG, Hamburg, Germany) and 100 µg/ml of FLT3 (Pepro Tech EC Ltd., London, England) (van den Broeke *et al.,* 2003). On day 6, non-adherent cells were collected and replated in new petri dishes with RPMI-1640 medium supplemented with 10 µg/ml LPS (Sigma, Deisenhofen, Germany). On day 10, these non-adherent cells were removed and stained with anti-mouse CD11c monoclonal antibody clone HL3 (1:100; Pharmingen, Heidelberg, Germany) for confirmation of DC phenotype.

3.1.11 DC/ Tumor fusion cell preparation

Fusion of bone marrow derived DCs and LLC1 cells were performed as previously described with slight modifications (Banat *et al.,* 2004). DCs were stained red using PKH-26-Gl, and tumor cells (LLC1 cells) were stained green using PKH-67-GI

fluorescent cell linker kits (Sigma, Deisenhofen, Germany) according to the manufacturer's instructions. After removing the unbound dye, LLC1 cells were transferred into an electroporation cuvette and pulsed at 200 V/cm and 200 µs using a Gene Pulser (BioRad, Hercules, CA, USA). Treated LLC1 cells and DCs were then mixed at a ratio of 2:1 and incubated in serum-free RPMI-1640 medium containing 50% polyethylene glycol (PEG; Sigma, Deisenhofen, Germany) by stirring for 2 min. An additional 7 ml of serum-free RPMI-1640 medium was added to the cell suspension over the next 3 min with continued stirring. Then, the cells were washed and resuspended in serum-free RPMI-1640 medium and incubated at 37°C in a humidified atmosphere (5% CO_2).

3.1.12 Fusion efficiency and fluorescence-activated cell sorting

After 48 h of culture, fusion efficiency was assessed by fluorescence microscopy. LLC1 cells revealed green fluorescence; DCs, red fluorescence; and LLC1/DC fused cells (Hybrids) showed yellow fluorescence. Fusion hybrids demonstrated viability over 90%, as documented by lack of propidium iodide uptake.

Fusion efficiency was also determined by counting the proportion of double stained cells. In addition, cells were also analyzed for fusion efficiency by labeling with CD11c, B7.1 and MHC class II. After 48 h of culture, fused mixtures were collected and resuspended in PBS (PAA Laboratories GmbH, Linz, Austria) at a concentration of 1 x 10^6 cells/ml for sorting. Hybrid cells (dual color) were gated and sorted using fluorescence-activated cell sorting (FACS) Calibur (Becton Dickinson, Heidelberg, Germany). The sorted cells, displaying both green and red fluorescence, were harvested and resuspended in medium for in vitro and in vivo assays.

3.1.13 Proliferation assay for spleen and lymph node cells

Spleens and lymph nodes were excised, pushed through fine gauze, and freed from debris and dead cells by Ficoll Hypaque density-gradient centrifugation (Amersham Pharmacia Biotech, Freiburg, Germany). Isolated spleen cells (SC) and lymph node cells (LNC) (1 x 10^5 cells/well) were seeded onto 96-well round bottomed microplates. Irradiated LLC1 cells, syngeneic purified fusion Hybrids, syngeneic DCs, mixture of syngeneic DC/LLC1 cells, syngeneic DC/LLC1 lysate or allogeneic lymphocytes (Balb/c) were added as stimulator cells at 1 x 10^4 cells/well in triplicates.

The final volume of each well was adjusted to 200 µl with complete medium. Triplicate wells of lymphocytes or stimulator cells alone were used as background controls. Cells were assessed for incorporation of tritiated thymidine (3H-TdR) on days 3 and 5 of culture by adding 37 kBq/well. After 6 h, the cells were harvested onto glass filters, and ß-emission was counted using a scintillation counter (Canberra Packard, Dreieich, Germany). The results were expressed as mean counts per minute (cpm) $x10^3$ ± SD of triplicate cultures. Proliferative activity is displayed as a proliferation index (radioactivity (cpm)) in test wells divided by that in control wells containing responder cells only (Banat *et al.,* 2001).

3.1.14 Cytotoxic assays for spleen and lymph node cells

Isolated SC/LNC lymphocytes were co-cultured with irradiated LLC1 cells, syngeneic purified fusion hybrids, allogeneic T lymphocytes (Balb/c), or syngeneic B16/F10 tumor cells as targets in various ratios. Cytotoxicity was measured in vitro using the standard cell dilution analysis method (Pechhold *et al.,* 1994). Briefly, K562 (human chronic myeloid leukemia in blast crisis) cells were obtained from the German Collection of Microorganisms and Cell Cultures (DMSZ, Braunschweig, Germany) and stained with PE-conjugated anti-human CD13 mouse monoclonal antibody clone WM15 and anti-human CD33 mouse monoclonal antibody clone WM53 (1:100, Pharmingen, Heidelberg, Germany) were fixed in PBS containing 4% paraformaldehyde (PFA; Merck, Darmstadt, Germany) and used as fixed standard cells (SC). Aliquots of T lymphocytes/target mixture were stained after 4, 12, or 16 h of culture in v-shaped 96-well plates with FITC-conjugated anti-mouse CD4 rat monoclonal antibody clone GK1.5, anti-mouse CD8 rat monoclonal antibody clone 53-6.7, anti-mouse CD16/CD32 rat monoclonal antibody clone 2.4G2, and anti-mouse NK1.1 mouse monoclonal antibody clone PK136 (1:10, all from Pharmingen, Heidelberg, Germany) for 30 min. After washing, the cells were resuspended in 100 µl standard cell dilution analysis (SCDA) buffer, consisting of PBS supplemented with 1% BSA (Sigma, Deisenhofen, Germany), 10^5 fixed SC, and 0.2 µg/ml propidium iodide. Cells were then analyzed immediately by flow cytometry. Absolute cell numbers were determined by the linear correlation between stained T lymphocytes, unstained target cells, and the absolute number of SC per sample.

Percentage cytotoxicity was calculated according to the formula: % cytotoxicity =1-$LLC1_a/SC_a$ X $SC_b/LLC1_b$ X 100, where $LLC1_a$ are propidium iodide negative LLC1 cells in the effector-target co-culture, SC_a are standard cells in the effector-target co-culture, SC_b are standard cells in the LLC1/SC control, and $LLC1_b$ are propidium iodide negative LLC1 cells in the LLC1/SC control.

3.2 Animal studies

3.2.1 Animals

Female C57/BL6 (H-2^b), female BALB/c (H-2^d), and male immunodeficient CD-1 *nu*/*nu* mice aged 3–5 weeks were purchased from Charles Rivers, Sulzfeld, Germany, kept under pathogen-free conditions, and handled in accordance with the European Communities recommendations for experimentation.

3.2.2 Tumorigenicity in nude mice

Tumorigenicity was assessed by subcutaneous injection of A549 cells (2.5×10^6 cells/200 µl in saline) into 4-week-old male CD-1 *nu*/*nu* male mice. The size of the tumor was measured using digital calipers (Mitutoyo, Tokyo, Japan). The tumor volume (TV) was calculated by the formula: TV (mm^3) = $(L \times W^2)/2$, where L is the longest dimension of the tumor (in mm), and W is the shortest dimension of the tumor (in mm). After 8 weeks, the mice were sacrificed, and tumors were prepared and embedded in tissue tek (Tissue Tek; Sakura, Torrance, CA, USA) and stored at –80 °C.

3.2.3 Immunization

C57/BL6 mice were immunized twice in a 1-week interval by intra-footpad injection of 2 x 105 irradiated (6,000 Rad) LLC1, DCs, DC/LLC1, DC/LLC1 lysate, Hybrids or PBS alone. Irradiation of cells was performed using irradiator OB 29 (STS GmbH, Braunschweig, Germany). Four days after the final immunization, each group of mice was injected subcutaneously with 1 x 10^6 viable LLC1 cells/mouse. Tumor growth and survival time were recorded for each group of ten mice. Mice were inspected weekly for tumor growth. Size of the tumor was measured as described in Section

3.2.2. After 4 weeks, mice were sacrificed, and SC/LNCs were isolated as in 3.1.13 and taken for proliferation and cytotoxicity assays.

3.2.4 Pre tumor challenge

C57/BL6 mice were immunized intra-footpad twice in 2-week intervals with 2 x 10^5 irradiated LLC1, DCs, DC/LLC1, DC/LLC1 lysate, Hybrids or PBS alone. One week after the final immunization, each group of mice was injected subcutaneously with 1 x 10^6 viable LLC1 cells/mouse. Tumor growth and survival time were recorded for each group of ten mice. Mice were inspected weekly for tumor growth. Size of the tumor was measured as described in Section 3.2.2. After 4 weeks, mice were sacrificed, and SC/LNCs were isolated as in 3.1.13 and taken for proliferation and cytotoxicity assays.

3.2.5 Vaccine therapy

For post tumor therapy, 1 x 10^6 LLC1 cells were injected into C57/BL6 mice subcutaneously. On days 7 and 14, tumor-bearing mice were treated with 2 x 10^5 irradiated LLC1, DCs, DC/LLC1, DC/LLC1 lysate, Hybrids or PBS alone per mouse. Tumor growth and survival time were recorded for another 2 weeks. After these 2 weeks, mice were sacrificed and SC/LNCs were isolated as in 3.1.13 and taken for proliferation and cytotoxicity assays.

3.2.6 Adoptive immunotherapy

For therapy of LLC1 tumors, C57/BL6 mice were injected subcutaneously with 1 x 10^6 LLC1 cells/200 µl in saline to initiate tumor formation. Four days after tumor inoculation, mice were randomly divided into several groups to intravenously receive 1 x 10^7 spleen and lymph node cells, obtained from irradiated LLC1, DCs, DC/LLC1, DC/LLC1 lysate, Hybrids or PBS alone immunized and re-immunized mice. On day 12, mice from each group received a booster-dose of primed T-lymphocytes. Tumor growth and survival time of each group of mice were monitored and recorded on a regular basis for 4 weeks after tumor inoculation. After these 4 weeks, mice were sacrificed, and SC/LNCs were isolated as in 3.1.13 and taken for proliferation and cytotoxicity assays.

3.2.7 Intratracheal instillation

Sub-confluent LLC1 cells were treated with trypsin and EDTA (Gibco, Eggenstein, Germany) and resuspended in saline. For intratracheal instillation of cells, C57/BL6 mice were anaesthetized by intraperitoneal injection of a mixture containing 100 mg/ml ketamine (Ketavet®; Pharmacia & Upjohn, Erlangen, Germany) and 2% xylazine (Rompun®; Bayer, Leverkusen, Germany). Later, mice were suspended in a hanging position by a rubber band fixed to the incisor teeth of the upper jaw. The trachea was intubated via the oral cavity. A Vasocan® Braunüle® 20 G 1 ¼‘‘ (Braun Melsungen AG, Melsungen, Germany) tube was placed in the trachea, and the cells (1 x 10^6/0.1 ml saline) or saline were instilled into the lungs. Next, the mice were placed on a 37°C hot plate for 10-15 min to maintain temperature. Lung tumor growth was monitored and confirmed by using both fpvCT and Hematoxylin and Eosin (H&E) staining. For histological analysis, lung tissues were fixed in 4% formalin and embedded in paraffin. Three µm thick paraffin sections were stained with hematoxylin and eosin.

3.2.8 Infusion of fluorescent microspheres

After confirmation of tumor growth with fpvCT, animals were anesthetized as in 3.2.7. A polyethylene catheter was positioned either in the right ventricle, left ventricle, or in both ventricles, and infused with fluorescent microspheres to trace pulmonary and systemic blood flow (Wu *et al.,* 1988; Iwamaru *et al.,* 2001; Iwamaru *et al.,* 2003). Because the capillaries were 4-9 µm in diameter, 10 µm yellow and red fluorescent microspheres (Molecular Probes Inc., Eugene, OR, USA) were selected and diluted to the desired concentration with saline. Certofix Mono Complete Size 1 catheter (Braun Melsungen AG, Melsungen, Germany) was used for infusion. 1.5 x 10^5 yellow fluorescent microspheres (200 µl) were introduced into the right ventricle to trace pulmonary blood flow, and systemic blood flow was monitored with 1.5 x 10^5 red fluorescent microspheres (200 µl) introduced into the left ventricle. After the infusion of fluorescent microspheres, the catheters were flushed with saline containing 25000 IU/5 ml Heparin sodium (Roche, Mannheim, Germany). Later the animals were divided into two groups. One set of animals (n=12) was taken for histological

examination and the other set (n=12) for extraction and counting the number of fluorescent microspheres.

3.2.9 Tumor and lung tissue digestion and processing

After fluorescent microsphere infusion, lungs and tumors were separated under light microscopic view (Leica Instruments, Nussloch, Germany). Their wet weights and volumes were measured, and their digestion was performed as previously described (Iwamaru *et al.,* 2001; Iwamaru *et al.,* 2003). Lungs and lung tumors were separately placed into polypropylene tubes and digested with 7 ml of a 4 M KOH solution containing 0.05% Tween 80, in a water bath at 65°C until the tissue was completely dissolved. Homogenous samples were centrifuged (20 min, 2000 g), and the supernatant was drawn off, leaving < 1 ml behind. Left over pellet, containing fluorescent microspheres and some debris, was rinsed with 9 ml of 0.25% Tween 80 in demineralized water at 65°C, and centrifuged again at the same force and duration. After a final rinsing with demineralized water, the pellet was re-suspended in saline and analyzed for the number of fluorescent microspheres using a hemocytometer and fluorescent microscope as described in the FMRC manual (Fluorescent Microspheres Resource Center, University of Washington, WA, USA) (Bernard *et al*., 1996).

3.3 Imaging techniques

3.3.1 Flat-panel volumetric computed tomography

The flat-panel volumetric Computed Tomography (fpvCT) is a novel high resolution Computed Tomography (CT) system developed by General Electric (GE Global Research, Niskayuna, NY, USA). In contrast to clinical CT scanners, in the fpvCT, an amorphous silicon flat-panel detector is irradiated by a cone-shaped X-ray beam. Animals were anaesthetized as in 3.2.7. The mice were mounted on a patient table, which was moved into the gantry bore during the scan, while the x-ray tube and detector, mounted on a rotating gantry and rotated around the table. The scan was performed in a sequential rather than a helical mode. For our investigation, 120 kVp at 40 mA was used. The scanning time for one rotation was 8 seconds, covering a field-of-view of 4.2 cm in the z-direction, sufficient for scanning the thorax of one mouse. Projection images were reconstructed using a cone-beam algorithm and an edge-defining reconstruction kernel (Kalender *et al.,* 2003; Kiessling *et al*., 2004).

Data can be reconstructed at arbitrary voxel sizes, but $(0.05\ mm)^3$ isotropic voxels were used for this investigation. All data were transferred to an Advantage Windows Workstation 4.1 (GE Healthcare Europe, Buc, France) and processed with the Volume Rendering Software.

3.3.2 Multislice computed tomography

Multislice computed tomography (MSCT) imaging was carried out on a Somatom Plus 4 Volume Zoom scanner (Siemens, Erlangen, Germany) with parameters of 120 kV and 320 mAs. For image reconstruction, a high resolution kernel was applied (U90). Slices of 0.5 mm thickness and 0.5 mm spacing were acquired in a sequential scanning mode.

3.3.3 Micro computed tomography

For investigation using μCT, blood vessels were filled with a solidifying blood-pool contrast agent (Microfil; Flow Tech, Carver, MA, USA) forming a vascular cast. Under visual control, ready-made, non-diluted contrast agent was perfused manually using three different methods as described (Jorgensen *et al.,* 1998; Kwon *et al.,* 1998; Kantor *et al.,* 2000). i) The pulmonary vascular tree was completely filled by intravenous in vivo injection via the jugular vein. ii) The pulmonary arteries were filled down to the capillary level by direct injection of contrast medium into the main pulmonary artery ex vivo. iii) The aorta and the arterial vessels were filled by injecting contrast media into a catheter inserted through the left ventricle. After perfusion and solidification of the contrast medium, the lungs were removed and scanned with a desktop μCT unit (Skyscan1072, Sky scan, Belgium) that has been previously described (Langheinrich AC. *et al.,* 2004). In our setting, samples were positioned on a computer-controlled rotation stage and scanned over a half rotation (180°) with rotation steps of 0.675°, at 60 kVp, 100 μA. Raw data were reconstructed with a modified Feldkamp cone-beam reconstruction algorithm (Feldkamp *et al.,* 1989), resulting in 8-bit gray-scale images with $(6\ \mu m)^3$ isotropic voxels. Image processing and analysis were performed with the Analyze 6.0 software package (Analyze, Biomedical Imaging Resource, Mayo Foundation, Rochester, MN, USA).

3.4 Histological methods

3.4.1 Hematoxylin and Eosin (H&E) staining

Three to five µm thick sections were prepared from paraffin embedded tissue samples. The sections were de-paraffinized by incubation in xylene solution 3 x 5 min. Then the sections were fixed in acetone for 2 min on ice and incubated in 100%, 90%, and 70% ethanol, and finally in dist. H_2O, spending 3 min in each solution. Then the slides were incubated in fresh hematoxylin (Merck, Darmstadt, Germany) for 15 min and washed in dist. H_2O for 20 min. Next, the slides were incubated with freshly prepared Eosin solution acidified with acetic acid (Sigma, Deisenhofen, Germany) for 1 min. The slides were then washed with dist. H_2O for 5 min and dehydrated for 3 min per solution in 90% ethanol and 100% ethanol. Finally, the slides were air dried for 5 min and mounted with mounting medium.

3.4.2 Assessment of microvessel density

Detection of blood vessels was performed by immunohistochemistry for CD31. Frozen 5 µm tumor sections equilibrated to room temperature were fixed in acetone for 10 min. Endogenous peroxidases were blocked with 0.3% (v/v) hydrogen peroxide in methanol and then blocked with 5% (v/v) goat serum in PBS, followed by incubation with anti-mouse CD31 rat monoclonal antibody clone MEC13.3 (1:500, Pharmingen, San Diego, CA, USA). Sections were washed in PBS, and antibody binding was determined using a Vector ABC kit (Vector Laboratories, Burlingame, CA, USA). Negative control slides were obtained by omitting the primary antibody. After extensive washing, sections were stained with DAB and visualized under light microscopy. Areas of microvessel density were counted in a minimum of five microscopic fields with a 10X objective. Values were expressed as mean microvessels per field (Ravi *et al.,* 2000).

3.4.3 Apoptosis by cyto- and histochemistry

Apoptosis in cultured cells and tumor sections was visualized using the terminal deoxynucleotidyl transferase (TdT) - mediated dUTP- biotin nick end labelling (TUNEL) method (alkaline phosphatase *in situ* cell detection kit, Roche, Mannheim, Germany). Frozen sections were fixed in 4% (v/v) paraformaldehyde for 1h,

permeabilized using Triton X-100 (Sigma, Deisenhofen, Germany), and then incubated at 37°C for 60 min with TUNEL reaction mixture. The staining was performed according to the manufacturer's recommendations. The stained cells were viewed under the light microscope magnification 20X (Leica Instruments, Nussloch, Germany). Results, based on apoptosis, were indicated as the average number mean ratio of labelled nuclei to the total number of cells in five different fields (n=3).

Positive control of TUNEL labeling was prepared using DNase I (Sigma, St. Louis, MO, USA) treatment. After pretreatment, histological sections were incubated with DNase I (5 µg/ml) in a 37°C humidified chamber for 10 min to induce DNA strand breaks. Negative control was obtained by omitting terminal transferase from the labeling procedure.

3.4.4 Histology of fluorescent microsphere-infused lungs

For cryosections, the fluorescent microsphere-infused (Number) lungs were inflated with Tissue-tek (Sakura Finetechnical Co. Ltd., Tokyo, Japan) in 0.9% NaCl (1:1). Cryosections with 15 µm slice thickness were made for histological examination using a Leica-CM 1900 Cryostat Microtome (Leica Instruments, Nussloch, Germany). Color and location of fluorescent microspheres within the lung and lung tumors were detected using a fluorescent microscope equipped with an IMT2RFL Reflected Light Fluorescence Attachment (Olympus Optical Co., Hamburg, Germany) multi-wavelength fluorescent filter cube (Wagner *et al.,* 2002).

3.5 Molecular biological methods

3.5.1 Construction of expression plasmid for HIF-1α

For isolation of full length cDNA fragments of HIF-1α, we employed a nested RT-PCR from RNA extracts of A549 cells. For maximal translation efficacy, we inserted the Kozak sequence (GCCGCCACCATGG) at the start codon of translation. The full length HIF-1α cDNA (Acc. No. NM_001530) was ligated into expression vector pMG (Invivogen, San Diego, CA, USA) and verified by sequencing (ABI Prism 310; PE Applied Biosystems, Foster City, CA, USA) (Hanze *et al.,* 2003).

3.5.2 Real-time reverse transcription-polymerase chain reaction (RT-PCR)

Cellular RNA was extracted from A549 tumors (n=3) using guanidine thiocyanate-acid phenol (RNAzol B, WAK-Chemie, Germany). Approximately 2 µg of RNA per sample was copied to cDNA using reverse transcriptase (MMLV-RT) (Gibco-BRL, Karlsruhe, Germany) in a standard protocol with random hexamers. For the negative control, MMLV was omitted. Real-time PCR was performed using the ABI Prism 7700 Detection system (Applied Biosystem, Weiterstadt, Germany) with SYBR-Green as fluorescent dye, enabling real time detection of PCR products according to the manufacturer's protocol (Hanze *et al.,* 2003; Goyal *et al.,* 2004). The following primer sets (+, sense; -, antisense), derived from the respective Genebank sequences, were employed: HIF-1α (Accession No. NM_001530) HIF-1α +: 5′- CCA TTA GAA AGC AGT TCC GC-3′, HIF-1α -: 5′-TGG GTA GGA GAT GGA GAT GC-3′, VEGF (Accession No. NM_003376) VEGF +: 5′-GGA GTG TGT GCC CAC CGA GGA GTC CAA C-3′, VEGF -: 5′-GGT TCC CGA AAC CCT GAG GGA GGC T-3′, and HPRT (Accession No. NM_000194) HPRT +: 5′-TCG AGA TGT GAT GAA GGA GAT GGG A-3′, HPRT -: 5′-TCA AAT CCA ACA AAG TCT GGC TTA T-3′.

3.5.3 Gene expression array analysis

Total RNA was isolated from blood obtained from immunized mice, which were injected previously with DC, LLC1 cells, hybrids, or PBS alone. Biotin-16-dUTP labeled cDNA probes were generated from 5 µg of RNA using a GE Array non-radioactive Ampo Labeling-LPR Kit (Super Array Bioscience Corp., Frederick, MD, USA) and used to hybridize a GE Array Q series mouse common cytokine gene micro array (Super Array Bioscience, cat # MM-003) according to the manufacturer's instructions. After hybridization, the membranes were developed according to the manufacturer's instruction to yield luminescent signals, which were then captured on X-ray film (Hyperfilm ECL, (Amersham Pharmacia Biotech UK Ltd., Buckinghamshire, England) using Curix capacity plus film developer (AGFA Gevaert, Hamburg, Germany). The resulting image data were analyzed for differential gene expression patterns using GE Array Analyzer 1.2 (Super Array Bioscience Corp., Frederick, MD, USA) software. Loading was adjusted based on the intensity of hybridization signals relative to the housekeeping gene ß-actin.

3.5.4 Semiquantitative RT-PCR

To validate the results obtained by microarray analysis, we evaluated the expression of six transcripts by semiquantitative RT-PCR. Although this is only a semiquantitative measure of transcript abundance, the strong expression differences of the selected genes among the groups legitimize this approach. Select genes included IL-2, IL-7, IL-13, IFNα-2, IFNα-4, and IFNα-11. Total RNA was isolated from mice blood using the ZR Whole Blood Total RNA Kit (Zymo Research Corp., Orange, CA, USA). First strand cDNA was synthesized by the ImProm-II™ Reverse Transcription System (Promega Corporation, Madison, WI, USA) using oligo $(dT)_{12-18}$ primers according to the manufacturer's instruction. Afterwards, 4 µl cDNA product, together with the appropriate primers, was used as a template in PCR amplifications. The final products were electrophoresed in 2% agarose gel and detected by ethidium bromide staining. The expression levels of ß-actin were monitored as a loading control. The following primer sets (+, sense; -, antisense) derived from the respective Genebank sequences were employed: IL-2 (Accession No. NM_001530) IL-2 +: 5′- TCC TCA CAG TGA CCT CAA GTC C - 3′, IL-2 -: 5′- TGA CAG AAG GCT ATC CAT CTC C - 3′, IL-7 (Accession No. NM_008371) IL-7 +: 5′ - ATC CTT GTT CTG CTG CCT GT - 3′, IL-7 -: 5′ - CCA GTG TTT GTG TGC CTT GT - 3′, IL-13 (Accession No. NM_008355) IL-13 +: 5′- AGA CCA GAC TCC CCT GTG CA - 3′, IL-13 -: 5′ - TGG GTC CTG TAG ATG GCA TTG - 3′, INFα–2 (Accession No. K01238) INFα–2 +: 5′ - TGA GCT ACT GGT CAA TCT GTT CTC - 3′, INFα–2 –: 5′ - TTT GTC TCA CAC TCA CTC CTT CTC - 3′, INFα–4 (Accession No. NM_010504) INFα–4 +: 5′ - GCC TGT GTG ATG CAG GAA - 3′, INFα–4 –: 5′ - TGC CAG CAA GTT GGT TGA G - 3′, INFα–11 (Accession No. M68944) INFα–11 +: 5′- AAG GTC CTG GCA CAA ATG Ag - 3′, INFα–11 –: 5′ - CAT TCC AAG CAG CAG ATG AAG - 3′, ß-actin Accession No. M12481) ß-actin +: 5′ - TGT TAC CAA CTG GGA CGA CA - 3′ and ß-actin –:5′ - AGG AAG GCT GGA AAA GAG C - 3′.

3.6 Data analysis

Proliferation and cytotoxic assays are given as mean ± SD. All other data are given as mean ± SEM. Differences between the groups were assessed by a student's t test, with a p value < 0.05 considered significant.

4 Results

4.1 Mouse models of Lung Cancer

Two different cell lines (A549 and LLC1) were used in our studies to generate mouse models of lung cancer. A549 cells were derived from human lung adenocarcinoma, and LLC1 cells were derived from mouse lewis lung carcinoma (Fig. 2).

A mouse xenograft tumor model was generated by subcutaneous injection of A549 cells into immunodeficient mice (CD1 nude). Tumor growth was assessed for a period of five weeks. Tumor size increased with time and cell number dependent manner (Fig. 3A). A syngeneic graft tumor model was generated by subcutaneous injection of LLC1 cells into syngeneic C57/BL6 mice. Tumor growth was assessed for three weeks. Tumor size increased rapidly with time and cell number dependent manner (Fig. 3B).

A lung tumor model was generated by intratracheal instillation of murine primary LLC1 cells into C57/BL6 mice. Tumor formation was confirmed by computed tomography systems and by light microscopy using Hematoxylin and Eosin (H&E) stainings.

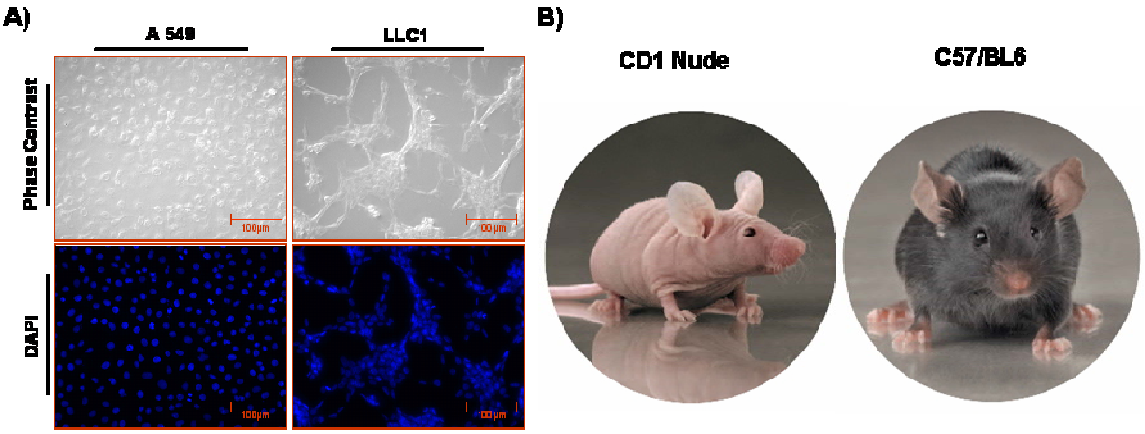

Figure 2: Cell morphology and mouse strains. (A) Adenocarcinoma (A549) and lewis lung carcinoma (LLC1) cell lines. Morphology was examined using phase contrast microscopy. The cells were counter stained with DAPI (Scale bar=100 µm). **(B)** CD1 nude and C57/BL6 mice strains were used for generating tumors.

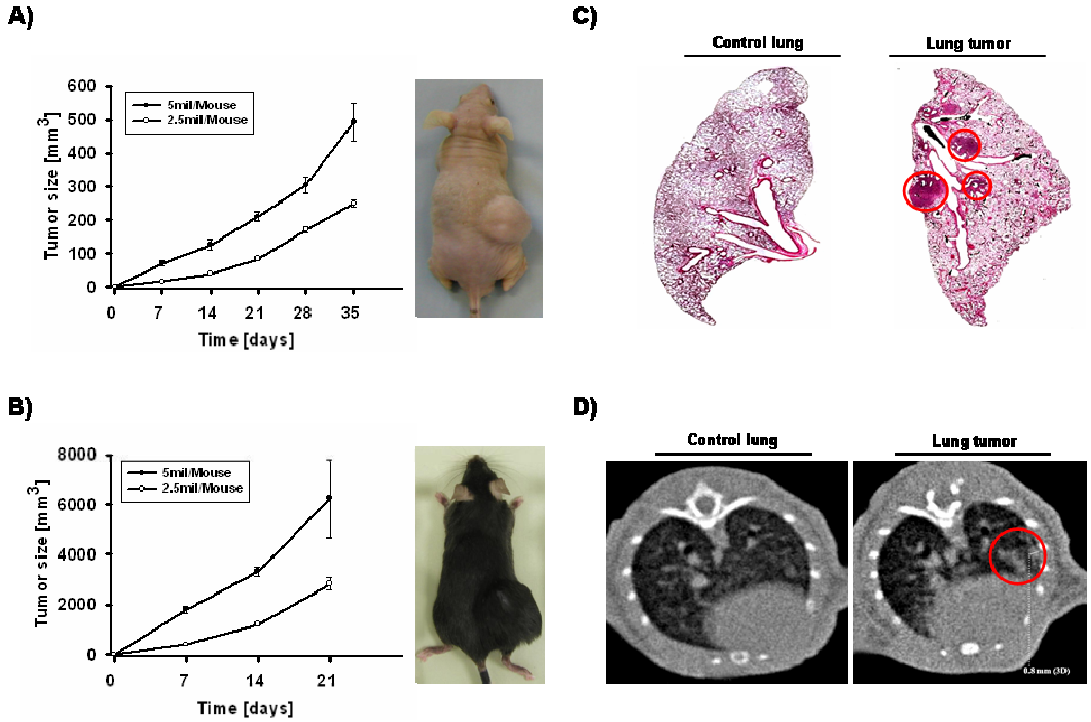

Figure 3: Subcutaneous tumors, lung tumor detection, and measurement. (A) A549 cells were injected subcutaneously into CD-1 nude mice. Tumor size was measured over 5 weeks by digital calipers in a time-dependent manner (mean ± SEM). **(B)** LLC1 cells were injected subcutaneously into C57/BL6 mice. Tumor size was measured over 3 weeks by digital calipers in a time-dependent manner (mean ± SEM). **(C, D)** LLC1 were cells instilled intratracheally into C57/BL6 mice. Derived lung tumors were detected with H&E staining and CT systems. Representative images from both control and tumor bearing mice are shown (**O** = Tumors).

4.2 Role of HIF-1α on tumor growth of lung adenocarcinomas

4.2.1 Characterization of cells transfected by HIF-1α

To analyze the effect of HIF-1, the human adenocarcinoma cancer A549 cell line was transfected with a human HIF-1α cDNA expression plasmid. HIF-1α overexpressing cells were selected with hygromycin. These cells were characterized by immunostaining for HIF-1α, hypoxia-responsive reporter gene assay, and HIF-1 dependent target gene VEGF expression (Fig. 4). The typical induction of HIF-1α, which was further enhanced in case of HIF-1α overexpression, was demonstrated in hypoxic conditions. Also, VEGF concentration in culture supernatants was enhanced under hypoxic conditions and when HIF-1α was overexpressed.

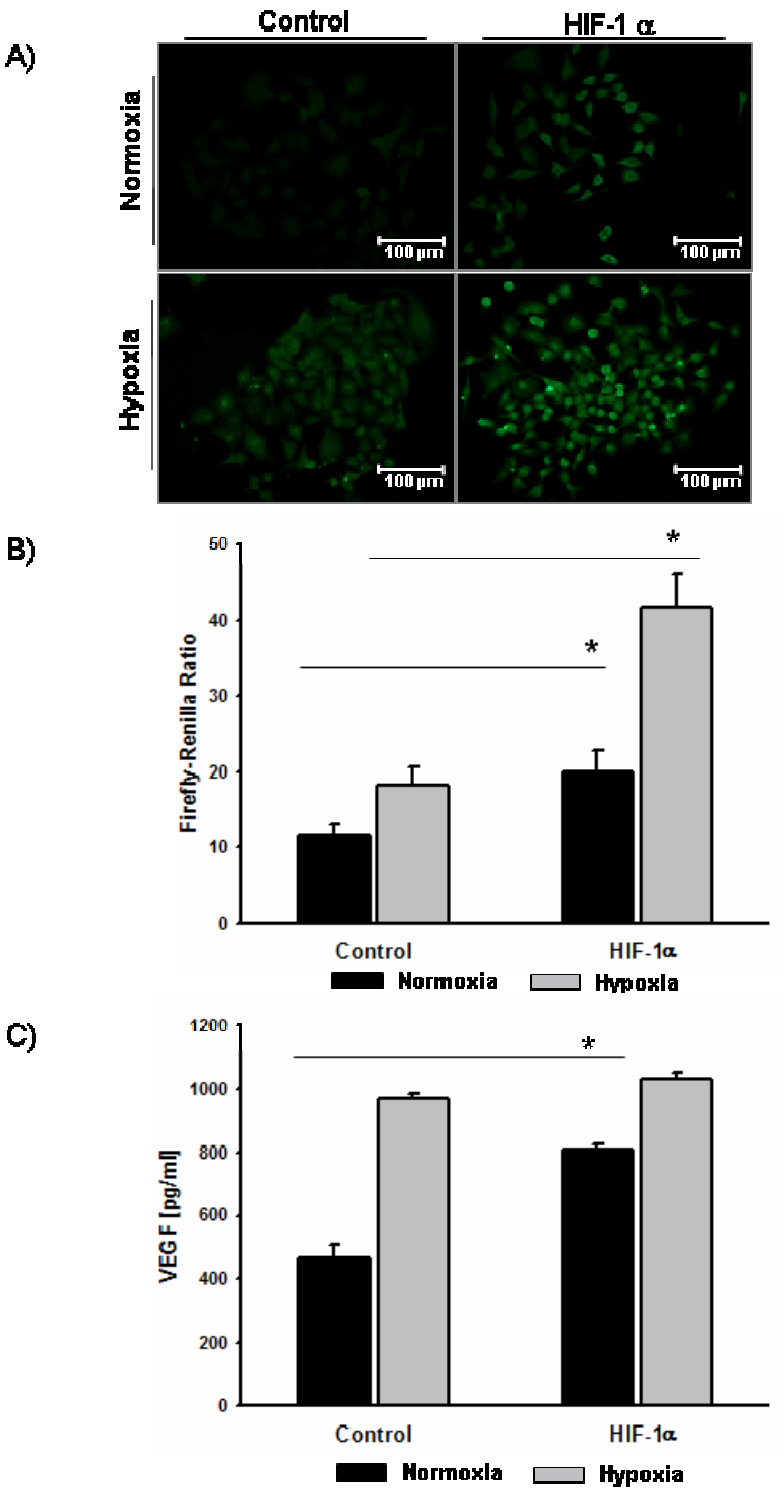

Figure 4: Characterization of HIF-1 expression in stable-transfected A549 cells. (A) Immunocytochemistry for HIF-1α in normoxic and hypoxic A549 cells stable-transfected with empty expression plasmid (control) or with an expression plasmid carrying the HIF-1α cDNA (HIF-1α). **(B)** Hypoxia-responsive-element (HRE) reporter gene assay of samples described in A (mean ± SEM, n = 3, *p<0.05, paired t-test). **(C)** HIF-1α target-gene vascular endothelial growth factor (VEGF) concentration measured in supernatants from the samples described in A (mean ± SEM, n = 3, *p<0.05, paired t-test).

4.2.2 Effect of HIF-1α on proliferation and apoptosis in cultured cells

To investigate the role of HIF-1α in cell survival and cell growth, the growth rates of HIF-1α overexpressing cells over a period of 8 days under normoxic and hypoxic conditions were measured (Fig. 5A). The growth rates decreased under hypoxic conditions in both control cells and HIF-1α transfected cells, reflecting a hypoxia induced growth arrest. However, HIF-1α transfected cells exhibited the lowest growth rates under both normoxic and hypoxic conditions. These data were confirmed measuring S-phase by thymidine incorporation (Fig. 5B). Control cells maintained under normoxic conditions exhibited the highest values, followed by control cells maintained under hypoxic conditions, while HIF-1α transfected cells again exhibited the lowest proliferations.

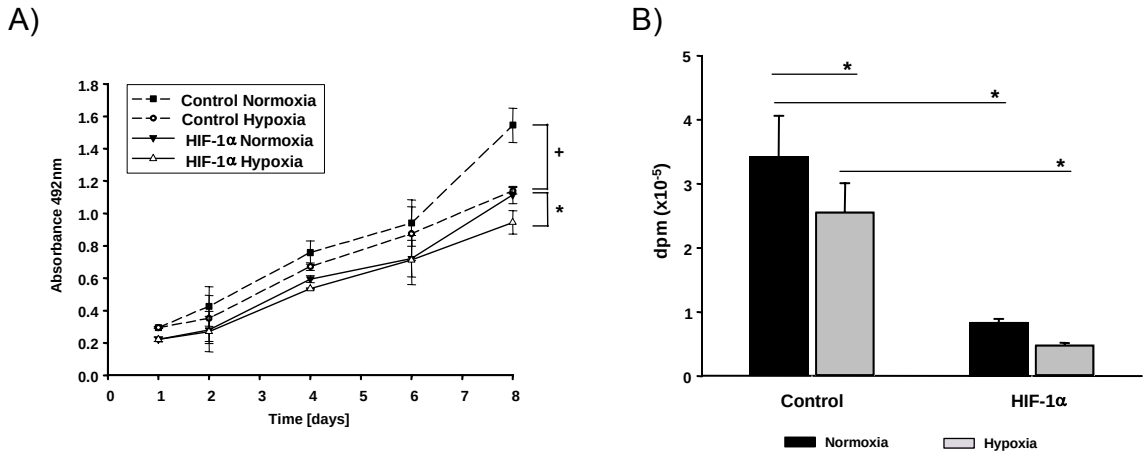

Figure 5: Analysis of cell proliferation in stable-transfected A549 cells. (A). Growth curve of A549 cells stable-transfected with empty expression plasmid (control) or an expression plasmid carrying the cDNA encoding HIF-1α (HIF-1α) measured by MTT assay under normoxic or hypoxic conditions (mean ± SEM, n = 3, $^{+}p<0.05$, comparison in normoxia; *p<0.05, comparison in hypoxia, paired t-test). **(B)** Thymidine incorporation after 24 h of hypoxic or normoxic exposure of cells stable-transfected with empty expression plasmid (control) or expression plasmid carrying HIF-1α (HIF-1α) (mean ± SEM, n = 3, *p<0.05, paired t-test).

We then analyzed cells grown in soft agar to address anchorage-independent growth as an in vitro measurement of tumorigenesis under long-term conditions. The HIF-1α transfected cells exhibited fewer colonies than did the control cells (Fig. 6A, B).

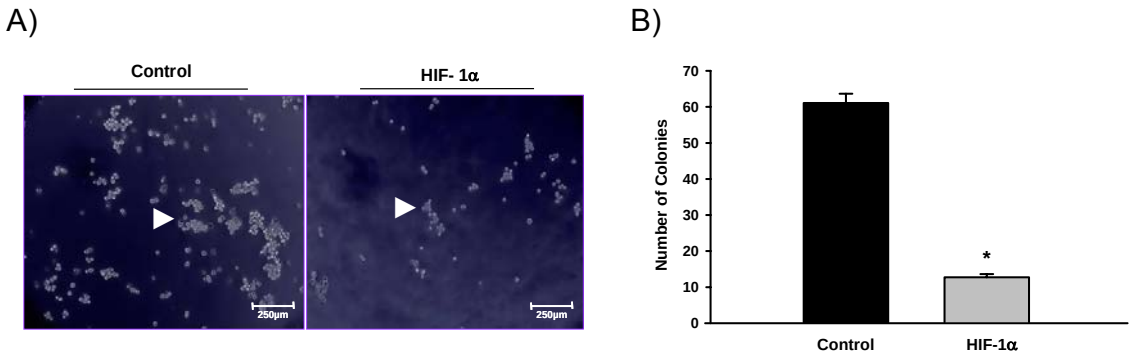

Figure 6: Soft agar cloning of stable-transfected A549 cells. A) A549 cells stable-transfected with empty expression plasmid (control) or expression plasmid carrying HIF-1α (HIF-1α) were cultured in soft agar to measure their potency of anchorage-independent growth. A representative figure from phase contrast microscopy is illustrated (▷ indicates a typical colony). B) Quantification of colony forming units (mean ± SEM, n = 24, *p<0.05, paired t-test).

The cultured cells were further analyzed cytochemically by TUNEL assay. We detected a greater increase in apoptosis under hypoxic versus normoxic conditions in both control cells and in HIF-1α overexpressing cells. Of the two groups, the HIF-1α overexpressing cells exhibited the greater increase in apoptosis, under both normoxic and hypoxic conditions (Fig. 7A, B).

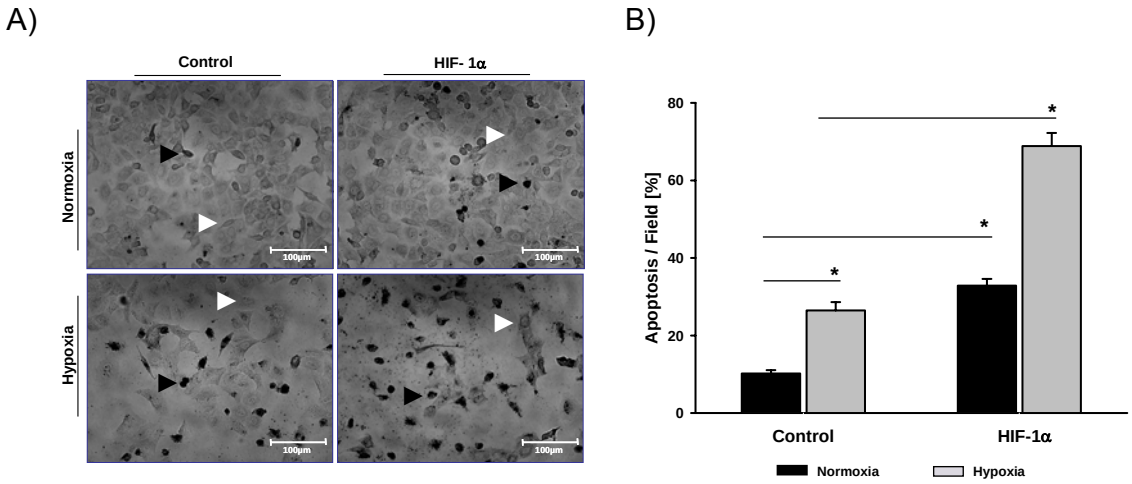

Fgure 7: Measurement of apoptosis in vitro. TUNEL assay in A549 cells stable-transfected with empty expression plasmid (control) or expression plasmid carrying HIF-1α (HIF-1α) cultured under normoxic or hypoxic conditions. **(A)** The TUNEL staining by cytochemistry in phase-contrast microscopy is illustrated (▷ indicates non-apoptotic cells, ▶ indicates apoptotic cells). **(B)** Quantification of apoptotic cells by counting microscopic fields (mean ± SEM, n = 15, *p<0.05, paired t-test).

4.2.3 Effect of HIF-1α on tumor growth in vivo

We further investigated the effect of HIF-1α overexpression on tumor growth in vivo. To this end, HIF-1α overexpressing cells were injected subcutaneously into nude mice. These mice developed tumors at the injection site. The size of tumor xenografts was measured over an eight-week period. The tumor xenografts derived from HIF-1α overexpressing cells were significantly smaller than those derived from control cells (Fig. 8A, B). To analyze the actual status of HIF-1α in these tumor xenografts, we analyzed RNA extracts of tumor tissues for HIF-1α mRNA and VEGF mRNA levels. We found increased levels of HIF-1α mRNA and VEGF mRNA; however, these levels were not significant for tumors derived from HIF-1α overexpressing cells (Fig. 8C, D).

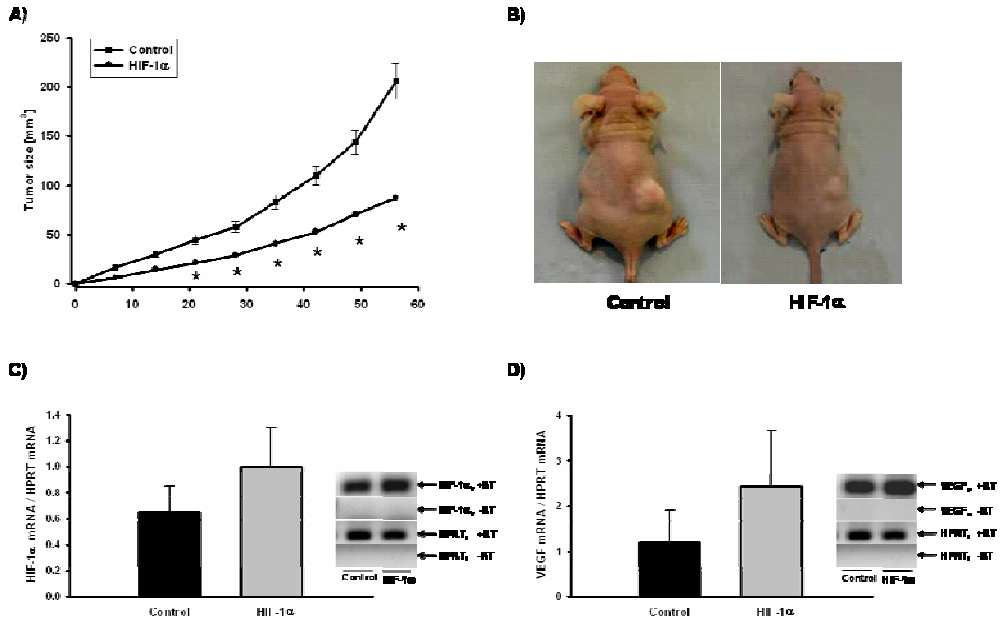

Figure 8: Tumor growth from cells stable-transfected with empty expression plasmid (control) or expression plasmid carrying HIF-1α ((HIF-1α)-transfected A549 cells). **(A)** Cells were injected subcutaneously into mice, and the tumor size was measured by digital calipers in a time-dependent manner (mean ± SEM, n = 12, *p<0.05, paired t-test). **(B)** Representative photograph of mice illustrating the development of subcutaneous tumors eight weeks after injection of cells into the hind flank. **(C, D)** Real-time RT-PCR analysis of HIF-1α mRNA and vascular endothelial growth factor (VEGF) mRNA (bottom) from RNA extracts of tumors derived from HIF-1α overexpressing or control cells. Data are normalized to the mRNA level of the housekeeping gene hypoxyphosphoribosyl transferase (HPRT). To demonstrate the integrity of the PCR products, an agarose gel of PCR fragments, stained with ethidium bromide, is included. The signals are only visible after reverse transcription (+RT), demonstrating that the signal is really derived from mRNA, while samples without reverse transcription (-RT), performed as a negative control, showed no signal.

4.2.4 Effect of HIF-1α on tumor vascularity and apoptosis

Hypoxia is a HIF-1 dependent stimulus for triggering angiogenesis, a process largely mediated by VEGF. We therefore analyzed vascularization of tumor xenografts derived from HIF-1α overexpressing or control cells by vessel staining the endothelial cell marker CD31 (Fig. 9A, B). Quantitative analysis performed by counting vessels in different tumor areas indicated a higher vascular density in tumors derived from HIF-1α overexpressing cells. Finally, tumor sections were also analyzed for apoptosis by TUNEL assay (Fig. 9C). The HIF-1α overexpressing tumors exhibited enhanced apoptotic rates in different sections investigated when compared to control tumors. Necrosis was observed in the central areas of both HIF-1α overexpressing and control tumors sections.

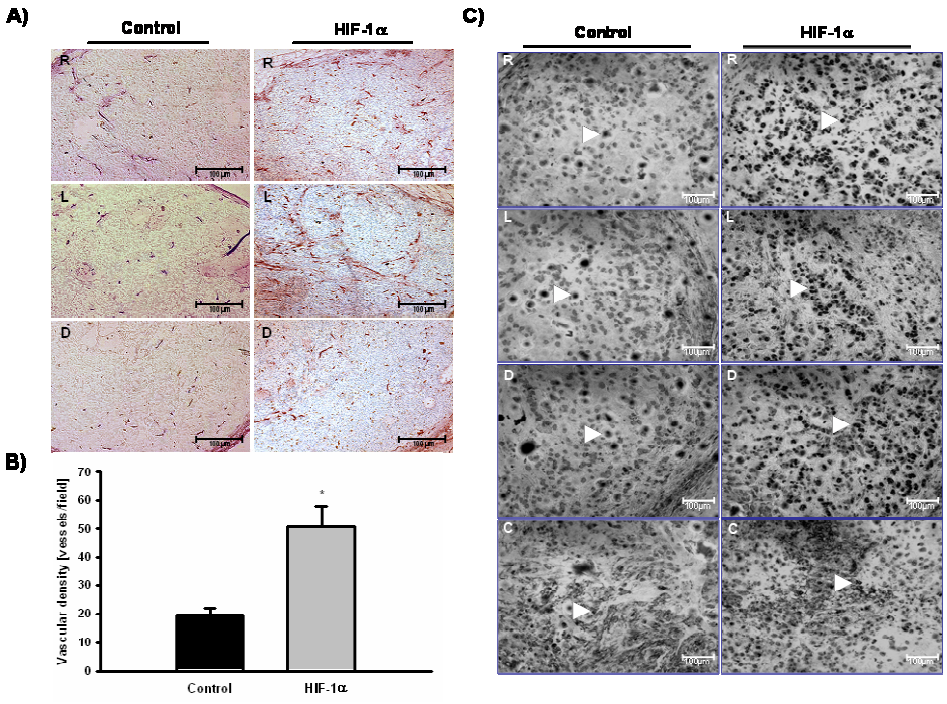

Figure 9: Quantification of vascular density and apoptosis: **(A)** Quantification of vascular density in various tumor sections (right part, R; left part, L; lower part, D) of HIF-1α overexpressing (HIF-1α) and control tumors (control). Shown is the immunohistochemistry of CD31 staining of frozen tumor sections. **(B)** The bar graph below shows quantification after counting representative fields from the microscopic images (mean, SEM, n =36, *<0.05, paired t-test). **(C)** Apoptosis in various tumor sections (right part, R; left part, L; lower part, D; central part, C) of HIF-1α overexpressing (HIF-1α) and control tumors (control) after eight weeks of cell injection. Tumors derived from HIF-1α overexpressing cells showed stronger apoptotic staining than control tumors (▷ labels apoptotic cell).

4.3 Anti-tumor effects of LLC1/DC fusion hybrids

4.3.1 Characterization of LLC1/DC cell hybrids

Activated DCs are potent inducers of T-lymphocyte-mediated immunity. To overcome the poor immune response particularly against weakly immunogenic tumor cells, we fused DC with LLC1 cells from C57/BL6 mice. Surface phenotypes of DCs and fused cells were analyzed by flow cytometry. LLC1 cells were stained with the green membrane marker PKH-67 (Fig. 10A). The characteristic phenotype and activation of bone marrow derived DCs was confirmed by expression of CD11c (Fig. 10B), B7.1 (Fig. 10C) and MHC class II (Fig. 10D) in about 60% of analyzed cells. Further, staining of both LLC1 marker and CD11c showed a few double positive cells in DC/LLC1 mixtures (Fig. 10E) in contrast to DC/LLC1 hybrids that showed about 50% of double positive cells (Fig. 10F). The fusion efficiency of DC/LLC1 hybrids was also confirmed by double staining with co-stimulatory molecules, B7.1 and MHC class II (Fig. 10G, H).

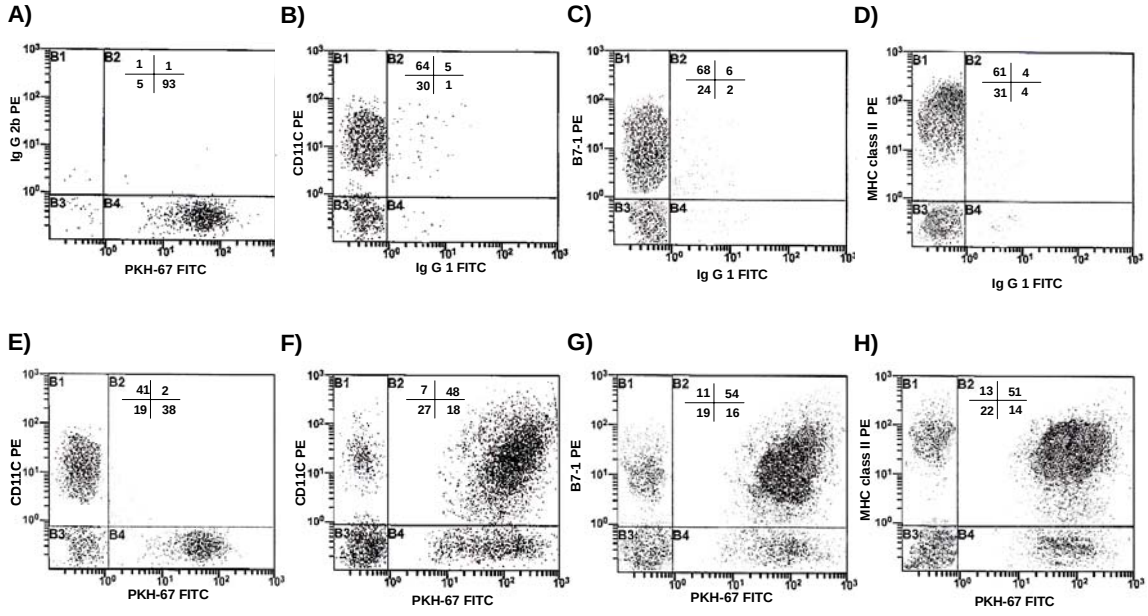

Figure 10: Fusion rate: (A) PKH-67 fluorescence on LLC1 cells. **(B)** Expression of CD11c, **(C)** expression of B 7.1, and **(D)** expression of MHC class II on dendritic cells. **(E)** CD11c and PKH-67 fluorescence on mixture of DC/LLC1. **(F)** Double staining of PKH-67 with CD11c or **(G)** B 7.1 or **(H)** MHC class II on fused Hybrids. Surface fluorescence intensity was evaluated by flow cytometry.

To evaluate the success of cell fusions, fluorescence microscopy was used to determine the quality of dual fluorescence on individual cells. PKH-67 and PKH-26, labeled

LLC1 and DCs, showed green or red staining of the cell membrane, respectively (Fig. 11A-D). HCs appeared yellow because of the double positivity for both membrane markers, PKH-67 and PKH-26 (Fig. 11E, F). As shown in Figure 11E, F, we also observed several green cells, indicating unfused LLC1 cells, and a few DCs and LLC1 cells with membrane overlapping. Moreover, on the second day following the fusion procedure, HCs showed a higher percentage of double positive cells and a strong yellow staining when compared to 1 day old HCs. Based on this observation, we assumed that fusion efficiency and proliferation of HCs increased with time.

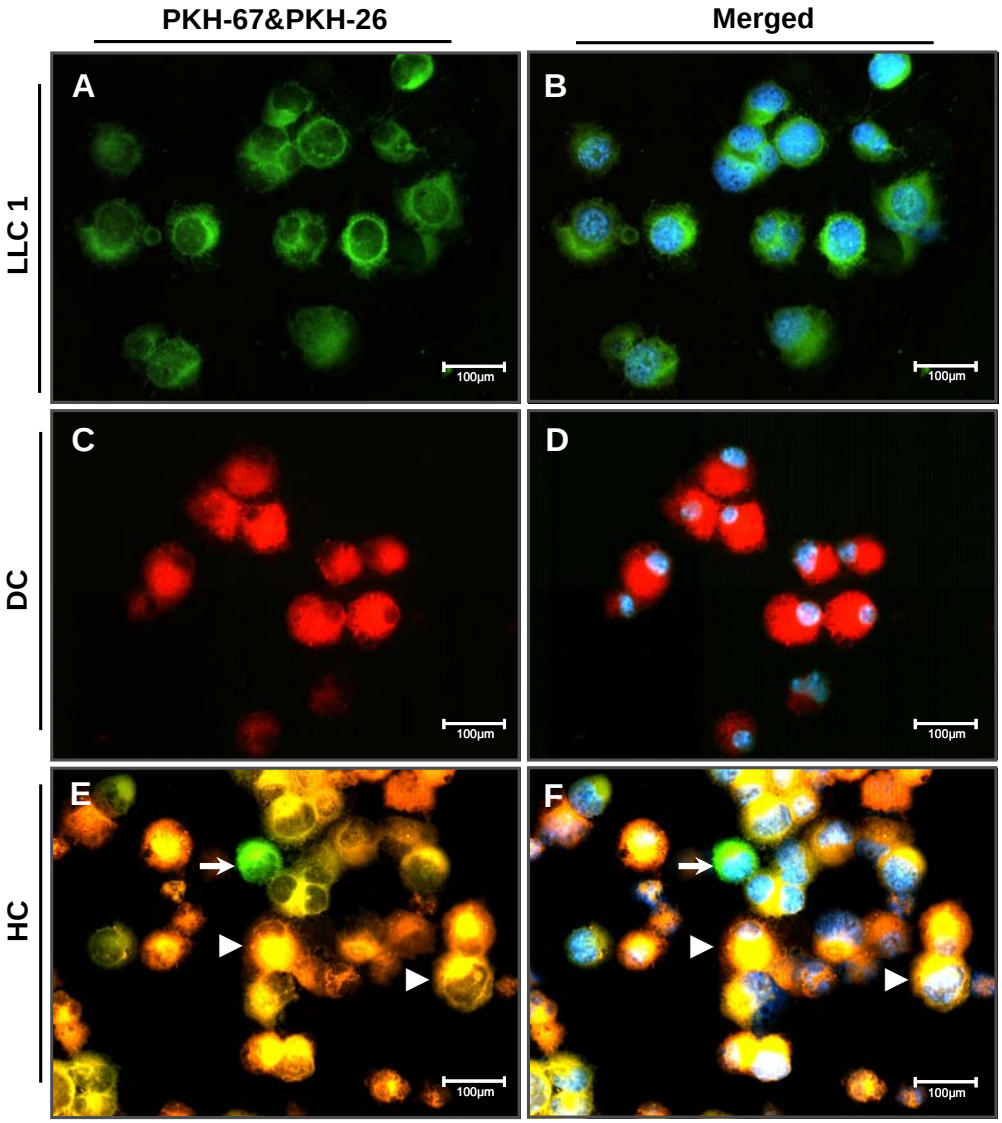

Figure 11: Fluorescence micrographs of LLC1, dendritic cells, and fusion hybrids. (A) PKH-67 labeled LLC1 cells, including (B) nuclei stain DAPI blue. (C) PKH- 26 labeled DCs, including (D) nuclei

stain DAPI blue. (E) Double stained HCs, including (F) nuclei stain DAPI blue. ► indicates HCs; → indicates unfused LLC1 cells. Scale bar: 100 µm.

4.3.2 Proliferation and cytotoxic response of hybrid immunized mice T-lymphocytes

Syngeneic naive mice were footpad immunized with irradiated LLC1, DCs, DC/LLC1, DC/LLC1 lysate, Hybrids or PBS alone as described in Material and Methods. After immunization, spleen (SC) and lymph node cells (LNC) from each group of mice were harvested and stimulated in vitro with syngeneic LLC1, DCs, DC/LLC1, DC/LLC1 lysate, HCs or allogeneic SC/LNCs (BALB/c derived) for 4 days. Only lymphocytes obtained from mice immunized with HCs showed a slight response to syngeneic naive tumor cells. T-cell response against tumor/DCs cell mixture or HCs was detected in all effector cell populations with the strongest response of lymphocytes obtained from mice immunized with HCs (Fig 12A).

To assess the induction of LLC1 specific cytotoxicity by HCs, spleen cells from each group of immunized mice were harvested and tested against LLC1 tumor cells, B16/F10 (2nd party tumor) cells or allogeneic lymphocytes. The results showed a negligible cytotoxic response of T-lymphocytes from mice immunized with DCs against LLC1 or B16/F10 tumor cells. In contrast, T-lymphocytes from mice immunized with HCs specifically targeted LLC1 tumor cells, but not B16/F10, a second party tumor cells (Fig. 12B).

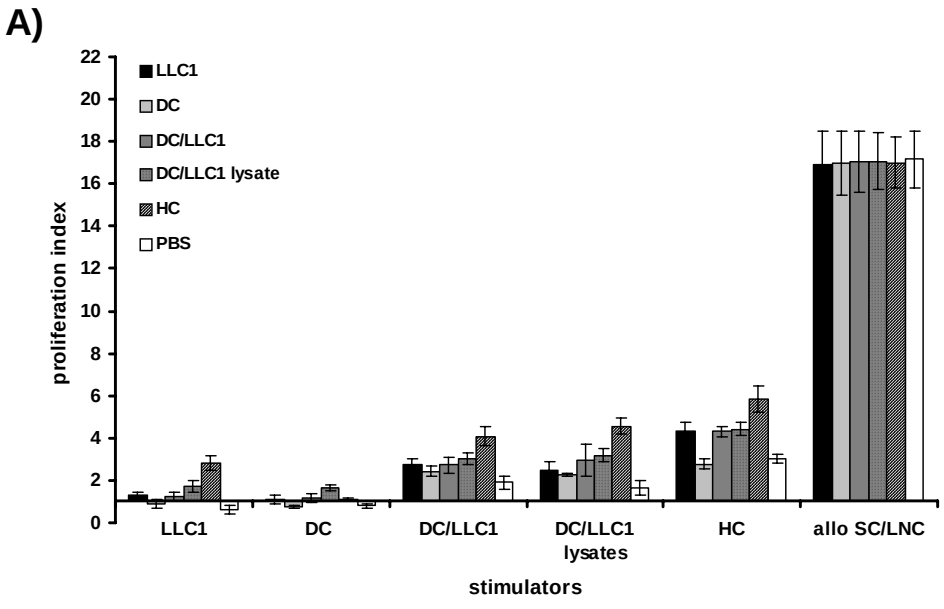

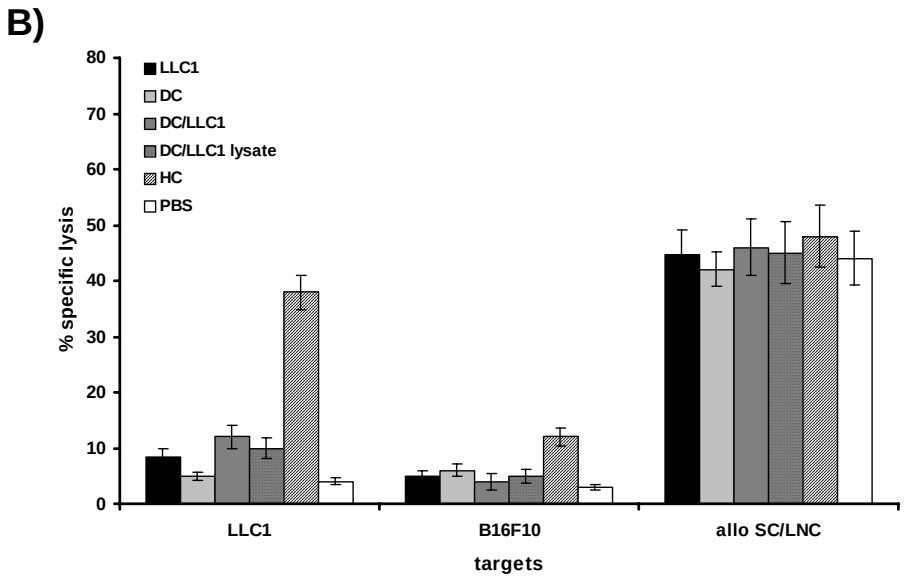

Figure 12: Proliferative activity and cytotoxicity of T-lymphocytes from immunized mice. (A) Proliferative activity of spleen cells (SC) and lymph node cells (LNC) collected from mice immunized with irradiated LLC1, DC, DC/LLC1, DC/LLC1 lysate, HC or PBS as control in response to different irradiated stimulator cells. SC/LNCs were either cultured with tumor cells LLC1, DC, DC/LLC1, DC/LLC1 lysate, HC or with allogeneic lymphocytes (BALB/c). Proliferative activity was determined by [3H] thymidine incorporation after 3 days of culture. Mean values + SD of the proliferation index (cpm of test well/cpm of control) of triplicate cultures are shown.
(B) Cytotoxic capacity of CTL spleen (SC) and lymph node cells (LNC) collected from mice immunized as described above were tested against LLC1 cells, syngeneic 2nd party tumor cells (B16F10) and allogeneic (BALB/c) lymphocytes at an effector:target ratio of 40:1. Mean percentages lysis values for four different experiments are shown.

4.3.3 Cytokine profile of hybrid immunized mice

To analyze LLC1/DC hybrid regulated cytokine genes, cellular RNA from LLC1, DCs, DC/LLC1, DC/LLC1 lysate, Hybrids or PBS immunized mice blood was isolated, reversed transcribed and hybridized with mouse common cytokine gene array. As shown in figure 13A, the expression of Interferon alpha family, gene B, 1, 2, 4, 5, 6, 7, 8, and 11, Interleukin 2, 7, 13 and also mouse stem cell factor (SCF), mast cell growth factor (MGF) kit ligand, and Tumor necrosis factor super-family member 13b were predominantly expressed in HCs immunized compared to all other control (LLC1, DCs and PBS) mice. These scores were normalized using the scores of ß-actin spotted on the same membrane.

To further verify the mouse cytokine gene array results, we performed semi-quantitative RT-PCR from HCs and control immunized mice. As shown in figure 13B

Interferon alpha family 2, 4, 7 and 11, Interleukin 2, 7, 13 were upregulated compared to all other control groups, confirming the micro array results.

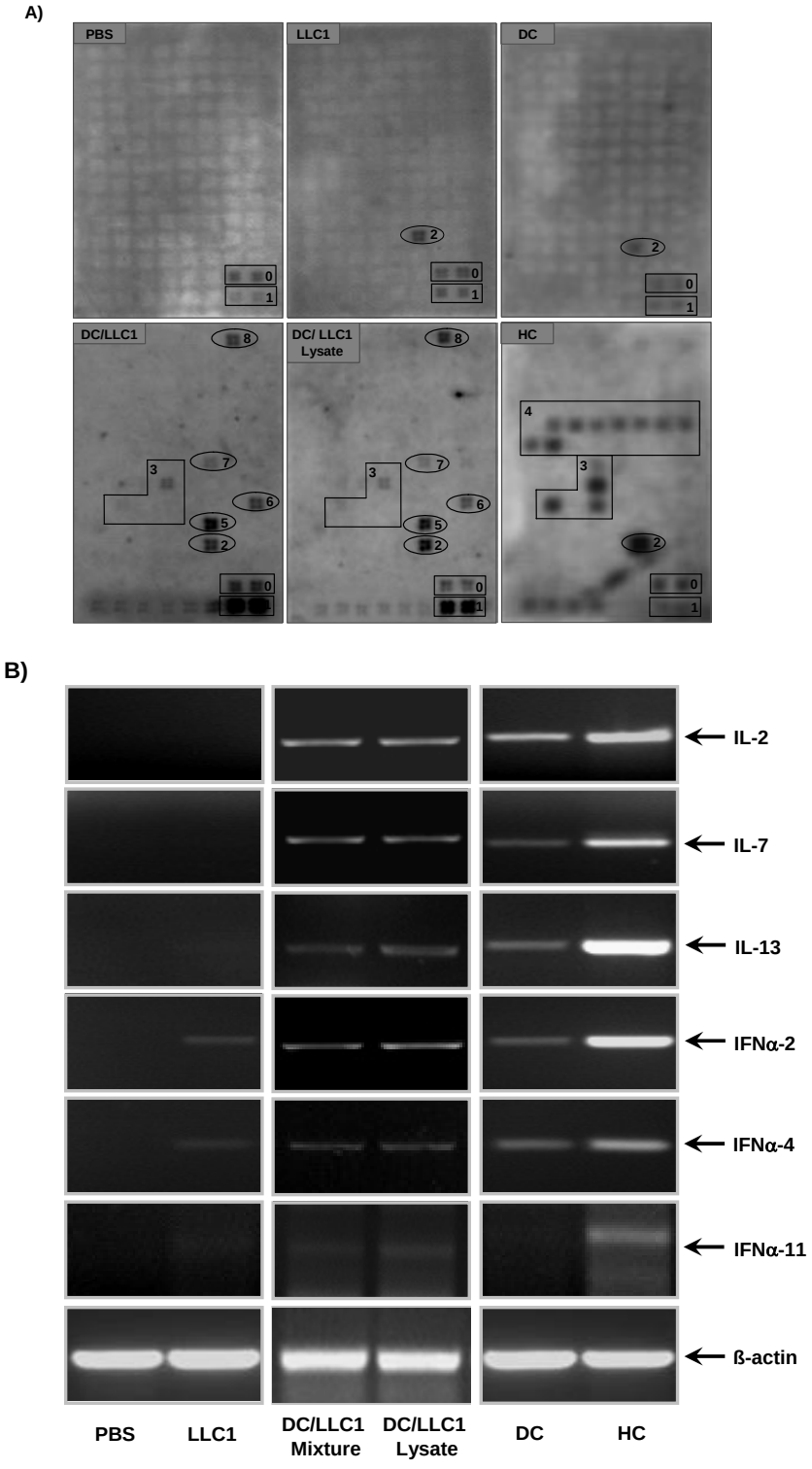

Figure 13: Representation of mouse common cytokine gene arrays from immunized mouse blood. **(A)** Mouse common cytokine gene arrays incubated with cDNA probes generated from immunized LLC1,

DC, DC/LLC1, DC/LLC1 lysate, HC or PBS alone. The detection of multiple cytokines by various samples was listed below.

1=ß actin, 2=Tumor necrosis factor super family member 13b, 3=Interleukin 2, 7, 13 and also mouse stem cell factor (SCF), mast cell growth factor (MGF) kit ligand, 4= Interferon alpha

family, gene B, 1, 2, 4, 5, 6, 7, 8, and 11, 5 = Transforming growth factor, beta 1 (Tgf b1), 6 = Lymphotoxin B (Ltb), 7 = Interleukin 16 (IL 16), 8 = Protein phosphate 1, catalytic subunit, alpha isoform (Ppp1ca).

(B) The mRNA level of each cytokine (IL-2, IL-7, IL-13, IFNα-2, IFNα-4 and IFNα-11) that exhibited significant regulation by HCs using cytokine gene arrays was analyzed by semi-quantitative reverse-transcriptase-PCR as described in "material and methods." The abundance of each cytokine mRNA is indicated relative to the ß-actin in immunized LLC1, DC, DC/LLC1, DC/LLC1 lysate, HC or PBS alone.

4.3.4 Immunization with hybrids induce growth retardation of LLC1 tumor challenge

To determine whether hybrid immunization affects tumor growth, groups of syngeneic naive mice were immunized twice and then challenged with tumor cells and monitored for tumor growth.

The results showed that mice immunized with LLC1 or PBS were all positive for tumor growth in the 1st week and 60% died within 28 days after challenge with LLC1 tumor (Fig.14A). Mice immunized with DCs or DC/LLC1 or DC/LLC1 lysate showed a slight decrease in tumor growth. However, mice immunized with HCs demonstrated a significant reduction (23%) in tumor growth and a delay in tumor development. These in vivo data were underlined by the in vitro evaluation of proliferation and cytotoxicity (Fig 14B, C). SC and LNC harvested from immunized and challenged animals 28 days after tumor challenge, showed a slight T-cell response after incubation with stimulator cells compared with results from animals that only received immunization. However, tumor challenge was not sufficient to trigger T-cell proliferation from animals immunized with LLC1, DCs, DC/LLC1 and DC/LLC1 lysate against naive tumor cells. In contrary, cytotoxicity assays with a specific lysis of 40% against naive LLC1 tumor cells induced by lymphocytes obtained from animals immunized with HCs. Otherwise, only T cells from DC, DC/LLC1 and DC/LLC1 lysate-immunized animals developed approximately 16% lysis activity as compared to 5% by unchallenged effector cells.

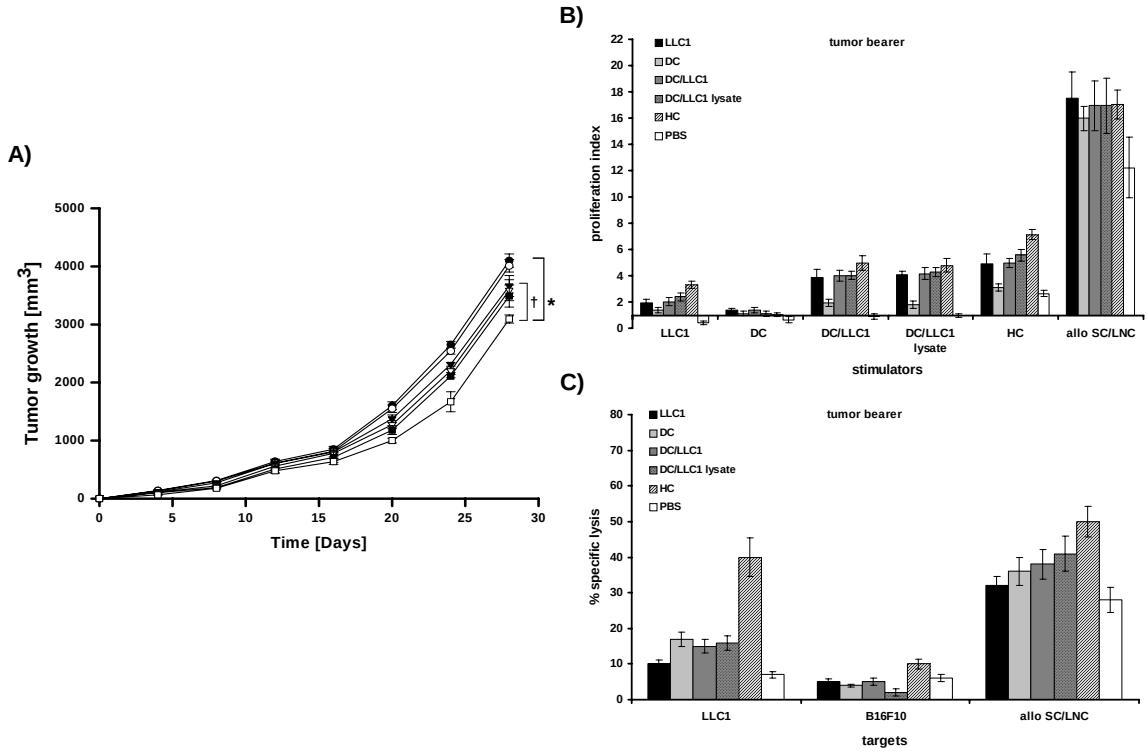

Figure 14: Anti-tumor effects of hybrid immunization. (A) Mice were immunized twice with PBS (□), irradiated LLC1 (O), DC (▼), DC/LLC1 ( ), DC/LLC1 lysate (■) or HC (□) and were challenged with LLC1 cells s.c after the 2nd immunization. Tumor volume measured chronologically after tumor challenge. Data are presented as the average tumor volume ± SEM of 10 mice. *, $p<0.05$ versus PBS and LLC1; †, $p<0.05$ versus DC

(B) Proliferative activity of SC/LNCs in response to different irradiated stimulator cells. SC/LNCs were collected from mice immunized with irradiated LLC1, DC, DC/LLC1, DC/LLC1 lysate, HC or PBS as control. SC/LNC was either cultured with tumor cells LLC1, DC, DC/LLC1, DC/LLC1 lysate, HC or with allogeneic lymphocytes (BALB/c). Proliferative activity was determined by thymidine incorporation after 3 days of culture. Mean values + SD of the proliferation index (cpm of test well/cpm of control) of triplicate cultures are shown.

(C) Cytotoxic capacity of SC/LNCs were tested against LLC1 cells, syngeneic 2nd party tumor cells and allogeneic lymphocytes at an effector:target ratio of 40:1. SC/LNC were collected as described above. Mean percentages lysis values from 4 different experiments.

4.3.5 Anti-tumor effect of hybrid vaccination

To examine the anti-tumor effects of HC vaccination on LLC1 subcutaneous tumors, LLC1 tumor inoculated mice were vaccinated with DC, DC/LLC1, DC/LLC1 lysate, Hybrids or PBS alone. As shown in Fig 15A, mice vaccinated with DCs as well as with mixture of DC/LLC1 or DC/LLC1 lysate, had no greater protection against LLC1

tumor challenge than the naive group (PBS alone), whereas in animals vaccinated with HCs, 60% growth reduction was achieved. Furthermore, the therapeutic effects of HC vaccination against LLC1 challenge was persistent and effective for longer periods (28 days). To determine whether vaccination can elicit T-lymphocyte proliferation and tumor specific cytotoxicity, T-lymphocytes from the vaccinated mice were exposed to stimulator cells or target tumor cells, respectively. As anticipated T-lymphocytes derived from HC vaccination showed increased proliferation indices against all stimulator cells and a 65% tumor specific cytolytic activity (Fig 15B, C) compared to T-lymphocytes derived from DC, DC/LLC1 and DC/LLC1 lysate vaccination.

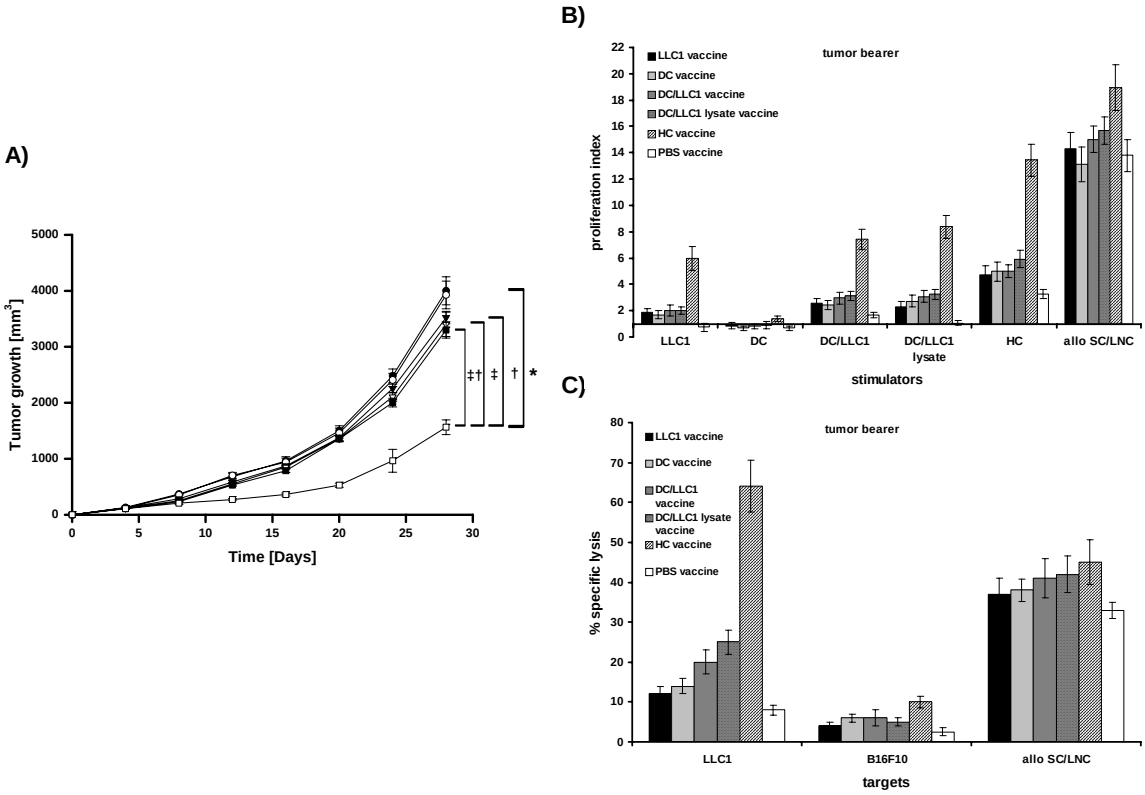

Figure 15: Lower tumor development by hybrid vaccination. (A) 7 days after tumor challenge of LLC1 cells, mice were vaccinated twice with PBS (□), irradiated LLC1 (O), DC (▼), DC/LLC1 ( ), DC/LLC1 lysate (■) or Hybrids (□). Tumor growth in each group of mice was recorded with 4-day interval of vaccination. Data are presented as the average tumor volume ± SEM of 10 mice. *, $p<0.05$ versus PBS and LLC1; †, $p<0.05$ versus DC; ‡, $p<0.05$ versus DC/LLC1 mixture, ‡†, $p<0.05$ versus DC/LLC1 lysate

(B) Proliferative activity of lymphocytes (SC/LNC) in response to different irradiated stimulator cells. SC/LNCs were collected from tumor bearing mice vaccinated twice with irradiated LLC1, DC, DC/LLC1, DC/LLC1 lysate, HC or PBS as control. SC/LNCs were either cultured with tumor cells LLC1, DC, DC/LLC1, DC/LLC1 lysate, HC or with allogeneic (BALB/c) lymphocytes. Proliferative activity was determined by [3H] thymidine incorporation after 3 days of culture. Mean values + SD of the proliferation index (cpm of test well/cpm of control) of triplicate cultures are shown.
(C) Cytotoxic capacity of lymphocytes (SC/LNC) were tested against LLC1 cells, syngeneic 2nd party tumor cells (B16F10) and allogeneic (BALB/c) lymphocytes at an effector:target ratio of 40:1. SC/LNC were collected as described above. Mean percentages lysis values for four different experiments are shown.

4.3.6 Adoptive therapy of established syngeneic tumors with hybrids primed T-cells

To assess the therapeutic potential of hybrid primed T-cells in established LLC1 tumors, we isolated SC/LNCs from DC, DC/LLC1, DC/LLC1 lysate, HC or PBS immunized C57BL/6 mice. These cells were adoptively transferred twice, with a 4 days interval, to LLC1 tumors bearing mice. In all the three treatment groups, visible tumor growth had started 4 days after tumor inoculation (Fig 16A). However, a dramatic reduction of tumor growth was observed 12 days after tumor implantation in mice treated with HC primed T cells (48%) compared with mice vaccinated with DCs (14%), DC/LLC1 (18%) or DC/LLC1 lysate (21%). Sustained growth retardation was observed at day 12 to day 28 with a mean reduction of 51.1%. In addition, we observed an increase in spleen size of mice treated with primed T-cells derived from mice vaccinated with HCs, thereby indicating an increased population of T-cells mediating tumor suppression (Fig 16B). These in vivo data were further supported by proliferation and cytotoxic assays. As shown in Fig 16C, D, T -lymphocytes harvested from the adoptively treated SC/LNCs HCs demonstrated an improved proliferation capacity against all stimulator cells, with a marked enhancement against hybrid stimulators. In line with these findings, LLC1 tumor specific CTL activity induced by the T -lymphocytes harvested from the adoptive treated SC/LNCs HCs was significantly elevated (50%) compared to all other groups including unchallenged effector cells.

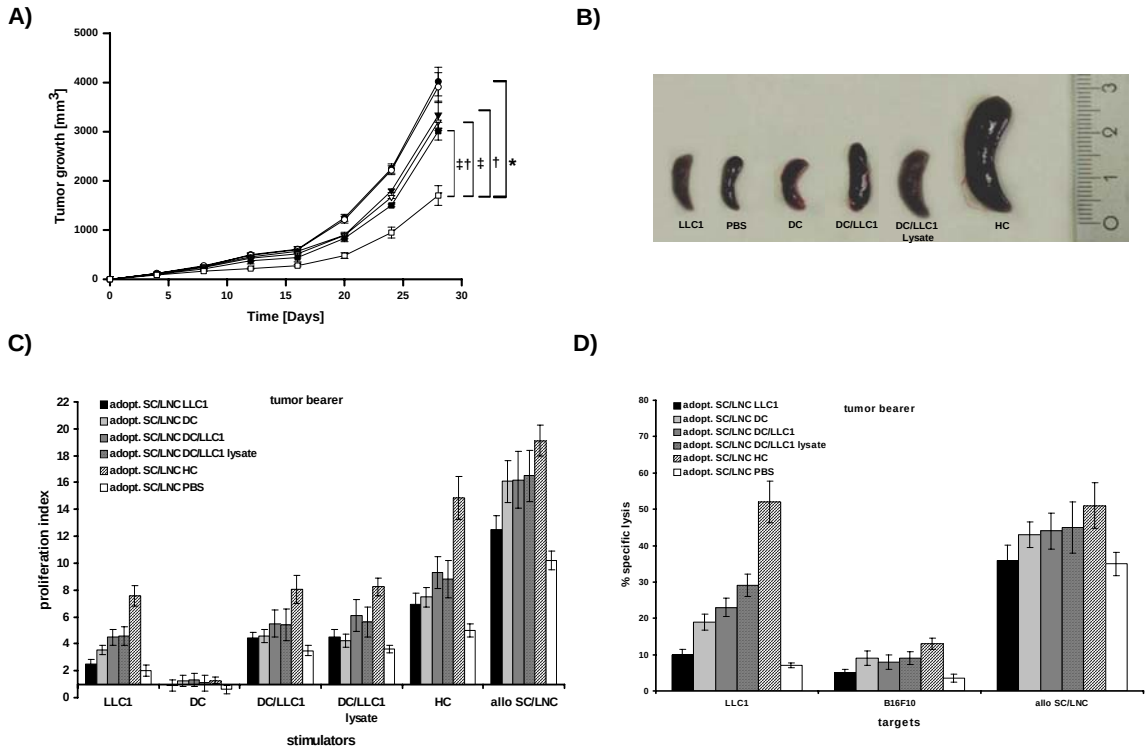

Figure 16: Suppression of LLC1 tumor growth in mice given adoptive immunotherapy (A) LLC1 tumors bearing mice were treated with SC/LNC cells isolated from PBS (□), irradiated LLC1 (O), DC (▼), DC/LLC1 ( ), DC/LLC1 lysate (■) or HC (□) immunized mice. Tumor development was monitored and recorded chronologically after tumor challenge. Data are presented as the average tumor volume ± SEM of 10 mice. *, $p<0.05$ versus PBS and LLC1; †, $p<0.05$ versus DC; ‡, $p<0.05$ versus DC/LLC1 mixture, ‡†, $p<0.05$ versus DC/LLC1 lysate

(B) Representative spleens, dissected 28 days after tumor challenge.

(C) Proliferative activity of SC/LNCs in response to different irradiated stimulator cells. SC/LNCs were collected from tumor bearing mice challenged with SC/LNC obtained from immunized mice. SC/LNCs were either cultured with tumor cells LLC1, DC, DC/LLC1, DC/LLC1lysate, HC or with allogeneic (BALB/c) lymphocytes. Proliferative activity was determined by thymidine incorporation after 3 days of culture. Mean values + SD of the proliferation index (cpm of test well/cpm of control) of triplicate cultures are shown.

(D) Cytotoxic capacity of SC/LNCs were tested against LLC1 cells, syngeneic 2nd party tumor cells and allogeneic lymphocytes at an effector:target ratio of 40:1. SC/LNC were collected as described above. Mean percentages lysis values from 4 different experiments.

4.4 Detection of pulmonary nodules in a lewis lung carcinoma model by fpvCT and MSCT

Scanning with both modalities (MSCT and fpvCT) could be performed without major motion artifacts; therefore, overall image quality was adequate for assessment of either scan. Comparing axial slices from both computed tomography systems; higher spatial and therefore anatomical resolution was obvious in fpvCT. Bronchial structures were clearly delineated and distinguished from pulmonary arteries, pulmonary veins, and lung parenchyma in this modality. The bronchial system and the whole lung could be tracked from its outlet for three-dimensional segmentation (Fig. 17). The four segments of the right lung could vaguely be distinguished in fpvCT, especially in the case of pleural effusions, while there was no differentiation possible with MSCT.

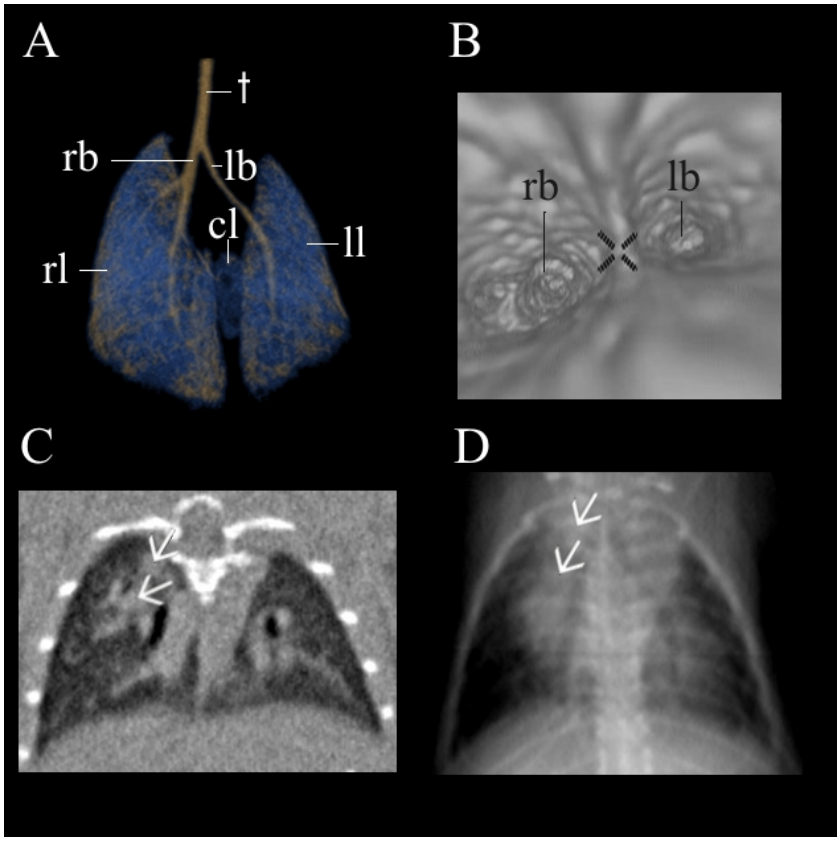

Figure 17: 3D segmentation of the lung. In panel **(A),** a 3D segmentation of the entire lung is shown. The trachea (t), left and right bronchus (lb, rb), and the division of the latter in its segmental bronchi are demonstrated. The left lung (ll) consists of only one segment, while the right lung (rl) has four segments where the cardiac lobe (cl) hands over to the right side. With the 3D software, virtual bronchoscopy can be performed. In panel **(B),** a view on the diversion of the trachea (cross) into the right bronchus (rb) and

left bronchus (lb) is indicated. Single reformatted slices (coronal view) can be combined to a 3D dataset, where, in this Maximum Intensity Projection **(C, D),** the tumor masses (arrows in C and D) are shown as enlargements of the mediastinum, known in its human correlate from chest imaging.

Pulmonary nodules were better delineated by fpvCT than by the clinical scanner. Detection of small nodules, which were frequently attached to pulmonary arteries, was improved in coronary reformatted images. Isotropic voxels were provided, and high resolution was obtained for both axial images and any reformatted slice (Fig. 18A, B). Therefore, better delineation and detection of tumors was possible in coronal planes, as the nodules could be distinguished from the pulmonary arteries, which were visualized in their course from their origin in the pulmonary artery to the periphery. The tumors showed preferential growth along the pulmonary arteries that was also better observed in coronal slices in fpvCT.

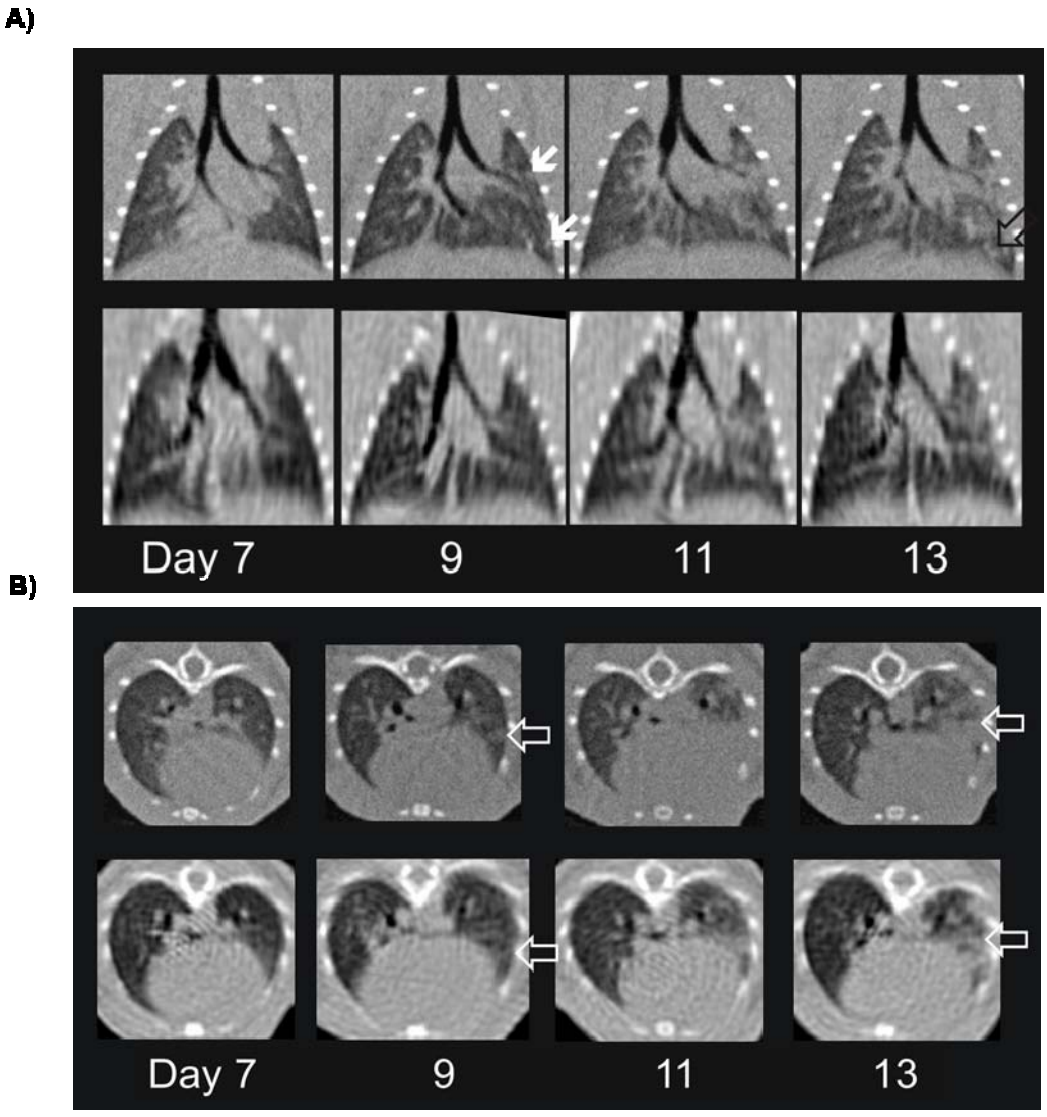

Figure 18: Display of coronal and axial reformatted images of datasets acquired with fpvCT and MSCT. (A) The first tumor nodules were detected with fpvCT on day 9 (white arrows); these nodules were not displayed in MSCT. Tumor induction was proven on day 11 in MSCT; however, the small nodules did not appear in later stages as in fpvCT (open arrow). The tumors were much better delineated in fpvCT images. The coronal reformatted images from MSCT appeared blurred due to anisotropy (less resolution in z-direction than in-plane). Isotropic voxels in fpvCT enabled more accurate volumetry of the nodules. **(B)** Axial slices acquired with fpvCT (upper row) and MSCT (lower row). The fpvCT images were of a higher quality and had less noise. Though the animal was freely breathing, the spine and ribs were much better delineated in fpvCT than in MSCT. The small nodule detected in fpvCT on day 9 was not visible in the corresponding image from MSCT (arrows). Due to the better resolution, the tumor border is more clearly delineated in fpvCT.

In Table 2, the time-point of lung nodule detection is stated in MSCT versus fpvCT, and the results on the last scan are opposed to investigation in histology. Tumor inoculation was successful in four mice (Mouse2 to Mouse5 in Table 2), visualized in longitudinal imaging, and proven in histology. Both imaging modalities revealed a good overall specificity of 100%. Comparing the scans on day 11 with the subsequently performed histology, MSCT scans created a sensitivity of 68% compared to 80% in fpvCT. Images taken before euthanasia of the animals could not be compared with ex-vivo investigation; therefore, a gold standard was not available. The only comparison possible was made by evaluating MSCT versus fpvCT, taking the later development of tumor evolution into account. A good validation was given with fpvCT, as all tumors detected in fpvCT could be followed in their growth and were evidenced in the final investigation with histology. Therefore, we could legitimately assume that positive evaluation of a nodule in fpvCT mirrored tumor growth. Relying on these assumptions, we found an overall sensitivity of 50% in MSCT compared to fpvCT.

		day 3	day 5	day 7	day 9	day 11	histology
Mouse 1	left						
	right						
Mouse 2	left			+	+	+	•
	right	+	+	+	+	⊕	•
Mouse 3	left						
	right			+	⊕	⊕	•
Mouse 4	left		+	⊕	⊕	⊕	•
	right				+		
Mouse 5	left				+	+	•
	right						•

Key: detected with
+ fpvCT
⊕ fpvCT and MSCT
• histology

Table 2: Lung tumor analysis. The results for the left and right lung of the five mice are tabulated for each day of investigation with fpvCT and MSCT, and finally for histology on the 11th day after tumor implantation. "+" means nodules were detected with fpCT but not MSCT, "⊕" indicates nodule detection with both fpvCT and MSCT, and presence of nodules found with histology is shown by "•". Except in mouse 4, all tumors were detected earlier in fpvCT. Sensitivity was superior in fpvCT compared to MSCT in the end-point of the investigation, while the specificity was 100% for both systems.

In addition to evidence of successful tumor inoculation, side effects from tumor growth, like pleural effusions and complications of intubation and tumor instillation, were detectable. Pulmonary infiltrates in the early course of the disease and pneumo-mediastinum and pneumothorax were observed.

Correlating the histological slices with images from fpvCT concerning the tumor diameter, we found a sensitivity of the system with 0.2 mm (Fig. 19A). However, shrinking artifacts may have appeared during histological preparation. Furthermore, volumetric measurements could easily be acquired with the three-dimensional datasets from fpvCT if there were good delineation from arteries and veins (Fig. 19B).

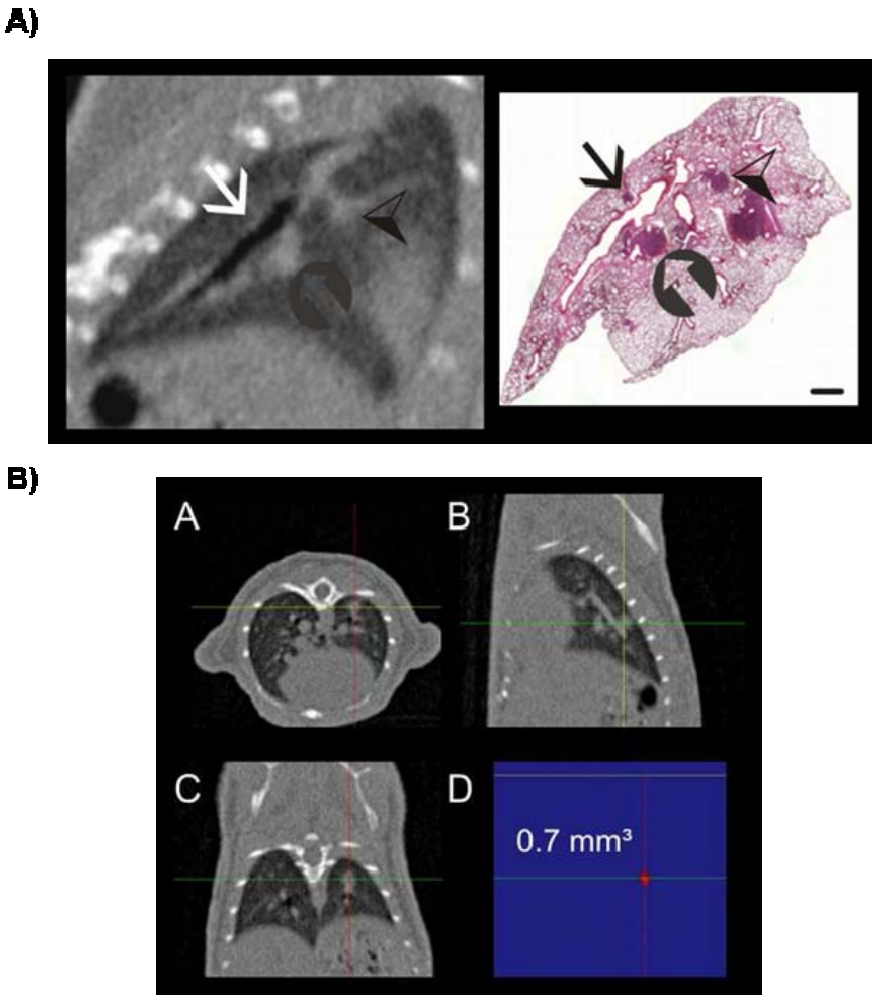

Figure 19: Comparison between fpvCT image and histology is displayed. (A) The small tumor adjacent to the bronchus (arrow) was measured with 200 µm in histology and vaguely seen in fpvCT. Therefore, 200 µm seems to be the cut-off resolution for lung nodules in fpvCT. Larger nodules could easily be identified in fpvCT (open arrow, arrow head). **(B)** In this panel, a three-dimensional reconstruction of a lung nodule is shown in fpvCT in the axial (A), sagittal (B), and coronal (C) planes. There is no obvious loss of resolution in the reformatted planes (B, C) as compared to the in-plane (axial, A) scanning slice. This nodule was measured with 0.7 mm³. A semi-automated threshold based algorithm was used for segmentation in the post-processing software.

4.5 Quantitative analysis of lung tumor vessel content by micro computed tomography

Both intrapulmonary and intravenous blood-pool CM injection kept the lungs fully inflated after extirpation and thereby enabled the detection of multiple lung tumors with µCT. These results closely corroborated the histological investigations (Fig. 20A, B). Quantitative volumetric measurements of extracted tumors and vascular fractions were made possible by this radiological modality (Fig. 21A, B).

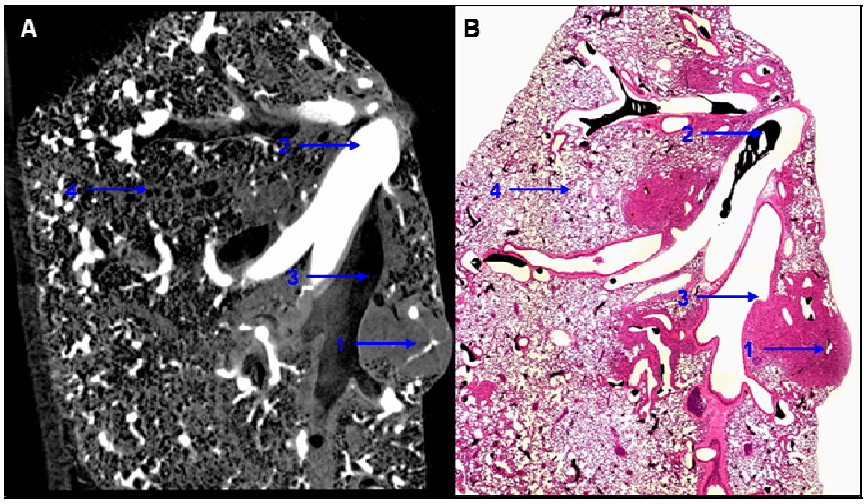

Figure 20: Comparison of µCT and microscopic images. (A) Transverse µCT image. **(B)** Conventional microscopic image of corresponding µCT section (magnification, 5X). Samples were scanned with µCT. The reconstructed images had isotropic voxels with 8 µm side-length. This section was subsequently stained with H&E for microscopic examination. Note tumor mass with contrast filled microvasculature (1), pulmonary artery (2), bronchus (3) and inflated lung (4).

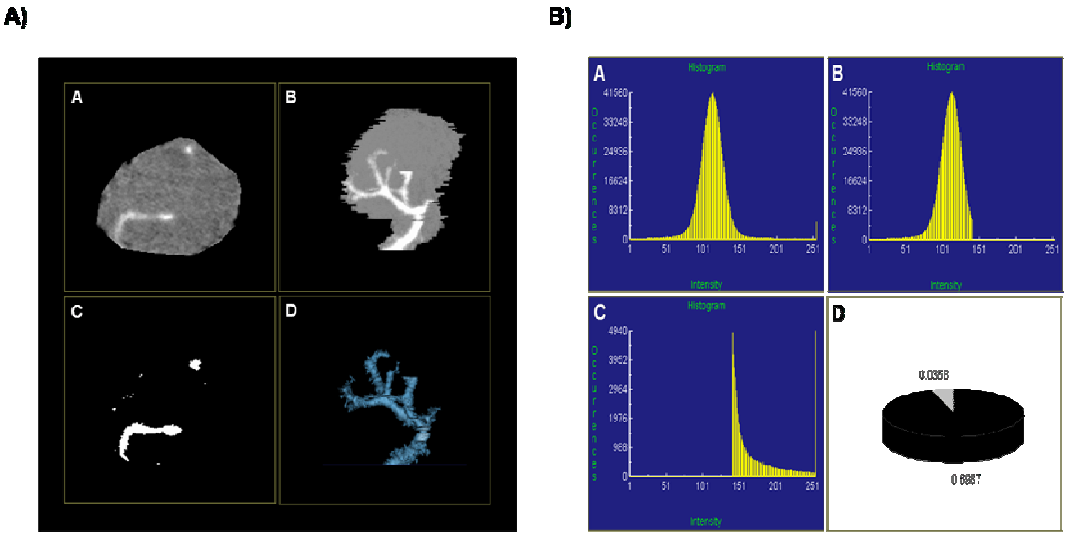

Figure 21: Quantitative volumetric measurements of extracted tumors and vascular fractions. (A) Single slice of the extracted tumors (A, B). Segmentation of the vascular fraction at the defined threshold (C) and in the entire extracted tumor by Volume Rendering Technique (D). **(B)** Volumetric histogram of the entire extracted tumor (A), the tumor without vessels (B), and the vessels of the tumor (C).Vascular fraction of the extracted tumor. Total tumor volume 0.7355 mm^3; ■ tumor volume without vessels (mm^3); □ vascular volume of the tumor (mm^3) (D).

4.6 Distribution of pulmonary and bronchial blood supply to lewis lung carcinomas

4.6.1 Tumor model

In H&E-stained histological images at 1, 3, 5, and 7 days following tumor instillation, tumors were noted at the peripheral parenchymal region away from the airways. The tumors increased in size from day 3 to day 7 (Fig. 22A), growing from 0.73±0.10 mm to 1.62±0.08 mm in diameter (Table 1). Additionally, in vivo images obtained with fpvCT before and after instillation of LLC1 cells in the same mice (Fig. 22B) detected rapid tumor development, with diameters increasing from 1.09±0.14 mm at day 3 to 1.93±0.10 mm at day 7, measured in reformatted images (Table 3).

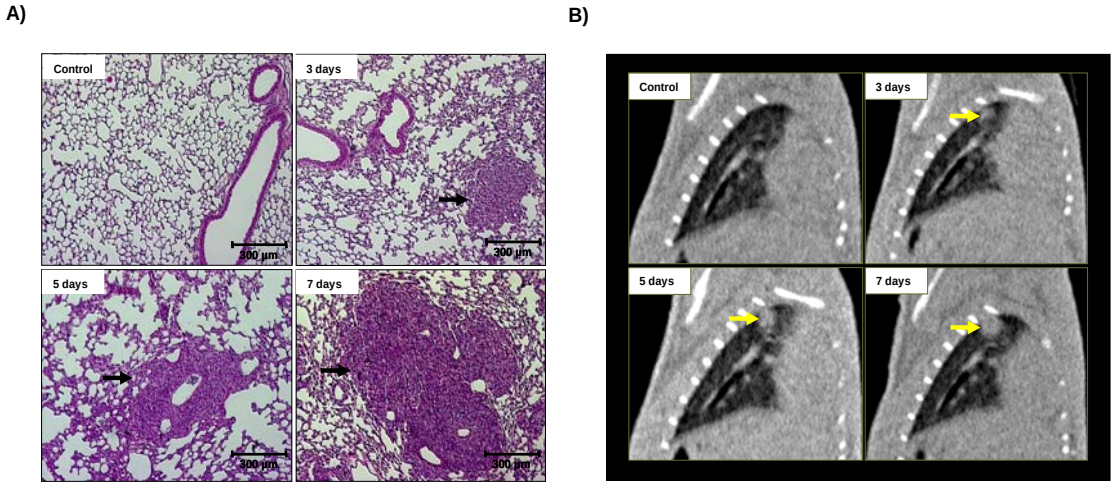

Figure 22: Analysis of lung tumor growth by histology and fpvCT. (A) Histological analysis with H&E staining of mice lung tumor tissue sections after intratracheal instillation of saline or LLC1 cells. The microphotographs demonstrate a time-dependent increase in tumor size, with an invasive growth (n=6 at each time point, bar = 300 µm); **Black arrow** indicates tumor. **(B)** Tumor detection with fpvCT in C57/BL6 mice in a longitudinal study, with scanning at days 3, 5, and 7 after LLC1-tumor instillation. Representative sagittal images from independent experiments (n=12). **Yellow arrow** indicates tumor

Tumor growth

Tumor	H&E staining (Diameter)	fpvCT (Diameter)
Control	no tumor	no tumor
3 days	0.73 ± 0.10 mm	1.09 ± 0.14 mm
5 days	1.13 ± 0.12 mm	1.47 ± 0.17 mm
7 days	1.62 ± 0.08 mm	1.93 ± 0.10 mm

Table 3: Measurement of tumor growth by histology and fpvCT. Measurement of tumor diameter obtained from H&E staining and fpvCT. H&E values represent the average diameter of typical tumors (n=6, at each time points). FpvCT values represent the average diameter over time of a specific tumor selected in each of 12 mice.

4.6.2 Fluorescent microspheres in LLC1 tumor lungs

Microscopic images of normal lungs revealed yellow microspheres originating from the pulmonary artery and spread throughout the parenchyma (Fig. 23C), as well as red microspheres, originating from the bronchial artery, close to the terminal bronchi and parenchyma (Fig. 23E, G). The parenchymal presence of microspheres from the bronchial artery might be explained by arterial anastomoses between the bronchial and pulmonary circulation and precapillary bronchial pulmonary connections of C57/BL6 mouse lung.

Furthermore, microscopic images of both normal and tumor lung cryosections revealed a predominance of yellow microspheres in both lung tissue and tumor tissue (Fig. 23C, D). In contrast, red microspheres were almost exclusively found in the lung tissue, with a predominant location adjacent to the bronchi (Fig. 23E, F). The absence of red microspheres in tumors indicated little or no perfusion of the tumor via systemic circulation. This observation was further confirmed in lung sections from mice that had microspheres introduced into both systems simultaneously (Fig. 23G, H).

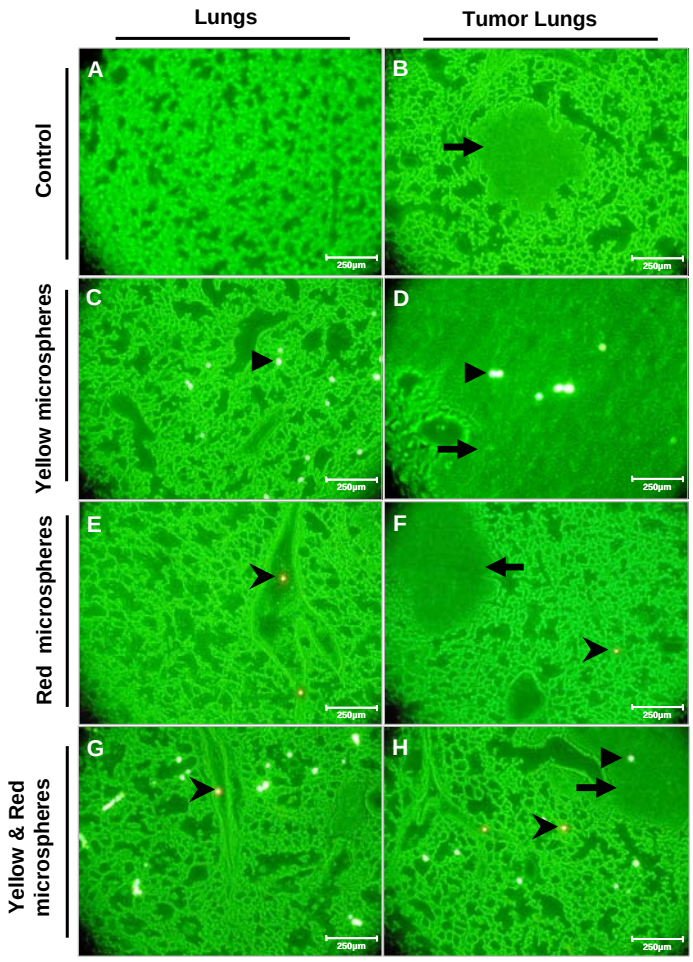

Figure 23: Blood vessel supply of healthy and tumor-bearing lung tissue analyzed by fluorescent microspheres. Cryosections of mouse lungs with **(B, D, F, H)** or without **(A, C, E, G)** tumors were analyzed with fluorescent microscopy for the presence of injected fluorescent microspheres. Lungs were fixed 7 days after LLC1 instillation when successful tumor induction was confirmed by fpvCT. The tumor lung sections show the presence of the solid tumor within the lung. Yellow fluorescent microspheres in control lung **(C)** and tumor lung **(D)**, injected into the pulmonary artery, show the localization of yellow microspheres in both lung and tumor **(D)**. Red fluorescent microspheres in control lung **(E)** and tumor lung **(H)**, introduced via the bronchial artery, resulted in detection around the bronchial branch **(E)** or parenchyma **(F)**. This observation was confirmed with simultaneous injection of both yellow and red fluorescent microspheres in control lung **(G)** and tumor lung **(H)** (n = 12). **Arrowhead** indicates yellow microspheres; **chevron** indicates red microspheres; **arrow** indicates tumor.

The microspheres lodged in lung and tumor preparations were counted under fluorescent microscopy (Table 4). The number of yellow microspheres (supplied by the pulmonary system) was 9117 (±113) per mg. of lung weight and 247 (±10) per mg of tumor weight, indicating that the tumor was less perfused than the healthy lung

parenchym (Table 4). The number of red microspheres (supplied by the bronchial system) was 713 (±58) per mg of lung weight and 4.5 (±1.9) per mg of tumor weight (Table 4). Furthermore, analysis of the relative vascular supply revealed an average ratio of pulmonary to systemic microspheres of 52:1 (± 0.0084) (tumor) and 13:1 (± 0.0069) (lung), a 4-fold greater ratio, confirming that the pulmonary arteries were the major feeding vessels to the tumor vasculature.

Mouse No	% tumor weight / lung weight	Yellow MS /mg lung	Yellow MS / mg tumor	Red MS /mg lung	Red MS / mg tumor
1	19.86	8794.33	223.21	567.37	0.36
2	10.61	8435.75	184.21	949.72	0.53
3	20.80	9127.52	266.13	1006.71	0.32
4	9.55	9554.14	208	700.64	17.33
5	17.16	9552.24	326.08	373.13	0.43
6	19.53	8698.22	208.18	769.23	10.30
7	13.90	8609.27	267.62	794.70	0.47
8	18.32	9465.65	260.42	381.68	5.83
9	9.09	9440.55	269.23	699.30	16.92
10	18.12	9395.97	259.26	805.37	0.37
11	23.22	9225.80	243.05	903.22	0.28
12	11.56	9115.64	257.05	612.24	0.58
Mean	**15.98**	**9117.93**	**247.70**	**713.61**	**4.48**
SEM	**1.39**	**113.41**	**10.84**	**58.63**	**1.92**

MS = Microspheres

Table 4: Analysis of pulmonary and systemic blood flow markers. Recovery of red and yellow fluorescent microspheres in the lung and lung tumors after injection of 1.5 x 10^5 red (left ventricle) or yellow (right ventricle) colored fluorescent microspheres (mean, SEM, n=12).

4.6.3 Analysis of micro computed tomography images

To identify the source of tumor vascularization, the lung vasculature was filled in three ways as described in materials and methods. Intravenous injection of contrast medium via the jugular vein resulted in complete fixation of the pulmonary vascular tree with preservation of both microarchitecture and three-dimensional interconnectivity. In

comparison, ex vivo administration of contrast medium via the pulmonary artery resulted in successful filling of the pulmonary arteries down to the capillary levels.

Both filling methods provided a clear visualization of the pulmonary artery branching to LLC1 lung tumors. The third filling approach, administration of contrast medium via the aorta, demonstrated both the origin of the bronchial artery at the level of main stem bronchi branching from the subclavian artery and the negligible role of bronchial arteries to LLC1 lung tumors.

For two or three dimensional presentations of intrapulmonary tumors and their vascularization, µCT images were reconstructed using 3D maximum intensity projection (MIP), 3D volume-rendering technique (VRT), and 2D multiplanar reconstruction (MPR). The 3D VRT µCT images (Fig. 24A, B) of contrast medium-filled lungs clearly showed branching and distribution of the pulmonary artery throughout the whole lung (Fig. 24A). The origin of the bronchial artery at the level of main stem bronchi branching from the subclavian artery was also visualized (Fig. 24B).

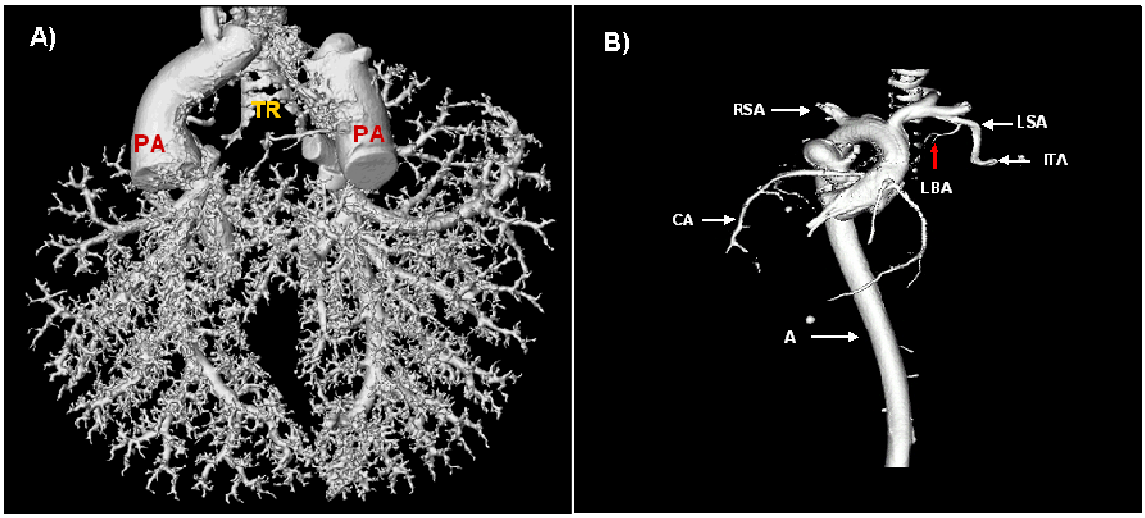

Figure 24: Volume rendering technique (VRT) images of the µCT. 3D VRT image of the contrast-fluid-filled pulmonary artery showed branching and distribution of the pulmonary artery (PA) throughout the whole lung. **(A)** 3D VRT image of the contrast-fluid-filled aorta showed systemic arteries **(B)** The main anatomical features, such as the origin, branches, and topography of the aorta (AO), including the left bronchial artery (LBA) branching from the left subclavian artery (LSA). In addition, the presence of right subclavian artery (RSA), internal thoracic artery (ITA), and coronary artery (CA) were also demonstrated (n=12).

3D MIP µCT image of contrast medium-filled lungs displayed fewer pulmonary vessels draining into tumors (Fig. 25A). In addition, coronal 2D MPR serial images of the tumor lungs showed the entry and branching of the pulmonary artery in the LLC1 tumor mass (Fig. 25B). This was demonstrated more clearly on the magnification MIP image view (Fig. 25C). All vascular filling approaches displayed branching of small pulmonary vessels inside the tumors without bronchial arterial branching.

These observations obtained from µCT scanning, along with the results obtained with fluorescent microspheres, confirmed that the pulmonary artery was the predominant tumor blood supplier.

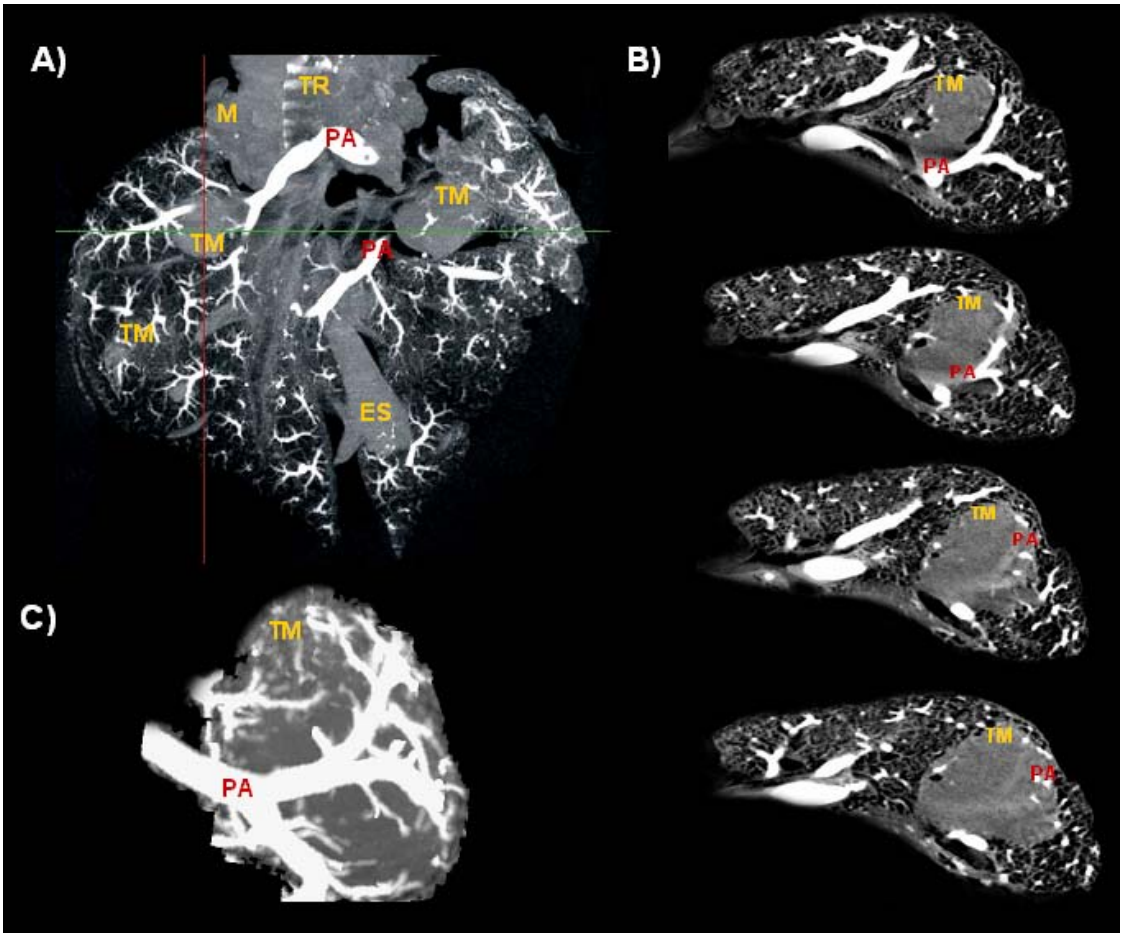

Figure 25: Maximum intensity projection (MIP) and multiplanar reconstructions (MPR) images of the µCT. 3D MIP image of the contrast-fluid-filled pulmonary artery shows branching and distribution of the pulmonary artery (PA) through the tumor mass (TM). In addition, the main anatomical features, such as trachea (TR), mediastinum (M), and esophagus (ES), are also visible **(A)**. Coronal 2D MPR images of the tumor lung shows the pulmonary artery (PA) passing through the LLC1 lung tumor mass

(TM) **(B)**. Magnification of 3D MIP image shows the increase of pulmonary artery (PA) vessel density around the tumor mass (TM) and vessels infiltrating the tumor **(C)** (n=12).

4.6.4 Repetitive analysis of fpvCT images in living mice

Non-invasive high resolution fpvCT was employed to obtain detailed characterization of lewis lung carcinoma mice model in vivo. The scanning revealed that lung tumors were closely attached to the pulmonary artery. Small tissue bridges suggested tumor nutrition from branches of the attached vessels (Fig. 26A, B, C, D). Both pulmonary arteries and veins were connected to the tumor by such bridges. This observation confirmed primary nutrition of the tumor from pulmonary circulation. The fpvCT permitted tumor detection down to a size of about 0.1 mm.

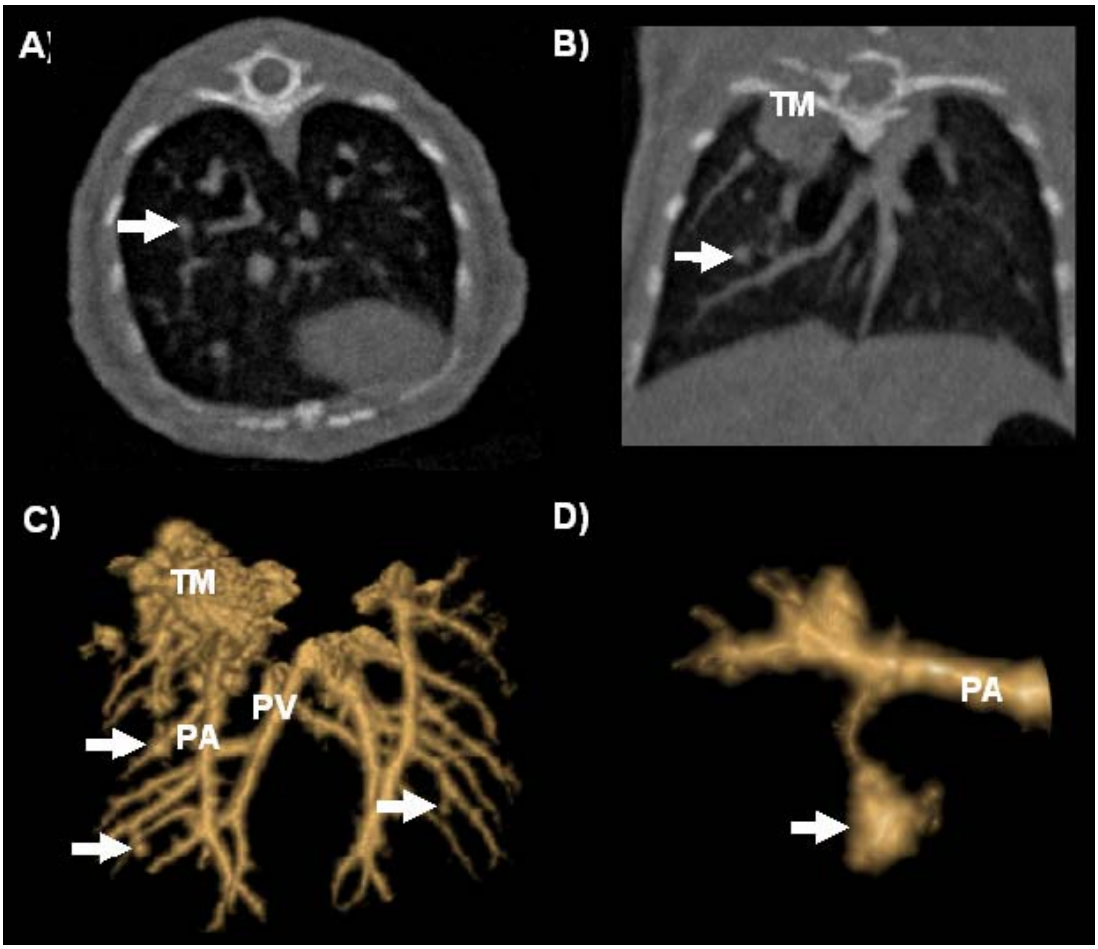

Figure 26: In vivo volumetric computed tomography (fpvCT) scanning of LLC1 lung tumors. Documentation of a lung nodule (0.5 mm in diameters, arrow) in axial **(A)** and coronal **(B)** projections, imaged with fpvCT. The voxel size was 0.05 mm in an isotropic dataset. Therefore, three-dimensional

visualization was readily available. Panel **(C)** displays a surface rendering of the pulmonary arteries (PA) and pulmonary veins (PV) with the adjacent nodules (arrow), as well as a large tumor mass (TM) in the apical lobe of the right lung. Panel (**D)** a magnification of the nodule displayed in the reformatted slices (A, B) shows the bridge structure from tumor to the adjacent pulmonary artery (n=12). Arrow indicates lung nodule.

5. Discussion

5.1 Therapeutic strategies

5.1.1 HIF-1α overexpression in lung adenocarcinoma mouse model

In the present study, overexpression of HIF-1α in adenocarcinoma A549 cells resulted in reduced proliferation and increased apoptosis. In line with this data, subcutaneous tumors derived from HIF-1α overexpressing A549 cells revealed decreased tumor growth and increased apoptosis, though the vascularization in these tumors was enhanced. These data reflect the fact that HIF-1α acts as a negative regulator of tumor growth in the lung adenocarcinoma model, despite a concomitant increase in vascularization, confirmed by both in vitro and in vivo studies.

Reduced proliferation and increased apoptosis observed in HIF-1α overexpressing A549 cells correlated with preceding studies illustrating that hypoxic conditions induce HIF-1α dependent growth arrest and apoptosis in embryonic stem cells (Carmeliet *et al.,* 1998), mouse embryonic fibroblasts (Schmaltz *et al.,* 1998), and lymphocytes (Goda *et al.,* 2003).

Likewise, tumor growth retardation by HIF-1α overexpression in adenocarcinoma mouse model was also in line with a reciprocal study (Carmeliet *et al.,* 1998) that analyzed a tumor model derived from embryonic stem cells with inactivated HIF-1α. These tumors exhibited accelerated growth despite decreased vascularization. In an additional study analyzing HIF-1α and HIF-2α expression in breast cancer cell lines, a surprising inverse correlation between low HIF-1α and HIF-2α and cells surviving under hypoxic conditions was observed (Blancher *et al.,* 2000). Interestingly, these cell lines exhibited high basal levels of VEGF, which in turn stimulated angiogenesis and supported tumor growth (Ryan *et al.,* 1997; Maxwell *et al.,* 1997; Elson *et al.,* 2001).

We believe that apoptosis induction by HIF-1α in our adenocarcinoma model could be mediated either by increased stability of p53 or by suppression of Bcl2 family member NIP3 (Bruick *et al.,* 2000; Ravi *et al.,* 2000). In addition, the expression level of p53 could negatively influence HIF-1α stabilization by interacting with HIF-1α ubiquitination, thereby linking a primarily apoptotic factor to angiogenesis (Bruick *et al.,* 2000). Because HIF-1α can be regulated by molecules such as growth factors

(Fukuda *et al.,* 2002), oncogenes (Laughner *et al.,* 2001), and tumor suppressor genes (Bruick *et al.,* 2000; Jiang *et al.,* 2003; Zimmer *et al.,* 2004), its cellular context determines its role in a specific tumor model. This phenomenon might also explain the ambiguity observed in clinical studies linking HIF-1α expression with patient survival.

Several clinical studies, including studies involving ovarian tumors, lymph node-negative and lymph node-positive breast carcinomas, have suggested that HIF-1α overexpression is independently correlated with poor patient prognosis (Birner *et al.,* 2001, 2002; Schindl *et al.,* 2002). Similarly, two other studies examining cervical and oropharyngeal cancers also indicated that HIF-1α was an independent marker for poor outcome (Aebersold *et al.,* 2001; Burri *et al.,* 2003).

However, in one study, lung cancer patients with high HIF-1α expressing tumors showed longer median survival times. This study demonstrated a role for HIF-1α in apoptotic induction (Volm *et al.,* 2000). An additional study, performed on patients with head and neck cancers, revealed decreased tumor growth in high HIF-1α expressing tumors (Beasley *et al.,* 2002). These observations are comparable with the experimental model described in this study and suggest that overexpression of HIF-1α acts as a negative regulator of tumor growth in lung adenocarcinomas.

5.1.2 Therapy with hybrid primed lymphocytes and hybrid vaccination

Fusion of C57/BL6 mice bone-marrow-derived DCs with LLC1 cells resulted in around 50% efficiency. Immunization with fusion cells activated proliferating and cytotoxic T-cells and significantly retarded tumor growth; this was also confirmed by upregulated expression of distinct cytokine genes. The same observations were supported by vaccination with fused cells in the tumor-bearing host. Finally, when T-cells from fused-cell-vaccinated mice were transferred into naive tumor-bearing mice (adoptive cellular therapy), tumor growth was greatly retarded, and an efficient proliferative and cytotoxic T-cell response was observed. Tumor growth was reduced by over 50%, and tumor development was significantly delayed, suggesting an effective immunotherapy against poorly immunogenic carcinomas.

We established stable hybrid cells by fusing DC with autologous LLC1 cells from C57/BL6 mice, as fused tumor and APC cells are believed to more efficiently induce

a host T-cell mediated anti-tumor response. The underlying principle of this approach is the generation of single cells that encompass the antigen presentation ability of the parental LLC1 cell (Gong *et al.,* 1997; Kawada *et al.,* 2003). Accordingly, hybrid cells generated in the present study demonstrated the full functional potency of DCs, along with the co-expression of separately prestained membrane markers (PKH-67 and PKH- 26), as evidence for efficient single cell fusion.

Lymphocytes obtained from mice immunized with hybrids showed a slight proliferative response to syngeneic naive tumor cells in vitro, as well as cytotoxicity against LLC1 cells, without any evidence of cross-reactivity against B16/F10 tumor cells. Furthermore, the analysis of anti-tumor effects mediated by hybrids in protective immunization, vaccination, and adoptive therapy proved promising.

In the group of mice that received immunization as a protective strategy, only hybrid-immunization induced partial host productivity against LLC1 tumor challenge. These data were in line with the enhanced proliferative and cytotoxic response of T-lymphocytes derived from mice that received HCs and tumor cells against naive LLC1 tumor cells in vitro, as compared to animals that only received immunization.

Furthermore, HC vaccination resulted in long-lasting tumor growth retardation, compared to the minimal effects of DC vaccination or HC immunization. This might have been due to the vaccination's ability to capture tumor antigens and effectively present these TAA to unprimed and/or host APC-primed T-cells in vivo. This behavior corroborated with the vaccination-elicited activities that were CTL specific against LLC1 tumor cells (Yang S. *et al.,* 1997).

Most impressively, hybrids were also remarkably effective in the adoptive LLC1 tumor therapy model. Adoptive transfer of HC primed T-cells was therapeutically effective against established tumors. The magnitude of tumor retardation was almost equal to the effects of vaccination with HC. In addition, increased cytotoxicity against naive LLC1 tumor cells by T-cells harvested from mice that had received adoptive treatment was observed. This finding was supported by the increased spleen sizes, indicating an increased population of T-lymphocytes responsible for tumor suppression.

In addition, we demonstrated that the hybrid mediated cytotoxic responses were mainly based on CD8+ lymphocytes, although CD4+ T-cells and NK cells also appeared to be factors. NK cell activation mediated by hybrid cells was more likely

the result of an intermediate interaction of DCs with CD4+ T-cells, rather than a direct effect of DCs on NK cells. CD4+ T-cells acted as links between DCs and NK cells, possibly through the induction of host DCs, producing IL-15 via interaction of CD40 ligand on the T-cell and CD40 on the DC (Ge *et al.,* 2002). In conclusion, these findings suggest that hybrid vaccination or adoptive transfer of hybrid-primed lymphocytes elicits anti-tumor immunity against tumors that are not highly immunogenic.

5.2 Tumor imaging modalities

5.2.1 Micro computed tomography (µCT)

Our results suggest that µCT is a reliable and non-destructive method for volumetric quantification of intrapulmonary tumors in the mouse model. Unlike histomorphometric procedures, µCT permits complete quantification of the vascular parameters.

µCT also allows us to visualize the architecture of tumor vasculature and, most importantly, to derive quantitative information from these images. The method allows the entire lung tumor to be studied intact, without physically sectioning or otherwise disrupting the tissue. However, µCT is restricted to ex vivo investigation of lung tumors for optimal visualization of the vasculature. Previous studies that have involved µCT imaging of the vasculature have used either barium sulphate-based contrast agents (Langheinrich *et al.,* 2004) or polymerizing compounds containing lead chromate (Holdsworth *et al.,* 2002). We found the polymerizing agent silicon-based microfil (lead chromate based) to be far superior for the intrapulmonary tumor model; however, we consider both agents useful, depending upon the mode of application. In this study, the silicon polymer was ideal for imaging intrapulmonary tumors because it allowed us to circumvent problems such as settling and lack of homogeneity within the vasculature, clumping during injection, and difficulty with perfusion due to high viscosity. In addition, silicon polymer allowed us to differentiate pulmonary vascular tree from pulmonary arteries, thereby facilitating the delineation of tumor vascular origin.

Furthermore, the adjustments that exist when defining the binarization threshold and the scanning resolution are important methodological aspects that must be considered

when using μCT imaging for analysis of tumor vasculature. The most important parameter is how to determine binarization thresholds in the μCT system. Luo *et al.* (1999) studied the relation between binarization thresholds and detectability of several structures. However, an uncertainty that varies according to the type of specimen does exist. As recommended by previous reports (Bentley *et al.,* 2002), the optimal binarization threshold for each specimen was determined in this study. A value, based on the threshold that captured the complex architecture of tumor microvasculature with minimal overestimation of broader structures, was chosen.

Likewise, the voxel size of the scan was also selected to image smaller vascular structures. For example, a voxel size of 8 μm was shown in our study to be appropriate for measuring a minimum vessel diameter of 9 μm, much smaller than any obtained by previous μCT images (Maehara *et al.,* 2003). However, drawbacks, including increased scan time and computational time, as well as more complex analyses, did exist.

In our study, μCT was used for volumetric quantification of a tumor and its vascular structures, but only structures delineated with sufficient contrast material could be visualized and quantified. By using tomographic reconstruction algorithms (Volume rendering technique), images of the vessels in the lung tumors that allowed total stereoscopic visualization of the three-dimensional microarchitecture of the lung tumors were generated. Since tomography allows convenient extraction of appropriate sections from the three-dimensional images, μCT also can be used to analyze and quantify distinct regions of interest more accurately; i.e., we were able to measure intrapulmonary tumors and their total vascular content.

In conclusion, the current study demonstrates that μCT imaging using perfused contrast agents provides a robust methodology for evaluation of vascular networks. Specifically, μCT is advantageous because it provides high resolution, quantitative, 3D, and objective data analysis. This was evident in our validation study using histological images, which found μCT to offer a highly accurate, less variable and less time-consuming alternative for quantitative measure of intrapulmonary tumors and its vascular content in the LLC1 mouse model. μCT techniques also offer flexibility to the user in defining the volume of interest (VOI) to be evaluated. Thus, contrast-enhanced μCT imaging provides broad applicability to tumor model systems

that require a vigorous and highly quantitative evaluation of vascular structure or growth.

5.2.2 Flat panel volumetric computed tomography (fpvCT)

The fpvCT proved its superior sensitivity in the detection of lung nodules. The accuracy in volumetry of nodules down to 0.2 mm in diameter was shown in histology. FpvCT, a new high resolution imaging system, proved its abilities in monitoring a lung tumor model, proving the importance of follow-up investigations in cancer research.

Few reports about follow-up studies of lung disease in mice can be found in medical literature (Kennel *et al.,* 2000; Ford *et al.,* 2003; Schuster *et al.,* 2004; Kiessling *et al.,* 2004; Plathow *et al.,* 2004). Although there is a rising need for diagnostic procedures to investigate tumor models, the lung is difficult to assess with conventional imaging techniques (Mitzner *et al.,* 2001; Schuster *et al.,* 2004). A limiting factor is the susceptibility of the systems to motion artefacts. The most promising modality is computed tomography, offering short scanning times and satisfactory tissue resolution in the lung due to the high contrast between air and alveolar tissue. Short scanning time permits investigations in a short ventilation arrest after intubation of the animals. However, this is a very invasive procedure, putting the life of the animals at risk in repeated scanning, especially in the investigation of models with pulmonary disease. To avoid this situation, we attempted to investigate the animals that were breathing freely. As a consequence of deep anesthesia and a muscle relaxing substance, thoracic movement was reduced to a minimum. In fpvCT as well as in MSCT, no major motion artefacts impeding image evaluation were observed, though slight blurring of the diaphragm indicated residual movement.

FpvCT showed a significant increase in sensitivity to small lung nodules compared to MSCT. Therefore, it is important to integrate fpvCT into cancer research in small animals to give preclinical research important information on their models. Benefits include (i) information about successful tumor induction, (ii) quantification of tumor growth, (iii) observation of possible complications (pneumonia, atelectasis), and most importantly, (iiii) success of therapeutic approaches.

Beyond monitoring of lung nodules, fpvCT could be used to detect and characterize structural lung pathologies like emphysema or fibrosis. The option to evaluate

functional parameters like tumor perfusion, previously reported for other modalities in subcutaneous tumors (Kiessling *et al.,* 2003*;* Krix *et al.,* 2003), has been exercised. The feasibility of morphological imaging of angiogenesis with fpvCT has been demonstrated (Kiessling *et al.,* 2004). Visualization of the vessels inside lung tumors is much more challenging, due to the thoracic motion and the small size of the tumors, although assistance of indirect parameters of angiogenesis in an orthotopic tumor model with perfusion imaging were available (Kerbel *et al.,* 2004).

In combination with other functional imaging modalities, fpvCT would help quantify and localize tumors. Used in combination with planar modalities like optical imaging (Mahmood *et al.,* 1999; Bremer *et al.,* 2003; Ntziachristos *et al.,* 2003; Yang *et al.,* 2003) or tomographic modalities with less resolution, like PET and SPECT (Weissleder *et al.,* 1998; Budinger *et al.,* 1999; Bremer *et al.,* 2002; Lewis *et al.,* 2002; Kiessling *et al.,* 2004), fpvCT could provide helpful additional information.

5.3 Applications

5.3.1 Delineation of vascular supply of lung tumors

This study describes blood flow distribution to lung tumors in an experimental C57/BL6 mouse model with intra-tracheal instillation of LLC1 cells. Using fluorescent microspheres infusions, subsequent microscopic analysis, and 3D images obtained by μCT and fpvCT, we identified the pulmonary artery as the major source of blood supply to the tumor vasculature in this model of primary lung cancer.

Based on previous observations in nude mice, where the diameter of the capillaries was measured as 4-9 μm (Lehr *et al.,* 1993; Bernard *et al.,* 1996), we decided to use 10 μm microspheres with different fluorescent colors. Our data revealed an average ratio of microspheres originating from the pulmonary to systemic systems as 13:1 (lung) and 52:1 (tumor). These data supported the known fact that pulmonary arteries are the major feeding vessels of the lung parenchyma. The predominance of the pulmonary over systemic blood supply was markedly increased, at a ratio of 4:1, for the LLC1 lung tumor tissue.

We also analyzed the microvasculature of lung tumors using μCT and fpvCT in a follow-up study up to one week after tumor cell seeding. 3D reconstructed images obtained by μCT revealed the entry and branching of the pulmonary artery in lung

tumors and detected capillaries as small as 9 μm in diameter. In addition, 3D images of the microfil-filled aorta illustrated the origin of the bronchial artery branching from the subclavian artery. This finding agrees with the observations of Verloop *et al.*, who studied the systemic blood vessels to the lung by using casting material (Verloop *et al.,* 1949).

In agreement with the μCT data, 3D fpvCT images also revealed close attachment of the lung tumors to the pulmonary artery. FpvCT allowed volumetric visualization of small pulmonary tumors down to a diameter of ~200 μm. In addition, the 3D images obtained by fpvCT revealed tissue bridges connecting pulmonary vasculature to the nodules.

In almost all types of cancer, tumor cells grow into solid neoplasms by using the host's pre-existing vasculature, which may originate from the pulmonary or bronchial system, or both. However, earlier studies that employed animal models to probe the origin of vascularization during lung tumor growth have reported conflicting results. Predominant nutrient supply from both the pulmonary and bronchial systems, via enlarged bronchial vessels, was observed (Jonas *et al.,* 1969; Muller *et al.,* 1978; Milne *et al.,* 1987; Bernard *et al.,* 1996; Mitzner *et al.,* 2000; Ley *et al.,* 2002).

These discrepancies might be explained in part by the tumor stage (Muller *et al.,* 1978), the species, the origin (primary tumor, metastasis), and the distribution (central, peripheral) of lung neoplasms. Milne *et al.* demonstrated the predominant perfusion of metastatic lung tumors by the pulmonary circulation in humans and rats (Milne *et al.,* 1987). In contrast, in primary lung tumors using in vivo angiography, Jonas *et al*. suggested the bronchial arterial supply as the primary source of nourishment in dogs. However, to the best of our knowledge, vascular supply of lung tumors in mice has not previously been investigated.

In our study of blood flow distribution to LLC1 primary lung tumors in C57/BL6 mice, the pulmonary arterial system had the predominant role, although the bronchogenic blood supply exists in this species. Our conclusion that bronchogenic blood supply of lung parenchyma and tumor tissue exists in C57/BL6 mice is based on i) the presence of bronchogenic blood flow markers in both healthy lungs and LLC1 tumors, ii) the detection of fluorescent microspheres in the cryosections, iii) the 3D-reconstruction of μCT images, which clearly demonstrated a left bronchial artery at the level of the main stem bronchi originating from the subclavian artery, consistent

with studies performed on different species (Jonas *et al.,* 1969; Muller *et al.,* 1978; Mitzner *et al.,* 2000; Ferreira *et al.,* 2001; Ley *et al.,* 2002), and iv) the possibility of arterial anastomoses between the bronchial and pulmonary circulation, as suggested by our observation of systemically applied (red) microspheres, found in the parenchymal capillaries of the lung.

In conclusion, this study clearly shows that the pulmonary arterial system plays the predominant role in the blood flow to LLC1 primary lung tumors in mice, as based on the analysis of fluorescent microspheres distribution and CT imaging.

6. Summary

Two mouse models of lung cancer were used to investigate cancer progression, cancer treatment, and cancer imaging. One model was established by subcutaneous injection of human adenocarcinoma A549 cells and lewis lung carcinoma (LLC1) cells, the other by intratracheal instillation of LLC1 cells.

In the first study, the role of HIF-1 in tumor progression was investigated. Overexpression of HIF-1α by genetic alteration of adenocarcinoma cells decreased tumor size, due to decreased proliferation and increased apoptosis, despite an augmented vascularization observed in these tumors.

In a further study, tumor regression by immunological approaches was attempted. Hybrids were generated by fusing dendritic cells and syngeneic poorly immunogenic LLC1 cells of C57/BL6 origin. Hybrid immunization induced the expression of a variety of cytokines and the partial host protective immunity against LLC1 tumor challenge. Moreover, hybrid vaccination and adoptive immunotherapy resulted in notable tumor regression.

For establishing small animal tumor imaging in our study, three different imaging modalities, micro computed tomography (μCT), multi slice computed tomography (MSCT), and flat panel volumetric computed tomography (fpvCT) were investigated.

The μCT images of intrapulmonary tumors suggested that μCT is a reliable and non-destructive method for quantifying the volume of intrapulmonary tumors in the mouse model. In addition, μCT can be used to evaluate tumor angiogenesis.

We exploited MSCT and fpvCT for the in vivo imaging and detection of lung nodules in a mouse LLC1 lung tumor model. FpvCT allowed easy monitoring of a lung tumor model with high resolution, facilitating follow-up investigations in cancer research. In addition, the superiority of fpvCT over MSCT was clearly demonstrated.

Furthermore, both imaging modalities (μCT and fpvCT), along with fluorescent microspheres, were applied to delineate the relative contribution of blood supply via the pulmonary and the systemic arteries to LLC1 lung tumors. All three methods revealed the pulmonary artery to be the primary functional source for feeding vessels to the lung tumors. Moreover, both modalities demonstrated the microanatomy of the vessels and blood-supplying tissue.

The development of experimental mouse lung tumor models is essential to the understanding of tumor pathophysiology and vascular microanatomy. Our findings can be used to identify novel targets for anticancer treatment and for site specific drug targeting. Additionally, the successful employment of various computed tomography systems for lung cancer imaging in rodents offers in vivo evaluation of such strategies.

7 Zusammenfassung

Zur Untersuchung von Tumorwachstum, Tumortherapie und Tumordarstellung wurden zwei verschiedene Lungentumor-Mausmodelle etabliert. Das eine Modell wurde durch die subkutane Injektion von menschlichen Adenokarzinom A549 Zellen oder Lewis-lung-karzinom zellen (LLC1), das andere durch die intratracheale Verabreichung von LLC1 Zellen ausgelöst.

In der ersten Studie wurde die Rolle von HIF-1 auf das Tumorwachstum analysiert. Die genetisch verursachte Überexpression von HIF-1α in Adenokarzinom-Zellen führte, trotz erhöhter Gefäßbildung in den untersuchten Tumoren, über eine verminderte Proliferation und gesteigerte Apoptose zu einer Verminderung des Tumorwachstums.

Eine weitere Untersuchung beschäftigte sich mit einem immunologischen Ansatz der Tumortherapie. Es wurden dendritische Zellen und syngene, schwach immunogene LLC1 Zellen, abgeleitet von C57/BL6 Mäusen, fusioniert. Immunisierung mit diesen Zellhybriden induzierte die Expression verschiedener Zytokine. Desweiteren wurde eine effektive Immunantwort gegen schwach immunogene Tumorzellen und eine gesteigerte T-lymphozytär vermittelte Zerstörung der Tumorzellen beobachtet. Dieser Effekt ließ sich sowohl durch Zellhybrid-Vakzinierung als auch durch die Übertragung von zuvor Zell hybrid-aktivierten T-Lymphozyten herbeiführen.

Zur Darstellung der induzierten Maus-Tumore wurden die Methoden der Mikro-Computertomographie (μCT), der Mehrschicht- Computertomographie (MSCT) und der Flachwandvolumen- Computertomographie (fpvCT) angewendet.

Die μCT Darstellung von intrapulmonalen Tumoren erwies sich als eine geeignete, nicht-destruktive Methode für die Quantifizierung des Tumorvolumens. Außerdem war es mit μCT möglich, die Gefäßversorgung der Tumore darzustellen.

Weiterhin haben wir die in vivo Darstellung und Detektion von Lungentumorknoten im LLC1-Lungen Modell mittels MSCT und fpvCT, untersucht. Aufgrund der

präzisen Bestimmung der Tumorgröße ermöglicht die fpvCT die Analyse der Tumorprogression in zeitlicher Abfolge. Zusätzlich konnte eine Überlegenheit der fpvCT gegenüber der MSCT nachgewiesen werden.

In Ergänzung wurden die Methoden der μCT und fpvCT zur Detektion von Fluoreszenzmikropartikeln für die Differenzierung von pulmonalarteriellen und systemarteriellen Blutflusses hinsichtlich der Versorgung des Tumorgewebes eingesetzt. Der strenge Hinweis, dass die Pulmonalarterien als funktionelle Quelle der Lungentumorgefäßversorgung dienten, konnte von allen drei eingesetzten Methoden erbracht werden. Darüber hinaus war es möglich, die Mikroanatomie der Gefäße sowie blutversorgende Gewebsbrücken darzustellen.

8 References

Abdel-Rahman SZ, El-Zein RA, Zwischenberger JB, Au WW. Association of the NAT1*10 genotype with increased chromosome aberrations and higher lung cancer risk in cigarette smokers. Mutat Res 1998;398:43-54.

Aebersold DM, Burri P, Beer KT, Laissue J, Djonov V, Greiner RH, Semenza GL. Expression of hypoxia-inducible factor-1alpha: a novel predictive and prognostic parameter in the radiotherapy of oropharyngeal cancer. Cancer Res 2001;61:2911-2916.

Amos CI, Xu W, Spitz MR. Is there a genetic basis for lung cancer susceptibility? Recent Results Cancer Res 1999;151:3-12.

Arriagada R, Pignon JP, Ihde DC, Johnson DH, Perry MC, Souhami RL, Brodin O, Joss RA, Kies MS, Lebeau B. Effect of thoracic radiotherapy on mortality in limited small cell lung cancer. A meta-analysis of 13 randomized trials among 2,140 patients. Anticancer Res 1994;14:333-335.

Banat GA, Christ O, Cochlovius B, Pralle HB, Zoller M. Tumour-induced suppression of immune response and its correction. Cancer Immunol Immunother 2001;49:573-586.

Banat GA, Usluoglu N, Hoeck M, Ihlow K, Hoppmann S, Pralle H. Dendritic cells fused with core binding factor-beta positive acute myeloid leukaemia blast cells induce activation of cytotoxic lymphocytes. Br J Haematol 2004:126:593-601.

Barr LF, Campbell SE, Diette GB, Gabrielson EW, Kim S, Shim H Dang CV. c-Myc suppresses the tumorigenicity of lung cancer cells and down-regulates vascular endothelial growth factor expression. Cancer Res 2000;60:143-149.

Beadsmoore CJ, Screaton NJ. Classification, staging and prognosis of lung cancer. Eur J Radiol 2003;45:8-17.

Beahrs OH, Henson DE, Hutter RP. American Joint Committee on Cancer (AJCC) "Lung" Manual for staging of cancer, 4th ed (1992), pp. 120 JB Lippincott, Philadelphia.

Beasley MB, Brambilla E, Travis WD. The 2004 World Health Organization classification of lung tumors. Semin Roentgenol 2005;40:90-97.

Beasley NJ, Leek R, Alam M, Turley H, Cox GJ, Gatter K, Millard P, Fuggle S, Harris AL. Hypoxia-inducible factors HIF-1α and HIF-2α in head and neck cancer: relationship to tumor biology and treatment outcome in surgically resected patients. Cancer Res 2002;62:2493-2497.

Bentley MD, Ortiz MC, Ritman EL, Romero JC. The use of micro computed tomography to study microvasculature in small rodents. Am J Physiol Regul Integr Comp Physiol 2002;282:R1267–R1279.

Bernard SL, Glenny RW, Polissar NL, Luchtel DL, Lakshminarayan S. Distribution of pulmonary and bronchial blood supply to airways measured by fluorescent microspheres. J Appl Physiol 1996;80:430-436.

Birner P, Schindl M, Obermair A, Breitenecker G, Oberhuber G. Expression of hypoxia-inducible factor 1alpha in epithelial ovarian tumors: its impact on prognosis and on response to chemotherapy. Clin Cancer Res 2001;7:1661-1668.

Birner P, Schindl M, Obermair A, Plank C, Breitenecker G, Oberhuber G. Overexpression of hypoxia-inducible factor 1alpha is a marker for an unfavorable prognosis in early-stage invasive cervical cancer. Cancer Res 2000;60:4693-4696.

Blancher C, Moore JW, Talks KL, Houlbrook S, Harris AL. Relationship of hypoxia-inducible factor (HIF)-1α and HIF-2α expression to vascular endothelial growth factor induction and hypoxia survival in human breast cancer cell lines. Cancer Res 2000;60:7106-7113.

Boczkowski D, Nair SK, Snyder D, Gilboa E. Dendritic cells pulsed with RNA are potent antigen-presenting cells in vitro and in vivo. J Exp Med 1996;184:465-472.

Bouck N. Tumor angiogenesis: the role of oncogenes and tumor suppressor genes. Cancer Cells 1990;2:179-185.

Boon T, Coulie PG, Van den Eynde B. Tumor antigens recognized by T cells. Immunol Today 1997;18:267-268.

Bray F, Guerra Yi M, Parkin DM. The comprehensive cancer monitoring programme in Europe. Eur J Public Health 2003;13:61-66.

Brossart P, Goldrath AW, Butz EA, Martin S, Bevan MJ. Virus-mediated delivery of antigenic epitopes into dendritic cells as a means to induce CTL. J Immunol 1997;158:3270-3276.

Bruick RK. Expression of the gene encoding the proapoptotic Nip3 protein is induced by hypoxia. Proc Natl Acad Sci 2000;97:9082-9087.

Bremer C, Ntziachristos V, Weissleder R. Optical-based molecular imaging: contrast agents and potential medical applications. Eur Radiol 2003;13:231-243.

Bremer C, Tung CH, Weissleder R. Molecular imaging of MMP expression and therapeutic MMP inhibition. Acad Radiol 2002;2:314-315.

Bunn HF, Poyton RO. Oxygen sensing and molecular adaptation to hypoxia. Physiol Rev 1996;76:839-885.

Budinger TF, Benaron DA, Koretsky AP. Imaging transgenic animals. Annu Rev Biomed 1999;1:611-648.

Burri P, Djonov V, Aebersold DM, Lindel K, Studer U, Altermatt HJ, Mazzucchelli L, Greiner RH, Gruber G. Significant correlation of hypoxia-inducible factor-1alpha with treatment outcome in cervical cancer treated with radical radiotherapy. Int J Radiat Oncol Biol Phys 2003;56:494-501.

Carmeliet P, Dor Y, Herbert JM, Fukumura D, Brusselmans K, Dewerchin M, Neeman M, Bono F, Abramovitch R, Maxwell P, Koch CJ, Ratcliffe P, Moons L, Jain RK, Collen D, Keshert E, Keshet E. Role of HIF-1α in hypoxia-mediated apoptosis, cell proliferation and tumor angiogenesis. Nature 1998;394:485-490.

Celluzzi CM, Falo LD. Physical interaction between dendritic cells and tumor cells results in an immunogen that induces protective and therapeutic tumor rejection. J Immunol 1998;160:3081-3085.

Chambers AF, Groom AC, MacDonald IC. Dissemination and growth of cancer cells in metastatic sites. Nat Rev Cancer 2002;2:563-572.

Chiba I, Takahashi T, Nau MM, D'Amico D, Curiel DT, Mitsudomi T, Buchhagen DL, Carbone D, Piantadosi S, Koga H. Mutations in the p53 gene are frequent in primary, resected non-small-cell lung cancer. Oncogene 1990;5:1603-1610.

Coleman MP, Gatta G, Verdecchia A, Esteve J, Sant M, Storm H, Allemani C, Ciccolallo L, Santaquilani M, Berrino F; EUROCARE Working Group. EUROCARE-3 summary: cancer survival in Europe at the end of the 20th century. Ann Oncol 2003;14:128-149.

Dang CV, Semenza GL. Oncogenic alterations of metabolism. Trends Biochem Sci 1999;24:68-72.

Elson DA, Thurston G, Huang LE, Ginzinger DG, McDonald DM, Johnson RS, Arbeit JM. Induction of hypervascularity without leakage or inflammation in transgenic mice overexpressing hypoxia-inducible factor-1alpha. Genes Dev 2001;15:2520-2532.

Feldkamp LA, Goldstein SA, Parfitt AM, Jesion G, Kleerekoper M. The direct examination of three-dimensional bone architecture in vitro by computed tomography. J Bone Miner Res 1989;4:3-11.

Feigal EG, Christian M, Cheson B, Grever M, Friedman MA. New chemotherapeutic agents in non-small-cell lung cancer. Semin Oncol 1993;20:185-201.

Ferreira PG, Silva AC, Águas AP, Pereira AS, Grande NR. Detailed arrangement of the bronchial arteries in the Wistar rat: A study using vascular injection and scanning electron microscopy. Eur J Anat 2001;5:67-76.

Ford NL, Thornton MM, Holdsworth DW. Fundamental image quality limits for microcomputed tomography in small animals. Med Phys 2003;30:2869-2877.

Frija G, Flahault A, Lemarie E. Spiral CT is it time for lung cancer screening? Bull Acad Natl Med 2003;187:153-160.

Fukuda R, Hirota K, Fan F, Jung YD, Ellis LM, Semenza GL. Insulin-like growth factor 1 induces hypoxia-inducible factor 1-mediated vascular endothelial growth factor expression, which is dependent on MAP kinase and phosphatidylinositol 3-kinase signaling in colon cancer cells. J Biol Chem 2002;277:38205-38211.

Gazdar A, Shoemaker R, Mayo J. Human lung cancer xenografts and metastases in athymic (nude) mice. In: Rygaard N, Brunner N, Graem N, Spang-Thornsen M, editors. Immune-dificient animals in biomedical research. Basel: Karger;1987. p. 277.

Ge Q, Palliser D, Eisen HN, Chen J. Homeostatic T cell proliferation in a T cell-dendritic cell coculture system. Proc Natl Acad Sci USA 2002;99:2983-2988.

Giaccone G, Manegold C, Rosell R, Gatzemeier U, Quoix E. An update on European randomized studies in non-small cell lung cancer. Semin Oncol 1998;25:11-17.

Gilboa E, Nair SK, Lyerly HK. Immunotherapy of cancer with dendritic-cell-based vaccines. Cancer Immunol Immunother 1998;46:82-87.

Giovanella BC, Stehlin JS Jr, Shepard RC, Williams LJ. Correlation between response to chemotherapy of human tumors in patients and in nude mice. Cancer 1983;52:1146-1152.

Goda N, Ryan HE, Khadivi B, McNulty W, Rickert RC, Johnson RS. Hypoxia-inducible factor 1alpha is essential for cell cycle arrest during hypoxia. Mol Cell Biol 2003;23:359-369.

Gong J, Chen D, Kashiwaba M, Kufe D. Induction of antitumor activity by immunization with fusions of dendritic and carcinoma cells. Nat Med 1997;3:558-561.

Halme M, Jekunen A, Tamminen K, Mattson K. Phase II study of weekly gemcitabine in advanced non-small cell lung cancer. Res Med 1997;91:423-426.

Goyal P, Weissmann N, Grimminger F, Hegel C, Bader L, Rose F, Fink L, Ghofrani HA, Schermuly RT, Schmidt HH, Seeger W, Hanze J. Upregulation of NAD(P)H oxidase 1 in hypoxia activates hypoxia-inducible factor 1 via increase in reactive oxygen species. Free Radic Biol Med 2004;36:1279-1288.

Halevy O, Michalovitz D, Oren M. Different tumor-derived p53 mutants exhibit distinct biological activities. Science 1990;250:113-116.

Hanze J, Eul BG, Savai R, Krick S, Goyal P, Grimminger F, Seeger W, Rose F. RNA interference for HIF-1alpha inhibits its downstream signaling and affects cellular proliferation. Biochem Biophys Res Commun 2003;312:571-577.

Hirsch FR, Franklin WA, Gazdar AF, Bunn PA Jr. Early detection of lung cancer: clinical perspectives of recent advances in biology and radiology. Clin Cancer Res 2001;7:5-22.

Hockel M, Vaupel P. Tumor hypoxia: definitions and current clinical, biologic, and molecular aspects. J Natl Cancer Inst 2001;93:266-276.

Holdsworth DW, Thornton MM. Micro-CT in small animal and specimen imaging. Trends Biotechnol 2002;20:S34–S39.

Hollstein M, Sidransky D, Vogelstein B, Harris CC. P53 mutations in human cancers. Science 1991;253:49-53.

Iwamaru A, Watanabe M, Yu S, Ohtsuka T, Horinouchi H, Kobayashi K. Measurement of tumor blood flow using colored dye extraction microspheres in two rat tumor models. Int J Oncol 2001;18:227-232.

Iwamaru A, Watanabe M, Ohtsuka T, Horinouchi H, Kobayashi K. Analysis of angiogenic profiles by estimation of tumor blood flow with colored dye extraction microspheres after antiangiogenic therapy. Oncol Rep 2003;10:1127-1131.

Jiang YA, Fan LF, Jiang CQ, Zhang YY, Luo HS, Tang ZJ, Xia D, Wang M. Expression and significance of PTEN, hypoxia-inducible factor-1 alpha in colorectal adenoma and adenocarcinoma. World J Gastroenterol 2003;9:491-494.

Jonas AM, Carrington CB. Vascular patterns in primary and secondary pulmonary tumors in the dog. Am J Pathol 1969;56:79-95.

Jorgensen SM, Demirkaya O, Ritman EL. Three-dimensional imaging of vasculature and parenchyma in intact rodent organs with X-ray micro-CT. Am J Physiol 1998;275:H1103-H1114.

Jung M, Davis WP, Taatjes DJ, Churg A, Mossman BT. Asbestos and cigarette smoke cause increased DNA strand breaks and necrosis in bronchiolar epithelial cells in vivo. Free Radic Biol Med 2000;28:1295-1299.

Kalender WA. The use of flat-panel detectors for CT imaging. Radiologe 2003;43:379-387.

Kantor B, Ritman EL, Holmes Jr DR, Schwartz RS. Imaging Angiogenesis with Three-Dimensional Microscopic Computed Tomography. Curr Interv Cardiol Rep 2000;3:204-212.

Kawada M, Ikeda H, Takahashi T, Ishizu A, Ishikura H, Katoh H, Yoshiki T. Vaccination of fusion cells of rat dendritic and carcinoma cells prevents tumor growth in vivo. Int J Cancer 2003;105:520-526.

Kennel SJ, Davis IA, Branning J, Pan H, Kabalka GW, Paulus MJ. High resolution computed tomography and MRI for monitoring lung tumor growth in mice undergoing radioimmunotherapy: correlation with histology. Med Phys 2000;27:1101-1107.

Kerbel RS. Antiangiogenic drugs and current strategies for the treatment of lung cancer. Semin Oncol 2004;31:54-60.

Kiessling F, Krix M, Heilmann M, Vosseler S, Lichy M, Fink C, Farhan N, Kleinschmidt K, Schad L, Fusenig NE, Delorme S. Comparing dynamic parameters of tumor vascularization in nude mice revealed by magnetic resonance imaging and contrast-enhanced intermittent power Doppler sonography. Invest Radiol 2003;38:516-524.

Kiessling F, Greschus S, Lichy MP, Bock M, Fink C, Vosseler S, Moll J, Mueller MM, Fusenig NE, Traupe H, Semmler W. Volumetric computed tomography (VCT):

a new technology for noninvasive, high-resolution monitoring of tumor angiogenesis. Nat Med 2004;10:1133-1138.

Kiessling F, Huber PE, Grobholz R, Heilmann M, Meding J, Lichy MP, Fink C, Krix M, Peschke P, Schlemmer HP. Dynamic magnetic resonance tomography and proton magnetic resonance spectroscopy of prostate cancers in rats treated by radiotherapy. Invest Radiol 2004;39:34-44.

Killion JJ, Radinsky R, Fidler IJ. Orthotopic models are necessary to predict therapy of transplantable tumors in mice. Cancer Metastasis Rev 1998;17:279-284.

Kwon HM, Sangiorgi G, Ritman EL, Lerman A, McKenna C, Virmani R, Edwards WD, Holmes DR, Schwartz RS. Adventitial vasa vasorum in balloon-injured coronary arteries: visualization and quantitation by a microscopic three-dimensional computed tomography technique. J Am Coll Cardiol 1998;32:2072-2079.

Kreyberg L, Liebow AA, Uehlinger EA. International Histologic Classification of Tumors: No. 1. Histological Typing of Lung Tumors. Geneva: World Health Organization, 2nd ed., 1981.

Krix M, Kiessling F, Vosseler S, Farhan N, Mueller MM, Bohlen P, Fusenig NE, Delorme S. Sensitive noninvasive monitoring of tumor perfusion during antiangiogenic therapy by intermittent bolus-contrast power Doppler sonography. Cancer Res 2003;63:8264-8270.

Kwak SY, Tsai, DeMayo FJ. Genetically engineered mouse models for lung cancer, Annu Rev Physiol 2004;66:647–663.

Lam S, leRiche JC, Zheng Y, Coldman A, MacAulay C, Hawk E, Kelloff G, Gazdar AF. Sex-related differences in bronchial epithelial changes associated with tobacco smoking. J Natl Cancer Inst 1999;91:691-696.

Langheinrich AC, Leithauser B, Greschus S, Von Gerlach S, Breithecker A, Matthias FR, Rau WS, Bohle RM. Acute rat lung injury: feasibility of assessment with micro-CT. Radiology 2004;233:165-171.

Laughner E, Taghavi P, Chiles K, Mahon PC, Semenza GL. HER2 (neu) signaling increases the rate of hypoxia-inducible factor 1alpha (HIF-1α) synthesis: novel mechanism for HIF-1-mediated vascular endothelial growth factor expression. Mol Cell Biol 2001;21:3995-4004.

Lee J, Mao L, Hong W. Biology of preneoplastic lesions. In: Roth J, Cox J, Hong W eds. lung cancer 2nd Ed. Oxford: Blackwell Science, 1998.

Lehr HA, Leunig M, Menger MD, Nolte D, Messmer K. Dorsal skinfold chamber technique for intravital microscopy in nude mice. Am J Pathol 1993;143:1055-1062.

Levi F, Lucchini F, Negri E, Boyle P, La Vecchia C. Cancer Mortality in Europe 1995-1999, and an Overview of Trends since 1960. Int J Cancer 2004;110:155-169.

Lewis JS, Achilefu S, Garbow JR, Laforest R, Welch MJ. Small animal imaging current technology and perspectives for oncological imaging. Eur J Cancer 2002;38:2173-2188.

Liotta LA, Steeg PS, Stetler-Stevenson WG. Cancer metastasis and angiogenesis: an imbalance of positive and negative regulation. Cell 1991;64:327-336.

Littman AJ, White E, Jackson LA, Thornquist MD, Gaydos CA, Goodman GE, Vaughan TL. Chlamydia pneumoniae infection and risk of lung cancer. Cancer Epidemiol Biomarkers Prev 2004;13:1624-1630.

Ley S, Kreitner KF, Morgenstern I, Thelen M, Kauczor HU. Bronchopulmonary shunts in patients with chronic thromboembolic pulmonary hypertension: evaluation with helical CT and MR imaging. AJR Am J Roentgenol 2002;179:1209-1215.

Lorenz J, Friedberg T, Paulus R, Oesch F, Ferlinz R. Oncogene overexpression in non-small-cell lung cancer tissue: prevalence and clinicopathological significance. Clin Investig 1994;72:156-163.

Luo G, Kinney JH, Kaufman JJ, Haupt D, Chiabrera A, Siffert RS. Relationship between plain radiographic patterns and three- dimensional trabecular architecture in the human calcaneus. Osteoporos Int 1999;9:339-345.

Maehara N. Experimental microcomputed tomography study of the 3D microangioarchitecture of tumors. Eur Radiol 2003;13:1559-1565.

Mahmood U, Tung CH, Bogdanov A Jr, Weissleder R. Near-infrared optical imaging of protease activity for tumor detection. Radiology 1999;213:866-870.

Mattson K, Saarinen A, Jekunen A. Combination treatment with docetaxel (Taxotere) and platinum compounds for non-small cell lung cancer. Semin Oncol 1997;24:S14-5-S14-8.

Maxwell PH, Dachs GU, Gleadle JM, Nicholls LG, Harris AL, Stratford IJ, Hankinson O, Pugh CW, Ratcliffe PJ. Hypoxia-inducible factor-1 modulates gene

expression in solid tumors and influences both angiogenesis and tumor growth. Proc Natl Acad Sci U S A 1997;94:8104-8109.

McLemore TL, Eggleston JC, Shoemaker RH, Abbott BJ, Bohlman ME, Liu MC, Fine DL, Mayo JG, Boyd MR. Comparison of intrapulmonary, percutaneous intrathoracic, and subcutaneous models for the propagation of human pulmonary and nonpulmonary cancer cell lines in athymic nude mice. Cancer Res 1988;48:2880-2886.

Michael B. Rubens, Simon PG, Padley A. Tumors of the lung. Textbook of Radiology and Imaging. TR7E-04(107-130) 6/24/02.

Milne EN, Zerhouni EA. Blood supply of pulmonary metastases. J Thorac Imaging 1987;2:15-23.

Mitzner W, Lee W, Georgakopoulos D, Wagner E. Angiogenesis in the mouse lung. Am J Pathol 2000;157:93-101.

Mitzner W, Brown R, Lee W. In vivo measurement of lung volumes in mice. Physiol Genomics 2001;4:215-221.

Mountain CF, Dresler CM. Regional lymph node classification for lung cancer staging. Chest 1997;111:1718-1723.

Mountain CF. Revisions in the International System for Staging Lung Cancer. Chest 1997;111:1710-1717.

Muller KM, Meyer-Schwickerath M. Bronchial arteries in various stages of bronchogenic carcinoma. Pathol Res Pract 1978;163:34-46.

Nair SK, Snyder D, Rouse BT, Gilboa E. Regression of tumors in mice vaccinated with professional antigen-presenting cells pulsed with tumor extracts. Int J Cancer 1997;70:706-715.

Nair SK, Boczkowski D, Morse M, Cumming RI, Lyerly HK, Gilboa E. Induction of primary carcinoembryonic antigen (CEA)-specific cytotoxic T lymphocytes in vitro using human dendritic cells transfected with RNA. Nat Biotechnol 1998;16:364-369.

Nestle FO, Alijagic S, Gilliet M, Sun Y, Grabbe S, Dummer R, Burg G, Schadendorf D. Vaccination of melanoma patients with peptide- or tumor lysate-pulsed dendritic cells. Nat Med 1998;4:328-332.

Noordijk EM, vd Poest Clement E, Hermans J, Wever AM, Leer JW. Radiotherapy as an alternative to surgery in elderly patients with resectable lung cancer. Radiother Oncol 1988;13:83-89.

Ntziachristos V, Bremer C, Weissleder R. Fluorescence imaging with near-infrared light: new technological advances that enable in vivo molecular imaging. Eur Radiol 2003;13:195-208.

Nyberg F, Agrenius V, Svartengren K, Svensson C, Pershagen G. Dietary factors and risk of lung cancer in never-smokers. Int J Cancer 1998;78:430-436.

Ohshima Y, Delespesse G. T cell-derived IL-4 and dendritic cell-derived IL-12 regulate the lymphokine-producing phenotype of alloantigen-primed naive human CD4 T cells. J Immunol 1997;158:629-636.

Pechhold K, Pohl T, and Kabelitz D. Rapid quantification of lymphocyte subsets in heterogeneous cell populations by flow cytometry. Cytometry 1994;16:152-159.

Perez-Soler R, Chachoua A, Hammond LA, Rowinsky EK, Huberman M, Karp D, Rigas J, Clark GM, Santabarbara P, Bonomi P. Determinants of tumor response and survival with erlotinib in patients with non--small-cell lung cancer. J Clin Oncol 2004;22:3238-3247.

Perez-Soler R. The role of erlotinib (Tarceva, OSI 774) in the treatment of non-small cell lung cancer. Clin Cancer Res 2004;10:4238s-4240s.

Pignon JP, Arriagada R, Ihde DC, Johnson DH, Perry MC, Souhami RL, Brodin O, Joss RA, Kies MS, Lebeau B. A meta-analysis of thoracic radiotherapy for small-cell lung cancer. N Engl J Med 1992;327:1618-1624.

Plathow C, Li M, Gong P, Zieher H, Kiessling F, Peschke P, Kauczor HU, Abdollahi A, Huber PE. Computed tomography monitoring of radiation-induced lung fibrosis in mice. Invest Radiol 2004;39:600-609.

Porgador A, Gilboa E. Bone marrow-generated dendritic cells pulsed with a class I-restricted peptide are potent inducers of cytotoxic T lymphocytes. J Exp Med 1995;182:255-260.

Prins J, De Vries EG, Mulder NH. The myc family of oncogenes and their presence and importance in small-cell lung carcinoma and other tumour types. Anticancer Res 1993;13:1373-1385.

Pritchard RS, Anthony SP. Chemotherapy plus radiotherapy compared with radiotherapy alone in the treatment of locally advanced, unresectable, non-small-cell lung cancer. A meta-analysis. Ann Intern Med 1996;125:723-729.

Quinn MJ. Cancer trends in the United States-a view from Europe. J Natl Cancer Inst 2003;95:1258-1261.

Ravi R, Mookerjee B, Bhujwalla ZM, Sutter CH, Artemov D, Zeng Q, Dillehay LE, Madan A, Semenza GL, Bedi A. Regulation of tumor angiogenesis by p53-induced degradation of hypoxia-inducible factor 1alpha. Genes Dev 2000;14:34-44.

Rodenhuis S, Slebos RJ. The ras oncogenes in human lung cancer. Am Rev Respir Dis 1990;142:S27-30.

Rojas M, Marie B, Vignaud JM, Martinet N, Siat J, Grosdidier G, Cascorbi I, Alexandrov K. High DNA damage by benzo[a]pyrene 7,8-diol-9,10-epoxide in bronchial epithelial cells from patients with lung cancer: comparison with lung parenchyma. Cancer Lett 2004;207:157-163.

Roland M, Rudd RM. Genetics and pulmonary medicine. 7. Somatic mutations in the development of lung cancer. Thorax 1998;53:979-983.

Roth JA, Atkinson EN, Fossella F, Komaki R, Bernadette Ryan M, Putnam JB Jr, Lee JS, Dhingra H, De Caro L, Chasen M, Hong WK. Long-term follow-up of patients enrolled in a randomized trial comparing perioperative chemotherapy and surgery with surgery alone in resectable stage IIIA non-small-cell lung cancer. Lung Cancer 1998;21:1-6.

Rosenberg SA. Progress in human tumor immunology and immunotherapy. Nature 2001;411:380-384.

Ryan HE, Lo J, Johnson RS. HIF-1α is required for solid tumor formation and embryonic vascularization. EMBO J 1998;17:3005-3015.

Shen Z, Reznikoff G, Dranoff G, Rock KL. Cloned dendritic cells can present exogenous antigens on both MHC class I and class II molecules. J Immunol 1997;158:2723-2730.

Schindl M, Schoppmann SF, Samonigg H, Hausmaninger H, Kwasny W, Gnant M, Jakesz R, Kubista E, Birner P, Oberhuber G. Overexpression of hypoxia-inducible factor 1alpha is associated with an unfavorable prognosis in lymph node-positive breast cancer. Clin Cancer Res 2002;8:1831-1837.

Schmaltz C, Hardenbergh PH, Wells A, Fisher DE. Regulation of proliferation-survival decisions during tumor cell hypoxia. Mol Cell Biol 1998;18:2845-2854.

Schuler G, Steinman RM. Dendritic cells as adjuvants for immune-mediated resistance to tumors. J Exp Med 1997;186:1183-1187.

Schwartz AG, Rothrock M, Yang P, Swanson GM. Increased cancer risk among relatives of nonsmoking lung cancer cases. Genet Epidemiol 1999;17:1-15.

Schuster DP, Kovacs A, Garbow J, Piwnica-Worms D. Recent advances in imaging the lungs of intact small animals. Am J Respir Cell Mol Biol 2004;30:129-138.

Semenza GL, Wang GL. A nuclear factor induced by hypoxia via de novo protein synthesis binds to the human erythropoietin gene enhancer at a site required for transcriptional activation. Mol Cell Biol 1992;12:5447-5454.

Semenza GL. Transcriptional regulation by hypoxia-inducible factor-1. Trends Cardiovasc Med 1996;6:151-157.

Semenza GL. Targeting HIF-1 for cancer therapy. Nat Rev Cancer 2003;3:721-732.

Shah SS, Goldstraw P. Combined pulmonary and thoracic wall resection for stage III lung cancer. Thorax 1995;50:782-784.

Sobin LH, Wittekind CH. International Union Against Cancer (UICC) "Lung tumors (ICDO-162)" *TNM Classification of malignant tumors*, 1997;5th ed Wiley-Liss, New York.

Steenland K, Stayner L. Silica, asbestos, man-made mineral fibers, and cancer. Cancer Causes Control 1997;8:491-503.

Stewart LA, Burdett S & Souhami Rl. Post-operative radiotherapy (PORT) in non-small cell lung cancer (NSCLC): A meta-analysis using individual patients data (IPD) from randomised clinical trials (RCTS). Proceedings of the American Society of Clinical Oncology 1998;17:457a.

Taillade L, Soria JC, Andre F, Grunenwald D, Dunant A, Pignon JP, Le Chevalier T. Adjuvant chemotherapy in non-small cell lung cancer. Bull Cancer 2004;91:63-67.

Talks KL, Turley H, Gatter KC, Maxwell PH, Pugh CW, Ratcliffe PJ, Harris AL. The expression and distribution of the hypoxia-inducible factors HIF-1α and HIF-2α in normal human tissues, cancers, and tumor-associated macrophages. Am J Pathol 2000;157:411-421.

Timmerman JM, Levy R. Dendritic cell vaccines for cancer immunotherapy. Annu Rev Med 1999;50:507-529.

Travis WD, Brambilla E, Mullar-Hermelink, Harris CC. (Eds.): World Health Organization Classification of Tumours. Pathology and Genetics of Tumours of the Lung, Pleura, Thymus and Heart. IARC Press: Lyon 2004.

Tuveson DA, Jacks T. Modeling human lung cancer in mice: similarities and shortcomings. Oncogene 1999;18:5318-5324.

van den Broeke LT, Daschbach E, Thomas EK, Andringa G, Berzofsky JA. Dendritic cell-induced activation of adaptive and innate antitumor immunity. J Immunol 2003;171:5842-5852.

Verloop MC. On the arteriae bronchiales and their anastomosing with the arteria pulmonalis in some rodents; a micro-anatomical study. Acta Anat 1949;7:1-32.

Volm M, Koomagi R. Hypoxia-inducible factor (HIF-1) and its relationship to apoptosis and proliferation in lung cancer. Anticancer Res 2000;20:1527-1533.

Wada H, Tanaka F, Yanagihara K, Ariyasu T, Fukuse T, Yokomise H, Inui K, Mizuno H, Ike O, Hitomi S. Time trends and survival after operations for primary lung cancer from 1976 through 1990. J Thorac Cardiovasc Surg 1996;112:349-355.

Wagner EM, Brown RH. Blood flow distribution within the airway wall. J Appl Physiol 2002;92:1964-1969.

Wang GL, Semenza GL. Purification and characterization of hypoxia-inducible factor 1. J Biol Chem 1995;270:1230-1237.

Weissleder R, Cheng HC, Marecos E, Kwong K, Bogdanov A, Non-invasive in vivo mapping of tumor vascular and interstitial volume fractions. Eur J Cancer 1998;34:1448-1454.

Wistuba II, Behrens C, Milchgrub S, Virmani AK, Jagirdar J, Thomas B, Ioachim HL, Litzky LA, Brambilla EM, Minna JD, Gazdar AF. Comparison of molecular changes in lung cancers in HIV-positive and HIV-indeterminate subjects. JAMA 1998;279:1554-1559.

Wu CH, Lindsey DC, Traber DL, Cross CE, Herndon DN, Kramer GC. Measurement of bronchial blood flow with radioactive microspheres in awake sheep: J Appl Physiol 1988;65:1131-1139.

Yang S, Darrow TL, Vervaert CE, Seigler HF. mmunotherapeutic potential of tumor antigen-pulsed and unpulsed dendritic cells generated from murine bone marrow. Cell Immunol 1997;179:84-95.

Yang M, Baranov E, Li XM, Wang JW, Jiang P, Li L, Moossa AR, Penman S, Hoffman RM. Whole-body and intravital optical imaging of angiogenesis in orthotopically implanted tumors. Proc Natl Acad Sci U S A 2001;98:2616-21.

Zimmer M, Doucette D, Siddiqui N, Iliopoulos O. Inhibition of hypoxia-inducible factor is sufficient for growth suppression of VHL-/- tumors. Mol Cancer Res 2004;2:89-95.

Zhong H, De Marzo AM, Laughner E, Lim M, Hilton DA, Zagzag D, Buechler P, Isaacs WB, Semenza GL, Simons JW. Overexpression of hypoxia-inducible factor 1alpha in common human cancers and their metastases. Cancer Res 1999;59:5830-5835.

9 Abbreviations

APC	Antigen Presenting Cells
CM	Contrast Medium
CTLs	Cytotoxic T Lymphocytes
CT	Computed Tomography
DAPI	4'6-diamidino-2-phenylindole
DC	Dendritic Cells
DNA	Deoxy-ribo-nucleic acid
EGFR	Epidermal Growth Factor Receptor
fpvCT	flat panel volumetric Computed Tomography
HC	Hybrid Cells
HIF	Hypoxia inducible factor
HPRT	Hypoxanthine-Guanine Phosphoribosyl Transferase
LLC1	Lewis Lung Carcinoma
MHC	Major histocompatibility complex
MRI	Magnetic Resonance Imaging
mRNA	Messenger Ribonucleic Acid
NIP3	Proapoptotic Protein
NSCLC	Non-Small Cell Lung Cancer
PA	Pulmonary artery
PV	Pulmonary vein
PCR	Polymerase Chain Reaction
PET	Positron Emission Tomography
RNA	Ribonucleic Acid
RT	Reverse Transcriptase
SCLC	Small Cell Lung Cancer
SC/LNC	Spleen Cells/Lymphnode Cells
SD	Standard Deviation
SEM	Standard Error of the Mean
TAA	Tumor Associated Antigens
Th	T-helper cells
TM	Tumor Mass

TNM	Tumor, Node, and Metastasis
VEGF	Vascular Endothelial Growth Factor
UICC	Union International Contre Cancer
μCT	Micro Computed Tomography

10 Erklärung

“Ich erkläre: Ich habe die vorgelegte Dissertation selbständig, ohne unerlaubte fremde Hilfe und nur mit den Hilfen angefertigt, die ich in der Dissertaion angegeben habe. Alle Textstellen, die wörtlich oder sinngemäβ aus veröffentlichten oder nicht veröffentlichten Schriften entnommen sind, und alle Angaben, die auf mündlichen Auskünften beruhen, sind als solche kenntlich gemacht. Bei den von mir durchgeführten und in der Dissertation erwähnten Untersuchungen habe ich die Grundsätze guter wissenschaftlicher Praxis, wie sie in der” Satzung der Justus-Liebig-Universität Gieβen zur Sicherung guter wissenschaftlicher Praxis” niedergelegt sind, eingehalten.“

10 Acknowledgements

This thesis is the result of a three year intellectual odyssey for me as a researcher. As such, I must acknowledge all assistance received along the way from the faculty and my colleagues at University Hospital Giessen, including the directors who supported and funded my research.

I am very grateful to my supervisor Dr. Frank Rose providing me with invaluable guidance, constructive criticism, and encouragement throughout my doctoral endeavor.

A word of appreciation should go to the Chairman of the Department of Internal Medicine II, University Hospital Giessen, Prof. Dr. Werner Seeger, for giving me an invaluable opportunity to do my doctoral research. His suggestions and positive feedback were both inspiring and enlightening.

I express my deep gratitude to PD Dr. Jörg Hänze for his suggestions and assistance at every critical juncture.

I owe my thanks to Dr. Ralph Schermuly, who instructed me in animal handling, infusion methods, and in vivo results.

I would like to also thank Dr. Susanne Greschus and Dr. Joachim Claudius Wolf, from the Institute of Neuroradiology and Institute of Radiology, respectively, for their cooperation in all imaging experiments.

I also owe my special thanks and respect to Dr. Andre Banat, Department of Hematology and Oncology, Giessen, who introduced me to the field of tumor immunology, for his support and guidance.

A word of gratitude certainly goes to all colleagues and lab technicians for their insightful discussions and cooperation throughout my research work.

Finally, I appreciate the inspiration and encouragement provided by my family and friends.

11 Curriculum vitae

Rajkumar Savai

Department of Internal Medicine II

Division of Pulmonary and Critical Care Medicine

Justus-Liebig University

35392 Giessen

Phone No: 0641-99-42717/18

E-mail:Savai.rajkumar@innere.med.uni-giessen.de

Savaik@yahoo.com

Personal Information: Male, single, born in India on 4th January 1976

Educational History Summary: First class academic career throughout.

Degrees and Year	Major	Institution
M.Sc., 1999	Biochemistry	Kakatiya University, India
B.Sc., 1997	Botany, Zoology, Chemistry	Kakatiya University, India
Higher Secondary, 1994	Biology, Chemistry, Physics	Board of intermediate, India
Matriculation, 1992		Markazi School, India

Ph.D. student (February, 2002 – January, 2005)

Thesis topic: "Establishment of mouse tumor models and development of new therapeutic approaches"

Specific aims

- Establishment of lung mouse tumor models such as Adeno carcinoma, Lewis lung carcinoma and Lung metastasis.
- Analysis of the role of HIF-1α on in an adenocarcinoma mouse model.
- Study of tumor regression capabilities by dendritic/tumor cell hybrid-primed T-lymphocytes and hybrid vaccination in a lewis lung carcinoma model.
- Application of new imaging strategies in order to monitor tumorigenesis and tumor metastasis in vivo over time (multislice computed tomography, micro-computed tomography and flat-panel volumetric computed tomography).
- Employing the imaging techniques for delineating vessel architecture (vascularization) and blood supply of lung tumors.

Scientific presentations

2003*:* **Savai R**, Rose F, Haenze J, Schmidt S, Grimminger F, Krick S, Ghofrani HA, Weissmann N, Seeger W, Schermuly R.T: Modulation of Tumor Growth by Transfection with Hypoxia Inducible Factor-1α in CD-1 Nude Mice. ATS 2003-99th International Conference. Seattle.

2004: **Savai R,** Hänze J, Schermuly RT, Eul B, Reichmann B, Grimminger F, Seeger W, Rose F. Rolle von HIF-1α bei der Proliferation, Apoptose und Vaskularisierung in einem A549 Tumormodell der Maus. Pneumologie 2004-45.Kongress der Deutschen Gesellschaft für Pneumologie ***(Oral presentation)***

2004: **Savai R,** Wolf JC, Schermuly RT, Haenze J, Eul BG, Grimminger F, Seeger W, Rose F. Determination of Tumor Blood Flow in Mice Lung Tumors. ATS 2004-100th International Conference. Florida.

2004: J C Wolf, MD, **Savai R** MSc; S Greschus, MD; A C Langheinrich, MD; F Rose, MD; W S Rau, MD. Micro-computed Tomography Is a Valuable Tool for Quantitative Investigation of the Vessel Content in a Murine Intrapulmonary Lewis Lung Carcinoma Model. RSNA 2004, 90th Scientific Assembly and annual meeting, Chicago, USA

2004: Schneider, M., **Savai R**, Hoeck, M., Hoppmann, S., Schermuly, R., Pralle, H., Grimminger, F. and Banat, G.-A. Immunization with fusion of murine dendritic cells and LLC1 tumor cells elicit T cell immunity. Deutschen Gesellschaften für Hämatologie und Onkologie 2004.

2004: S Greschus, MD, **Savai R** MSc**,** J C Wolf, MD, F Rose, MD; W S Rau, MD; H Traupe, MD. In Vivo Monitoring of Lung Tumor Growth in Mice with Novel Flat-panel Detector Volumetric Computed Tomography RSNA 2004, 90th Scientific Assembly and annual meeting, Chicago, USA

2004: B. Eul, F. Rose, **Savai R,** P. Goyal, S. Krick, F. Grimminger, W. Kummer, W. Seeger, J. Hänze. Suppression des Transkriptionsfaktors HIF-1α durch RNA interference: Effekte auf Zielgene und Zellproliferation in A549 Zellen. Pneumologie 2004-45. Kongress der Deutschen Gesellschaft für Pneumologie

Personal skills and competencies

Telugu	:	Mother tongue
English	:	Fluent
German	:	Basic
Technical skills and Competencies	:	Microsoft Office, Basics of Oracle 6.0, Corel Draw, Adobe Photo Deluxe, Sigma Plot
Additional Information	**:**	Received merit scholarship for distinction in masters Winner in State level gymnastics

12 Publications

Published

1. **Savai R**, Wolf A, Greschus S, Eul BG, Schermuly R, Hänze J, Vosswinkel R, Langheinrich A, Grimminger F, Traupe H, Seeger W, and Rose F. Analysis of tumor vessel supply in Lewis Lung Carcinoma in mice by fluorescent microspheres distribution and imaging with micro- and volumetric- computed Tomography. ***Am J Pathol.*** 2005 Oct;167(4):937-46.

2. **Savai R**, Schermuly R, Voswinckel R, Reichmann B, Renigunta A, Eul BG, Grimminger F, Seeger W, Rose F, and Hänze J. HIF-1alpha attenuates tumor growth in spite of augmented vascularization in a A549 mouse tumor model. ***Int J Oncol.*** 2005 Aug 05; 27(2): 393-400.

3. **Savai R,** Schermuly R, Schneider M, Pullamsetti S, Rose F, Grimminger F and Banat GA. Hybrid-primed lymphocytes and hybrid vaccination prevent tumor growth of Lewis lung carcinoma in mice ***J Immunother.*** 2006 Mar-Apr;29(2):175-87.

4. Hanze J, Eul BG, **Savai R**, Krick S, Goyal P, Grimminger F, Seeger W, Rose F. RNA interference for HIF-1alpha inhibits its downstream signaling and affects cellular proliferation. ***Biochem Biophys Res Commun***. 2003 Dec19;312(3):571-7.

5. Krick S, Eul BG, Hänze J, **Savai R**, Grimminger F, Maus U, Lohmeyer J, Klepetko W, Seeger W and Rose F. Hypoxia driven proliferation of human pulmonary artery fibroblasts: crosstalk between HIF-1alpha and an autocrine angiotensin system. ***FASEB J***. 2005 May;19(7):857-9.

6. Krick S, Eul BG, Hanze J, **Savai R**, Grimminger F, Seeger W, Rose F. Role of HIF-1alpha in hypoxia-induced apoptosis of primary alveolar epithelial type II cells. ***Am J Respir Cell Mol Biol.*** 2005 May;32(5):395-403.

7. Greschus S, Kiessling F, Lichy MP, Moll J, Mueller MM, **Savai R**, Rose F, Ruppert C, Gunther A, Luecke M, Fusenig NE, Semmler W, Traupe H. Potential Applications of Flat-Panel Volumetric CT in Morphologic and Functional Small Animal Imaging. ***Neoplasia.*** 2005 Aug;7(8):730-40.

8. Schermuly RT, Dony E, Ghofrani HA, Pullamsetti S, **Savai R**, Roth M, Sydykov A, Lai YJ, Weissmann N, Seeger W, Grimminger F. Reversal of experimental pulmonary hypertension by PDGF inhibition. ***J Clin Invest.*** 2005 Oct;115(10):2811-21.

9. Eul BG, Rose F, Krick S, **Savai R,** Goyal P, Kleptko W, Seeger W and Hänze J. Specific intervention by RNA interference reveals the predominant role of HIF-2alpha in proliferation and migration of human pulmonary artery fibroblasts. ***FASEB J.*** 2006 Jan;20(1):163-5.

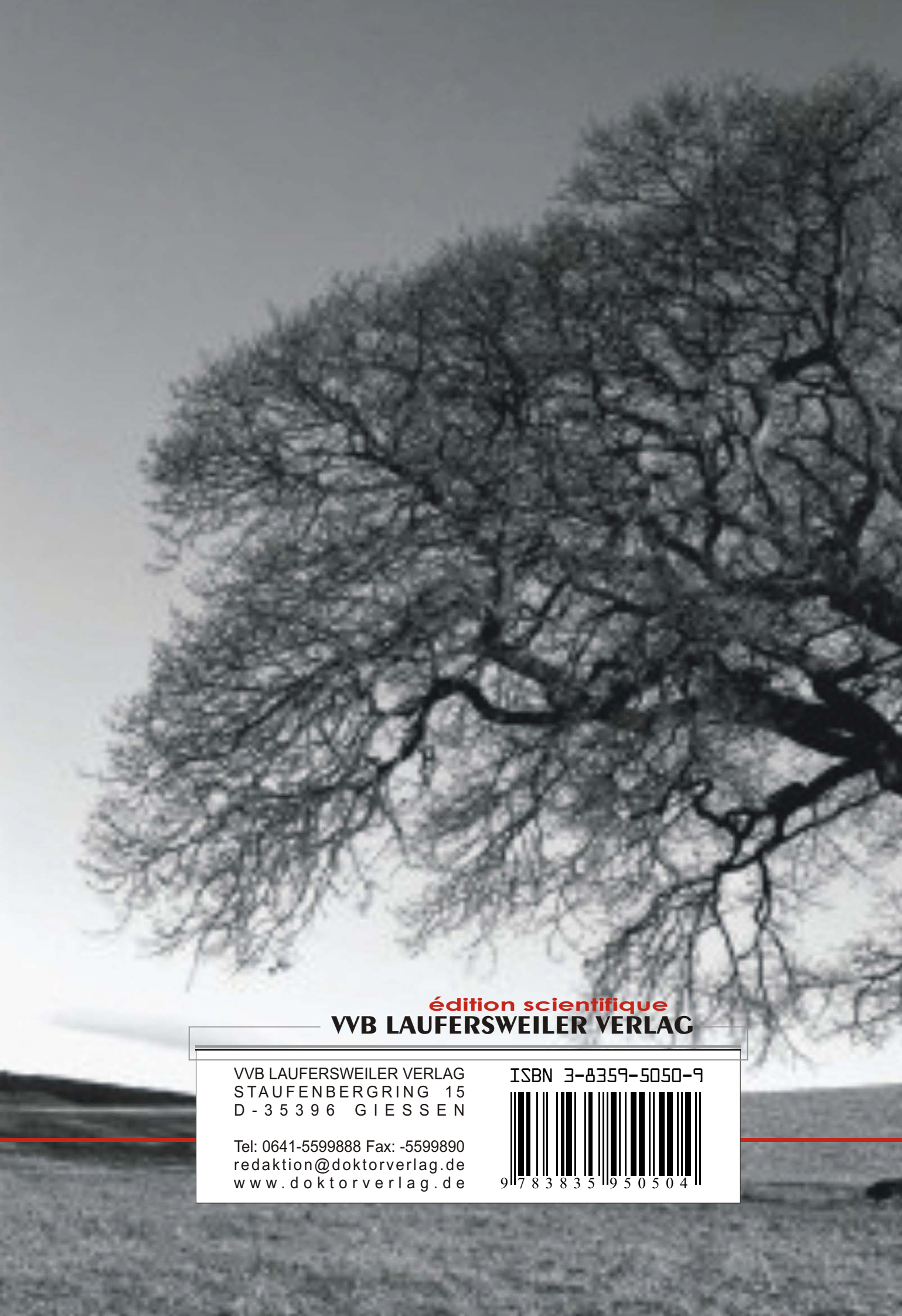

édition scientifique
VVB LAUFERSWEILER VERLAG

VVB LAUFERSWEILER VERLAG
STAUFENBERGRING 15
D-35396 GIESSEN

Tel: 0641-5599888 Fax: -5599890
redaktion@doktorverlag.de
www.doktorverlag.de

ISBN 3-8359-5050-9

9 783835 950504